

University of Windsor

Scholarship at UWindor

Electronic Theses and Dissertations

Theses, Dissertations, and Major Papers

1-1-2006

Numerical simulation of paint spray process.

Ligong Yang
University of Windsor

Follow this and additional works at: <https://scholar.uwindsor.ca/etd>

Recommended Citation

Yang, Ligong, "Numerical simulation of paint spray process." (2006). *Electronic Theses and Dissertations*. 7229.

<https://scholar.uwindsor.ca/etd/7229>

This online database contains the full-text of PhD dissertations and Masters' theses of University of Windsor students from 1954 forward. These documents are made available for personal study and research purposes only, in accordance with the Canadian Copyright Act and the Creative Commons license—CC BY-NC-ND (Attribution, Non-Commercial, No Derivative Works). Under this license, works must always be attributed to the copyright holder (original author), cannot be used for any commercial purposes, and may not be altered. Any other use would require the permission of the copyright holder. Students may inquire about withdrawing their dissertation and/or thesis from this database. For additional inquiries, please contact the repository administrator via email (scholarship@uwindsor.ca) or by telephone at 519-253-3000ext. 3208.

NUMERICAL SIMULATION OF PAINT SPRAY PROCESS

By
Ligong Yang

A Dissertation

Submitted to the Faculty of Graduate Studies and Research through
Mechanical, Automotive and Materials Engineering
in Partial Fulfillment of the Requirements for
the Degree of Doctor of Philosophy at
the University of Windsor

Windsor, Ontario, Canada

2006



Library and Archives
Canada

Published Heritage
Branch

395 Wellington Street
Ottawa ON K1A 0N4
Canada

Bibliothèque et
Archives Canada

Direction du
Patrimoine de l'édition

395, rue Wellington
Ottawa ON K1A 0N4
Canada

Your file Votre référence
ISBN: 978-0-494-57569-7
Our file Notre référence
ISBN: 978-0-494-57569-7

NOTICE:

The author has granted a non-exclusive license allowing Library and Archives Canada to reproduce, publish, archive, preserve, conserve, communicate to the public by telecommunication or on the Internet, loan, distribute and sell theses worldwide, for commercial or non-commercial purposes, in microform, paper, electronic and/or any other formats.

The author retains copyright ownership and moral rights in this thesis. Neither the thesis nor substantial extracts from it may be printed or otherwise reproduced without the author's permission.

In compliance with the Canadian Privacy Act some supporting forms may have been removed from this thesis.

While these forms may be included in the document page count, their removal does not represent any loss of content from the thesis.

AVIS:

L'auteur a accordé une licence non exclusive permettant à la Bibliothèque et Archives Canada de reproduire, publier, archiver, sauvegarder, conserver, transmettre au public par télécommunication ou par l'Internet, prêter, distribuer et vendre des thèses partout dans le monde, à des fins commerciales ou autres, sur support microforme, papier, électronique et/ou autres formats.

L'auteur conserve la propriété du droit d'auteur et des droits moraux qui protègent cette thèse. Ni la thèse ni des extraits substantiels de celle-ci ne doivent être imprimés ou autrement reproduits sans son autorisation.

Conformément à la loi canadienne sur la protection de la vie privée, quelques formulaires secondaires ont été enlevés de cette thèse.

Bien que ces formulaires aient inclus dans la pagination, il n'y aura aucun contenu manquant.


Canada

© Ligong Yang 2006

ACKNOWLEDGEMENTS

This work would not have been completed were it not for the tireless patience of my wife, Yuxia. Indeed, were it not for her encouragement, I would not have kept the patience to overcome obstacles in this work.

The person, however, who is most responsible for the vision and quality of this work is Dr. R. M. Barron. Great thanks should be given to him for his guidance and unceasing help during this study.

Thanks goes to Mr. M. A. Malik of DaimlerChrysler Canada, for arranging access to the computer facilities at the University of Windsor/DaimlerChrysler Automotive Research and Development Centre, and for his discussions on various aspects of this study.

Thanks are also due to Dr. G. W. Rankin, Dr. N. Zamani, Dr. P. F. Henshaw and Dr. M. F. Lightstone for evaluating this dissertation as committee members and for their enlightening questions.

Special thanks should be extended to Dr. P. Maksimovic and Dr. E. Koutsavdis of FLUENT for their technical support.

Thanks goes to Mr. C. Tighe of DaimlerChrysler Canada for sharing experimental data with me and to Mrs. B. Mulaosmanovic for creating some of the geometry models.

Finally, I would like to acknowledge the Natural Sciences and Engineering Research Council of Canada, University of Windsor and DaimlerChrysler Canada Inc. for their financial support.

ABSTRACT

The electrostatic high-speed rotating bell (ESRB) applicator is widely used in the automotive finishing industry because of its atomization characteristics and high transfer efficiency. In order to study the paint spray process of an ESRB, a three-step CFD simulation methodology has been developed in this research work, using the commercial CFD code FLUENT. First, the paint flow in the atomizer is simulated, using an Euler approach. Paint droplet size and velocities at the edge of the atomizer are determined based on the simulation. Then, the Euler-Lagrange approach is applied to investigate the droplet transfer process. The air is treated as a continuum and the paint droplets are tracked as dispersed parcels. Models for electrostatic force and drag force on the droplets, and droplet breakup and collision models are incorporated in this step. Finally, the paint film thickness on the target plate and the transfer efficiency are calculated based on the paint mass accretion on the target plate. The effects that various operating parameters, such as flow rates, bell rotation speed and voltage, have on the flow field and, in particular, on the film build and transfer efficiency are examined. The results of the simulations are compared with experimental observations and data from published literature and from the paint spray lab at the University of Windsor/DaimlerChrysler Canada Automotive Research & Development Centre (ARDC).

DEDICATION

To my wife

TABLE OF CONTENTS

ABSTRACT	iv
DEDICATION	v
ACKNOWLEDGEMENTS	vi
LIST OF TABLES	x
LIST OF FIGURES	xi
NOMENCLATURE	xvii
CHAPTER 1 INTRODUCTION	1
CHAPTER 2 LITERATURE REVIEW	7
2.1 DISINTEGRATION REGION	8
2.2 FULLY DEVELOPED SPRAY REGION	8
2.3 DROPLET/WALL INTERACTION REGION	10
2.4 ELECTROSTATIC FORCE IN SPRAY APPLICATIONS	12
2.5 NUMERICAL SIMULATIONS ON PRESSURE-SWIRL ATOMIZERS	13
2.6 HIGH-SPEED ROTARY ATOMIZERS	14
2.7 SUMMARY OF PREVIOUS STUDIES	15
CHAPTER 3 MULTIPHASE SIMULATION APPROACHES	17
3.1 EULER-EULER APPROACH	17
3.1.1 The Eulerian Model	18
3.1.2 The Mixture Model	18
3.1.3 The VOF Model	19
3.2 EULER-LAGRANGE APPROACH	19
3.3 SUMMARY	20
CHAPTER 4 SIMULATION OF FLOW IN THE ATOMIZER	22
4.1 THE COMPUTATIONAL DOMAIN	24
4.2 NUMERICAL ALGORITHM	25
4.3 DROPLET PROPERTIES AT THE ATOMIZER EDGE	26

4.4	SIMULATION CONDITIONS -----	29
4.5	RESULTS AND DISCUSSION -----	30
4.6	CONCLUSIONS-----	34
CHAPTER 5 DROPLET TRANSFER SIMULATION -----		39
5.1	FLUENT'S DISCRETE PHASE MODEL-----	39
5.2	COMPONENTS OF THE SPRAY MODEL -----	41
5.2.1	Injection Model-----	41
5.2.2	Droplet Collision Model -----	41
5.2.3	Spray Breakup Model -----	42
5.2.4	Drag Model -----	43
5.3	ELECTROSTATIC FORCE INCORPORATION-----	44
5.4	MODELING TURBULENT DISPERSION OF DROPLETS -----	46
5.5	THE COMPUTATIONAL DOMAIN-----	46
5.5.1	Mesh for Electrostatic Field Simulation -----	47
5.5.2	Mesh for Droplet Transfer Simulation -----	48
5.6	NUMERICAL ALGORITHM -----	53
5.6.1	Numerical Algorithm for Electric Field Simulation -----	53
5.6.2	Numerical Algorithm for Droplet/Airflow Field Simulation -----	53
5.7	SIMULATION CONDITIONS -----	54
5.8	RESULTS AND DISCUSSION -----	56
5.8.1	Electric Field Simulation-----	56
5.8.2	Air and Droplet Flow Fields (Baseline Conditions)-----	58
5.8.3	Effect of Voltage -----	68
5.8.4	Effect of Droplet Diameter -----	71
5.8.5	Effect of Bell Rotational Speed -----	75
5.8.6	Effect of Paint Flow Rate -----	78
5.8.7	Effect of Shaping Air Flow Rate-----	81
5.8.8	Effect of Spray Angle -----	86
5.9	CONCLUSIONS-----	88
CHAPTER 6 PAINT FILM THICKNESS AND TRANSFER EFFICIENCY -----		89

6.1	PAIN T FILM THICKNESS CALCULATION -----	90
6.2	TRANSFER EFFICIENCY CALCULATION -----	92
6.3.1	Paint Film Thickness Profile and Spray Transfer Efficiency at Baseline Condition -----	93
6.3.2	Effect of Voltage -----	94
6.3.3	Effect of Droplet Diameter -----	94
6.3.4	Effect of Bell Rotational Speed -----	95
6.3.5	Effect of Paint Flow Rate -----	96
6.3.6	Effect of Shaping Air Flow Rate -----	97
6.3.7	Effect of Spray Angle -----	99
6.4	CONCLUSIONS -----	100
CHAPTER 7 CONCLUSIONS AND RECOMMENDATIONS -----		101
7.1	CONCLUSIONS -----	101
7.1.1	Simulation of the Flow in the Atomizer -----	101
7.1.2	Droplet Transfer Simulation -----	101
7.1.3	Film Thickness and Transfer Efficiency Calculation -----	102
7.2	RECOMMENDATIONS FOR FUTURE WORK -----	103
REFERENCES -----		105
APPENDIX USER DEFINED FUNCTIONS -----		113
UDF1 - ELECTROSTATIC FIELD STRENGTH CALCULATION -----		113
UDF2 - ELECTROSTATIC FORCE INCORPORATION -----		114
UDF3 - CALCULATION OF MASS ACCUMULATION ON THE TARGET PLATE -----		116
VITA AUCTORIS -----		119

LIST OF TABLES

Chapter 4

Table 4.1 Numerical Simulation Conditions for Paint Flow Rate of 150 cc/min.....	30
Table 4.2 Numerical Simulation Conditions for Bell Rotating Speed of 38000 rpm.....	30
Table 4.3 Coefficients and R^2 Values of Linear Curve Fit	33

Chapter 5

Table 5.1 Analogy between a Spring-Mass System and a Distorting Droplet	42
Table 5.2 Characteristics of Electrostatic Field Domain and Flow Domain	52
Table 5.3 Numerical Simulation Conditions of Droplet Transfer Process for Varying Electric Charge	55
Table 5.4 Numerical Simulation Conditions of Droplet Transfer Process for Varying Paint Flow Rate.....	55
Table 5.5 Numerical Simulation Conditions of Droplet Transfer Process for Varying Shaping Air Flow Rate	55
Table 5.6 Numerical Simulation Conditions of Droplet Transfer Process for Varying Bell Rotational Speed.....	55

Chapter 6

Table 6.1 Summary of the Parametric Study on the Paint Film Thickness and Transfer Efficiency.....	100
---	-----

LIST OF FIGURES

Chapter 1

Figure 1.1 Schematic of Typical Automotive Coating Process.....	2
Figure 1.2 Basecoat Spray Booth.....	2
Figure 1.3 Perspective and Section View of Paint Spray Nozzle.....	3
Figure 1.4 Spray Regions.....	5

Chapter 4

Figure 4.1 Schematic Meridian View of the Bell-shape Atomizer.....	23
Figure 4.2 Mesh for One Quarter of the Atomizer	25
Figure 4.3 3D Illustration of Paint Film Thickness at the Bell Edge.....	28
Figure 4.4 Flow Chart for Calculating the Paint Film Thickness at the Bell Edge	29
Figure 4.5 Velocity Vectors on a Meridian Plane of the Bell-shape Atomizer	31
Figure 4.6 Velocity Vectors on a Meridian Plane near the Inlet of the Bell-shape Atomizer	31
Figure 4.7 Film Thickness at the Bell Edge as a Function of Reynolds Number [from Domnick & Thieme (2004)]	32
Figure 4.8 Droplet Size vs. Bell Rotation Speed (paint flow rate = 150 cc/min)	34
Figure 4.9 Droplet Size vs. Paint Flow Rate (bell rotation speed = 38000 rpm).....	35
Figure 4.10 Droplet Axial and Radial Velocities vs. Bell Rotation Speed (paint flow rate = 150 cc/min).....	35
Figure 4.11 Droplet Axial and Radial Velocities vs. Paint Flow Rate (bell rotation speed = 38000 rpm)	36
Figure 4.12 Droplet Tangential Velocities vs. Bell Rotation Speed (paint flow rate = 150 cc/min)	36
Figure 4.13 Droplet Tangential Velocities vs. Paint Flow Rate (bell rotation speed = 38000 rpm).....	37
Figure 4.14 Spray Angle vs. Bell Rotation Speed (paint flow rate = 150 cc/min)	37
Figure 4.15 Spray Angle vs. Paint Flow Rate (bell rotation speed = 38000 rpm).....	38

Chapter 5

Figure 5.1 Charge-to-Mass Ratio vs. Drop Diameter for the Rotary Bell Atomizer at 40 kV Operating Voltage [from Gemci et al. (2002)]	45
Figure 5.2 Charge-to-Mass Ratio vs. Drop Diameter for the Rotary Bell Atomizer at 70 kV Operating Voltage [from Gemci et al. (2002)]	45
Figure 5.3 Computational Domain for Electrostatic Potential Calculation	48
Figure 5.4 Computational Mesh Distribution for Electrostatic Potential Calculation.....	48
Figure 5.5 Static Pressure Contours from 2D Air Jet Simulation.....	49
Figure 5.6 Static Pressure Contours from 2D Air Jet Simulation with Extended Domain	50
Figure 5.7 Velocity Magnitude Contours from 2D Air Jet Simulation	50
Figure 5.8 Velocity Magnitude Contours from 2D Air Jet Simulation with Extended Domain.....	51
Figure 5.9 Mesh Distribution for Air Flow and Droplet Transfer Simulation.....	52
Figure 5.10 Horizontal View of Electric Potential Contours at $Z = 0.327$ m.....	57
Figure 5.11 Horizontal View of Electric Potential Contours at $Z = 0.2$ m.....	57
Figure 5.12 Meridian View of Electric Potential Contours	58
Figure 5.13 Meridian View of Electric Field Strength Vectors.....	58
Figure 5.14 Static Pressure Contours on the Target Plate for a Pure Air Spray (shaping air flow rate = 250 cc/min).....	59
Figure 5.15 Meridian View of Air Velocity Vectors (paint flow rate = 150 cc/min, shaping air flow rate = 250 cc/min).....	60
Figure 5.16 Meridian View of Air Velocity Magnitude Contours (paint flow rate = 150 cc/min, shaping air flow rate = 250 cc/min)	61
Figure 5.17 Meridian View of Static Pressure Contours (paint flow rate = 150 cc/min, shaping air flow rate = 250 cc/min).....	61
Figure 5.18 Meridian View of Turbulent Kinetic Energy Contours (paint flow rate = 150 cc/min, shaping air flow rate = 250 cc/min)	62
Figure 5.19 Meridian View of Turbulent Dissipation Rate Contours (paint flow rate = 150 cc/min, shaping air flow rate = 250 cc/min)	63
Figure 5.20 Static Pressure Contours on the Target Plate (paint flow rate = 150 cc/min, shaping air flow rate = 250 cc/min).....	64

Figure 5.21 Static Pressure Contours at the Centre of the Target Plate (paint flow rate = 150 cc/min, shaping air flow rate = 250 cc/min)	64
Figure 5.22 Turbulent Kinetic Energy Contours on the Target Plate (paint flow rate = 150 cc/min, shaping air flow rate = 250 cc/min)	65
Figure 5.23 Turbulent Kinetic Energy Contours at the Centre of the Target Plate (paint flow rate = 150 cc/min, shaping air flow rate = 250 cc/min).....	66
Figure 5.24 Turbulent Dissipation Rate Contours on the Target Plate (paint flow rate = 150 cc/min, shaping air flow rate = 250 cc/min)	66
Figure 5.25 Turbulent Dissipation Rate Contours at the Centre of the Target Plate (paint flow rate = 150 cc/min, shaping air flow rate = 250 cc/min).....	67
Figure 5.26 Droplet Trace Coloured by Droplet Residence Time (paint flow rate = 150 cc/min, shaping air flow rate = 250 cc/min)	68
Figure 5.27 Meridian View of Air Velocity Magnitude Contours at 50 kV.....	69
Figure 5.28 Meridian View of Air Velocity Magnitude Contours at 90 kV.....	69
Figure 5.29 Static Pressure Contours on the Target Plate at 50 kV.....	70
Figure 5.30 Static Pressure Contours on the Target Plate at 90 kV.....	70
Figure 5.31 Droplet Trace Coloured by Droplet Residence Time at 50 kV	71
Figure 5.32 Droplet Trace Coloured by Droplet Residence Time at 90 kV	71
Figure 5.33 Meridian View of Static Pressure Contours using One-tenth of Film Thickness at the Bell Edge as Initial Droplet Diameter.....	73
Figure 5.34 Static Pressure Contours on the Target Plate using One-tenth of Film Thickness at the Bell Edge as Initial Droplet Diameter.....	73
Figure 5.35 Turbulent Kinetic Energy Contours on the Target Plate using One-tenth of Film Thickness at the Bell Edge as Initial Droplet Diameter	74
Figure 5.36 Turbulent Dissipation Rate Contours on the Target Plate using One-tenth of Film Thickness at the Bell Edge as Initial Droplet Diameter	74
Figure 5.37 Droplet Trace Coloured by Droplet Residence Time using One-tenth of Film Thickness at the Bell Edge as Initial Droplet Diameter.....	75
Figure 5.38 Meridian View of Velocity Vectors (bell rotational speed = 42000 rpm)	76
Figure 5.39 Meridian View of Static Pressure (bell rotational speed = 42000 rpm)	76

Figure 5.40 Static Pressure Contours at the Centre of the Target Plate (bell rotational speed = 42000 rpm)	77
Figure 5.41 Turbulent Kinetic Energy Contours at the Centre of the Target Plate (bell rotational speed = 42000 rpm)	77
Figure 5.42 Turbulent Dissipation Rate Contours at the Centre of the Target Plate (bell rotational speed = 42000 rpm)	78
Figure 5.43 Meridian View of Static Pressure Contours (paint flow rate = 200 cc/min, shaping air flow rate = 250 cc/min)	79
Figure 5.44 Static Pressure Contours at the Centre of the Target Plate (paint flow rate = 200 cc/min, shaping air flow rate = 250 cc/min)	79
Figure 5.45 Turbulent Kinetic Energy Contours at the Centre of the Target Plate (paint flow rate = 200 cc/min, shaping air flow rate = 250 cc/min)	80
Figure 5.46 Turbulent Dissipation Rate Contours at the Centre of the Target Plate (paint flow rate = 200 cc/min, shaping air flow rate = 250 cc/min)	80
Figure 5.47 Droplet Trace Coloured by Droplet Residence Time (paint flow rate = 200 cc/min, shaping air flow rate = 250 cc/min)	81
Figure 5.48 Meridian View of Static Pressure Contours (paint flow rate = 175 cc/min, shaping air flow rate = 150 cc/min)	82
Figure 5.49 Static Pressure Contours on the Target Plate (paint flow rate = 175 cc/min, shaping air flow rate = 150 cc/min)	82
Figure 5.50 Turbulent Kinetic Energy Contours at the Centre of the Target Plate (paint flow rate = 175 cc/min, shaping air flow rate = 150 cc/min)	83
Figure 5.51 Turbulent Dissipation Rate Contours on the Target Plate (paint flow rate = 175 cc/min, shaping air flow rate = 150 cc/min)	83
Figure 5.52 Meridian View of Static Pressure Contours (paint flow rate = 175 cc/min, shaping air flow rate = 250 cc/min)	84
Figure 5.53 Static Pressure Contours on the Target Plate (paint flow rate = 175 cc/min, shaping air flow rate = 250 cc/min)	84
Figure 5.54 Turbulent Kinetic Energy Contours at the Centre of the Target Plate (paint flow rate = 175 cc/min, shaping air flow rate = 250 cc/min)	85

Figure 5.55 Turbulent Dissipation Rate Contours on the Target Plate (paint flow rate = 175 cc/min, shaping air flow rate = 250 cc/min)	85
Figure 5.56 Meridian View of Static Pressure Contours (spray angle = 22.5°).....	86
Figure 5.57 Static Pressure Contours on the Target Plate (spray angle = 22.5°).....	87
Figure 5.58 Turbulent Kinetic Energy Contours at the Centre of the Target Plate (spray angle = 22.5°).....	87
Figure 5.59 Turbulent Dissipation Rate Contours at the Centre of the Target Plate (spray angle = 22.5°).....	88

Chapter 6

Figure 6.1 Paint Accretion on the Target Plate for 0.25 s at the Baseline Operating Condition (kg/m^2)	90
Figure 6.2 Bands Created for Paint Film Thickness Calculation.....	91
Figure 6.3 Paint Film Thickness Profile and Transfer Efficiency (paint flow rate = 150 cc/min, shaping air flow rate = 250 cc/min)	93
Figure 6.4 Predicted Paint Film Thickness Profiles and Transfer Efficiencies for Varying Electric Charge	94
Figure 6.5 Predicted Paint Film Thickness Profiles and Transfer Efficiencies for Varying Initial droplet Diameter.....	95
Figure 6.6 Predicted Paint Film Thickness Profiles and Transfer Efficiencies for Varying Rotational Speed	95
Figure 6.7 Paint Film Thickness Profile and Transfer Efficiency (paint flow rate = 175 cc/min, shaping air flow rate = 250 cc/min)	96
Figure 6.8 Paint Film Thickness Profile and Transfer Efficiency (paint flow rate = 200 cc/min, shaping air flow rate = 250 cc/min)	97
Figure 6.9 Predicted Paint Film Thickness Profiles and Transfer Efficiencies for Varying Paint Flow Rate (shaping air flow rate = 250 cc/min).....	97
Figure 6.10 Paint Film Thickness Profile and Transfer Efficiency (paint flow rate = 175 cc/min, shaping air flow rate = 150 cc/min)	98
Figure 6.11 Paint Film Thickness Profile and Transfer Efficiency (paint flow rate = 175 cc/min, shaping air flow rate = 200 cc/min)	98

Figure 6.12 Predicted Paint Film Thickness Profiles and Transfer Efficiencies for Varying Shaping Air Flow Rate (paint flow rate = 175 cc/min) 99

Figure 6.13 Predicted Paint Film Thickness Profiles and Transfer Efficiencies for Varying Spray Angle 99

NOMENCLATURE

\dot{Q}	Mass flow rate of paint, kg/s
ρ	Density, kg/m ³
ρ_a	Density of air, kg/m ³
ρ_p	Density of paint, kg/m ³
R	Internal radius of atomizer bell cup at its edge, m
δ	Paint film thickness at the edge of atomizer bell cup, m
v_a	Axial velocity of paint, m/s
v_r	Radial velocity of paint, m/s
v_θ	Tangential velocity of paint, m/s
θ	Spray angle or cone angle, degree
d_p	Paint droplet diameter, micron
F	Electric force on droplet, N
ϕ	Electric potential, V
E	Electric field strength, V/m
q	Electric charge, C
C_v	Volumetric solid component ratio
$C_{q,m}$	Droplet charge-to-mass ratio, C/kg
C_D	Drag coefficient
S_f	Swirl fraction
m_i	Mass of droplet i , kg
A_j	Area of the cell face j , m ²
D_j	Discrete phase model (DPM) accretion on cell face j , kg/m ²
M_k	Mass of paint accretion on band k , kg
Δ_k	Averaged wet paint film thickness on band k , milliinch (2.54e-5 m)
g_x	Gravitational acceleration in x direction, m/s ²

g_y	Gravitational acceleration in y direction, m/s^2
g_z	Gravitational acceleration in z direction, m/s^2
μ	Dynamic viscosity, $N*s/m^2$
μ_a	Dynamic viscosity of air, $N*s/m^2$
\bar{u}	Fluid phase velocity, m/s
\bar{u}_p	Paint droplet velocity, m/s
Re_d	Droplet Reynolds number

CHAPTER 1 INTRODUCTION

Appearance, colour and durability of the painted surface are very important criteria that customers consider when making a decision regarding the purchase of a motor vehicle. Therefore, automotive manufacturers are continuously searching for ways to improve the finish quality of their products. They are also driven by the market, and indirectly by government policy, to increase the transfer efficiency (TE) in the paint spray process and reduce the volatile organic compounds (VOC) emission.

Painting is an expensive process in the automotive industry. A one percent improvement in transfer efficiency (the ratio of the mass of paint deposited on the target object to that injected from the nozzle) of paint spray can save millions of dollars per year because of the savings on paint, energy and resources. Also, in order to protect the environment, automotive producers require low emission of VOC. High transfer efficiency leads to a reduction of VOC emissions and solid waste.

Coating application by means of electrostatic high-speed bell-type rotary atomizers is now widely used in the automotive industry. Compared with the conventional air atomization application, the transfer efficiency is significantly higher. The above factors provide a strong motivation for the study of the paint spray process.

Figure 1.1 shows a schematic of a typical automotive coating process. First, the anti-chip powder is sprayed onto the vehicle using the powder spray robots. Then the vehicle is moved into the oven in order to melt the powder, and the quality of the powder coating is inspected. If the result is satisfactory, the vehicle is moved into the basecoat and clearcoat zone where basecoat and clearcoat paints are sprayed onto it. The vehicle is then moved into the oven again to dehydrate the paint layer. After that, the paint layer on the vehicle is inspected again. If the result is satisfactory, the painting process is finished. In this study the basecoat spray process, using electrostatic high-speed rotating bell applicators (ESRB), is simulated.

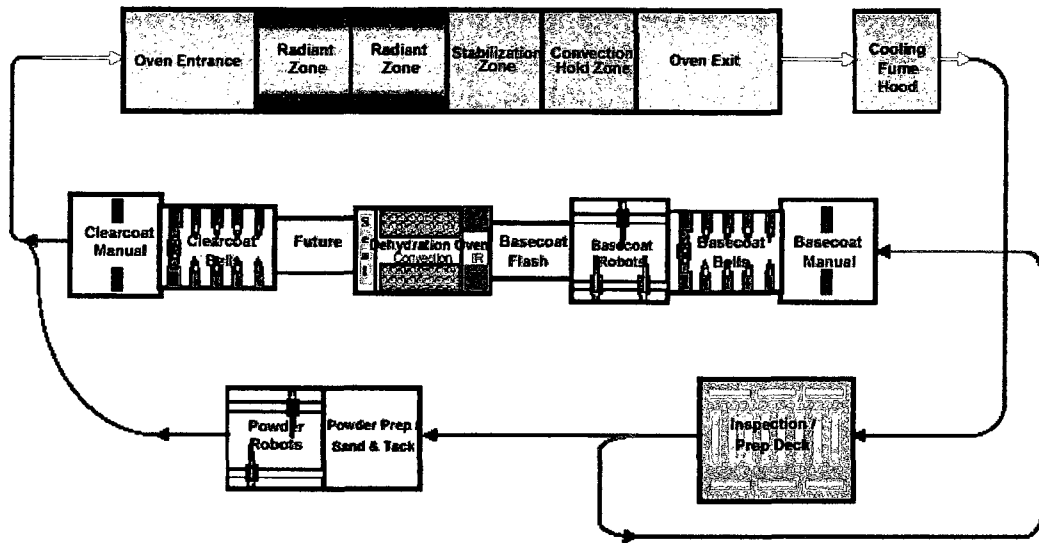


Figure 1.1 Schematic of Typical Automotive Coating Process

Figure 1.2 shows the layout of a basecoat spray booth. The ESRB applicator is installed at the end of each robot. The vehicle is placed in the middle of the booth during spraying.



Figure 1.2 Basecoat Spray Booth

Figure 1.3 shows a paint spray gun nozzle with an electrostatic high-speed bell-type rotary atomizer used in a typical paint spray booth. Since water-based paint is used in this study, an indirect electrostatic charge is supplied from six long cylindrical electrodes in an annular locus outside the paint spray gun nozzle. A bell-shape atomizer is installed at the tip of the nozzle. The rotation of the bell cup is driven by compressed air. For the applicator considered in this work, this (turbine) air and the bearing air exhaust along the outer wall of the bell cup, between the bell wall and the shaping air inlet. This exhaust air, along with the shaping air, forms an air curtain that confines the paint spray and increases deposition efficiency.

There is an annular jet ring near the outer rim of the bell cup. During normal operation, jets of paint emerge from the bell cup and the paint undergoes an atomization process, breaking up into droplets. Once airborne, the paint droplets mix with the surrounding air, and droplets collide, break up and coalesce. The flight of the droplets is confined by the air curtain that emerges from the rim of the bell cup. The electrostatic force generated by the positively charged electrodes and the grounded target plate also draws the paint droplets to the plate. Finally, the paint droplets hit the plate and the paint film is generated.

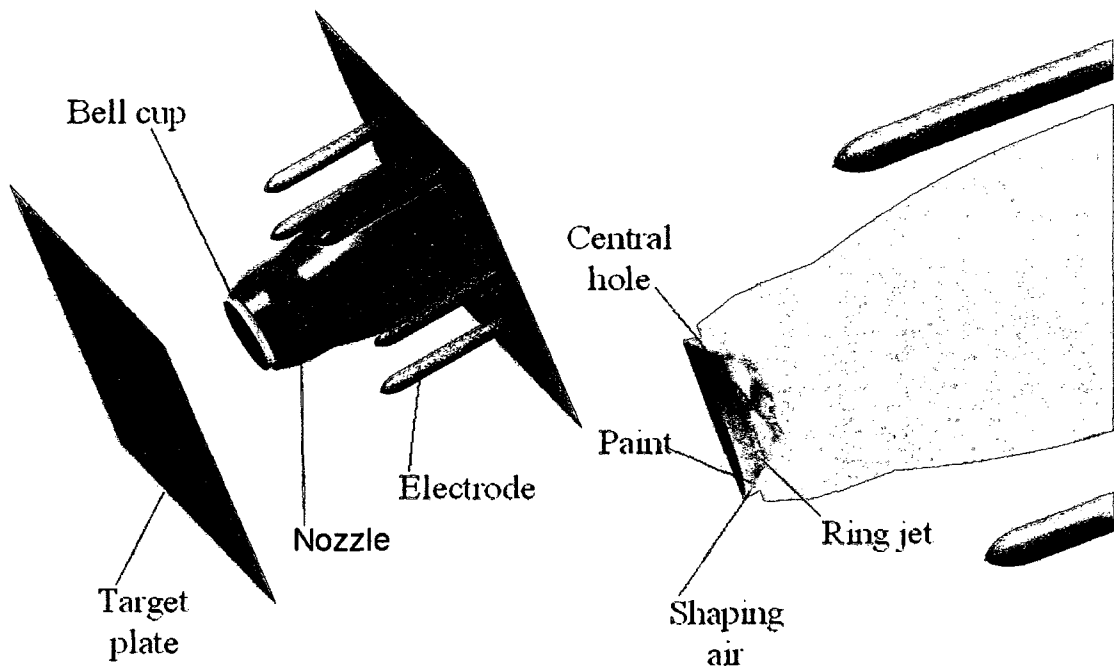


Figure 1.3 Perspective and Section View of Paint Spray Nozzle

Researchers have conducted experiments in which paint is sprayed onto a flat plate, and the resulting paint film thickness is measured. In the experimental setup, after the vertical paint spray was fully developed, a rectangular workpiece (target plate) with dimension of 36 inch x 4 inch was passed under the nozzle with a speed of 16 ft/min, i.e., 3.2 inch/s, at a distance of 10 inches from the nozzle. Since the width of the workpiece was 4 inches, it took 1.25 ($4 \div 3.2$) seconds for the plate to pass through the paint spray. During this process, paint droplets deposited on the workpiece and formed a thin layer of paint on it. The paint film that had deposited on the plate was then heated until 99 percent of the VOC had been removed. The dry paint film thickness was then measured along the centreline of the rectangular plate.

In order to determine the optimal setting combination to use in the ESRB paint spray process, such as geometric properties of the nozzle and atomizer, voltage of the electrodes, paint and shaping air flow rate, and distance between nozzle and target plate, experimentalists traditionally have to set up costly experiment facilities. These facilities include the particular spray nozzle being tested, high-voltage power source, and expensive light-scattering interferometry instruments, such as a Phase Doppler Anemometer (PDA) and/or a Malvern Particle Sizer. Meanwhile, the testing methods can only obtain data at the exact location where the measurement is taken. For example, PDA can only measure the droplet velocities where the interference area of the laser beams is located. In order to get the droplet properties at any location in the spray, the laser interference area must loop through the whole spray region. Furthermore, measurement difficulties arise in the following aspects: (i) the large amount of droplets in a spray, (ii) the high speed and widely varying velocity of the droplets, (iii) the wide range of droplet sizes encountered in most sprays, and (iv) the changes in droplet size through evaporation, breakup and coalescence. The high cost of building facilities and conducting experiments provides strong motivation for the relatively less expensive Computational Fluid Dynamics (CFD) simulation for the study of the paint spray process.

Although ESRB paint spray has been used for many years in the industry, a deeper understanding of paint atomization, droplet transport and deposition may lead to overall paint quality and process improvements. Typically a spray system can be broken down into three regions: disintegration region, fully developed spray region and

droplet/wall interaction region, as illustrated in Figure 1.4. In the disintegration zone, the liquid paint jet from the nozzle is atomized and a very dense spray is generated. Downstream of this atomization region, the spray is assumed to be fully developed, and the droplet/droplet and droplet/air interactions dominate the flow. In the third region, deposition and/or reflection of the droplets occur at the target plate.

The overall objectives of the present study are: (i) to acquire a more detailed and comprehensive understanding of the spray application process, (ii) to develop a methodology for numerical simulation of the paint spray process, (iii) to investigate various factors affecting the paint spray process, and their effect on paint film thickness on the target plate and droplet transfer efficiency, and (iv) to provide suggestions to improve the paint spray process.

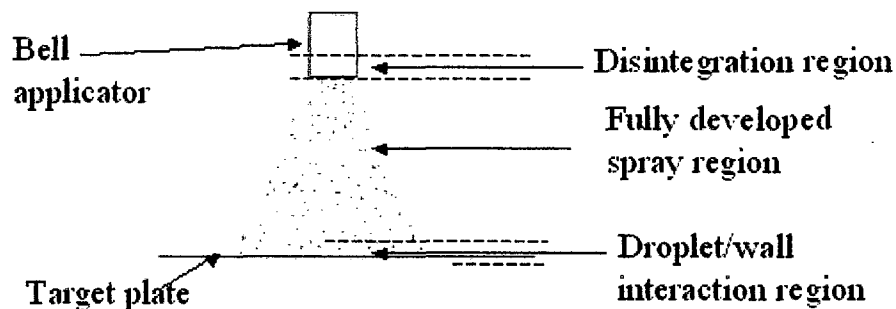


Figure 1.4 Spray Regions

Three commercial softwares have been used to carry out this study. The CAD model of the atomizer is created with CATIA. The meshes are created with ANSYS ICEM CFD HEXA. The flow simulations are performed and post-processed using FLUENT, which is run on a workstation.

The CFD predictions for the paint film thickness on the target plate and the spray transfer efficiency are compared to the experimental results from the ARDC paint lab.

This dissertation is organized as follows: A survey of the relevant literature is presented in Chapter 2. Some general approaches for multiphase simulation are described in Chapter 3. Chapter 4 is devoted to the CFD simulation in the atomizer. Droplet transfer simulation is described in Chapter 5. A method for calculating paint film thickness

profiles and spray transfer efficiency is presented in Chapter 6, and the computational and experimental results are compared. Finally, some conclusions and recommendations are suggested in Chapter 7.

CHAPTER 2 LITERATURE REVIEW

Sprays are applied in many applications, such as agriculture, fuel injection, pharmaceuticals, powder and liquid paint coatings.

Paint spray is a very complex process. Lefebvre (1989) provided one of the first comprehensive classifications of atomizers and described the general droplet measurement methods and facilities needed for experimental atomization studies. He listed and explained many terminologies used in spray research. These terminologies have now been widely adopted by many researchers. Typically, a spray system consists of three regions: disintegration region, fully developed spray region and droplet/wall interaction region (see Figure 1.4). Most studies reported in the literature are limited to only one of these three parts of the whole spray system.

In order to validate the CFD simulation of the paint spray process, CFD results should be compared with experimental data. Thus, some researchers have set up test facilities to provide the measurements. Others have developed CFD simulation models. In the current study, the rotational speed of the atomizer is very high. Thus, the spray forms a hollow cone close to the edge of the atomizer. Since a pressure-swirl atomizer also generates a hollow cone-shaped spray, some relevant research on pressure-swirl atomizers is reviewed in this chapter. Also, since a properly aligned electrostatic force significantly improves the spray efficiency, review on electrostatic force research cannot be overlooked.

The literature contains a considerable number of papers and books concerning experiments and CFD simulations of spray. The review of the relevant literature is organized in the following sections: (i) disintegration region, (ii) fully developed spray region, (iii) droplet/wall interaction region, (iv) electrostatic force in spray applications, (v) numerical simulations of pressure-swirl atomizer and (vi) high-speed rotary atomizers. Finally a summary of the previous research is presented.

2.1 Disintegration Region

Different types of atomizers have been employed in various applications. Typical atomizers encountered in industry include the fan atomizer, pressure-swirl atomizer and electrostatic high-speed rotary atomizer. The diversity of the atomizers demonstrates the variety of atomization mechanisms that may occur.

Many researchers have attempted to measure the droplet size in the disintegration region and summarized their results with empirical formulas, or stated their observations on a specific atomizer, e.g., Hinze and Milborn (1950), Bell and Hochberg (1981), Lefebvre (1987), Wang and Lefebvre (1987), St-George and Buchlin (1994), Bailey (1988), Snyder et al. (1989a & 1989b), McCarthy (1991), Corbeels et al. (1992), Bauckage et al. (1994) and Xing et al. (1999). The phase Doppler interferometry technique has been widely used in these studies. The most commonly used equipment for measuring droplet size and velocities are the Laser Doppler Anemometer (LDA), Phase Doppler Anemometer (PDA) and Malvern Particle Sizer (for size only). Unfortunately, no general relationships for the drop size of high-speed rotary atomizers have been proposed by these researchers

Li and Tankin (1988) calculated the droplet size distribution for pressure-swirl atomizers using information theory (or maximum entropy formalism) applied to atomization theory. They obtained a distribution that contains the Weber number as a parameter, and this Weber number is a function of the total number of droplets. The Sauter Mean Diameter (SMD) was also derived as a function of Weber number. Similar methodologies for predicting droplet size have been proposed by Bhatia and Durst (1989) and Van Der Geld and Vermeer (1994). Since the formulas they have proposed contain many geometric parameters of pressure-swirl atomizers, their formulas are not directly applicable to the rotary atomizer studied here.

2.2 Fully Developed Spray Region

Most published articles in the literature on the fully developed spray region consider both measurement and numerical simulation.

Hicks (1995) and Hicks and Senser (1995) numerically simulated paint transfer in an air spray process by incorporating a number of assumptions based on measurements. The direct effect of turbulent air velocity fluctuations on the trajectories of paint droplets was incorporated via a stochastic separated flow approach. They compared their results with measurements and other published simulation results on the axial air velocity along the centreline of the spray, and the droplet transfer efficiency. They found that their assumptions were valid over broad ranges of atomizing air pressure and liquid flow rate since the shaping air augmented mixing and created a high aspect ratio spray.

Bauckage et al. (1994 & 1995) experimentally investigated the atomization characteristics of a commercial electrostatic high-speed rotary atomizer. The fluid atomized was a water-borne metallic paint typically used in automotive coating processes. Three geometrically different bell types were tested, one with serrations and two without. Axial zones of circulating droplets were observed. They also used a Phase Doppler Particle Analyzer to study the effect of electrostatic force and found that the droplet size was smaller with higher voltage and that the spray cone was wider.

Im (1999) and Im et al. (2001 & 2004) reviewed technological challenges and research issues, and then described the spray atomization, visualization, droplet size and velocity measurement results of a water-borne paint spray system under a range of various operating parameters such as liquid flow rate, shaping air flow rate, bell rotational speed and high voltage setting. Their results showed that the bell speed dominated the atomization, but high voltage and flow rate settings significantly modified the spray transport. They concluded that the droplet size decreased with the increase in bell speed, an increase in liquid flow rate widened the spray shape slightly, the spray cone was narrowed by a high flow rate of the shaping air, the spray cone decreased due to more consistent and finer atomization at higher bell speed, and the spray became denser and more uniform in the core region at high voltage. They also developed their own code to simulate the spray transfer process in an electrostatic high-speed rotary bell sprayer by using the Euler-Lagrange approach. The initial droplet properties, applied on the inlet to the fully developed spray region, were obtained from their experiments. They performed a parametric study by changing the voltage, the shaping air flow rate and charge-to-mass ratio. In each simulation, a uniform charge-to-mass ratio was applied on all the droplets.

Only the forces acting on the droplets were considered in their study. They neglected the effect that the droplets have on the air, and did not consider droplet breakup and coalescence. Unfortunately, there was no comparison with experimental data in their study. By employing the Euler-Lagrange approach, similar numerical simulations of the droplet transfer process have been carried out by McCarthy (1995), Bai and Gosman (1995), Dooley et al. (1997), Yarin and Weiss (1995), Mundo et al. (1995c), Ruger et al. (2000), Huang et al. (2000) and Fogliati et al. (2006).

Some researchers have carried out only a numerical investigation on the droplet transfer process. For example, Ellwood and Braslaw (1998) developed a model based on a Lagrangian particle tracking scheme to simulate the formation of spray patterns for charged droplets. Steady state spray patterns were computed using an iterative particle source in cell approach, which represented momentum exchange between the droplet and gas phase as a body force. The flow solver was based on a finite element formulation incorporating the streamlined upwind Petrov Galerkin method for stabilization. They did not provide validation for their simulation based on experimental data. Han et al. (1997) proposed a modified Taylor Analogy Breakup (TAB) model to simulate the breakup of initial blobs and subsequent droplets for the pressure-swirl atomizer and obtained good agreement with experiment. Their model has been adopted by many researchers, and has been incorporated into the commercial CFD code FLUENT for the simulation of droplet breakup.

2.3 Droplet/Wall Interaction Region

When a single droplet hits the solid plate, it may deposit on the plate, rebound from the plate, or break up into several smaller droplets. If a liquid film already exists on the plate, the incident droplet may cause ripples and splashing. The properties of the liquid (viscosity, density, surface tension), droplet diameter, droplet velocity and incident angle determine the fate of the droplet upon impingement. The Weber number is usually chosen as the criterion to predict the result of impingement since it includes surface tension and velocity, i.e., crucial parameters determining the deformation of droplets. Many researchers have experimentally investigated the impingement of a droplet on a

wall, or a droplet on a liquid film, including Pumphrey and Elmore (1990), Oguz and Prosperetti (1990), Trapaga and Szekely (1991), Chandra and Avedisian (1991), Rein (1993), Sommerfeld et al. (1993), Fukai et al. (1993 & 1995), Yarin and Weiss (1995), Cossali et al. (1997), Mao et al. (1997), Mundo et al. (1994, 1995a, 1995b, 1995c & 1998), Tropea and Marengo (1999), Weiss and Yarin (1999), Bussmann et al. (2000).

Numerical simulations on single droplet deformation during impingement, using the Volume of Fluid (VOF) model, have been performed by Ghafouri-Azar et al. (2002) and Garbero et al. (2002).

When a large number of spray droplets strike the wall or film, the impingement process will be significantly more complicated. McCarthy (1991) studied droplet rebound from a small workpiece in the spray of a conventional air applicator. Drop sizes and velocities were measured with a Phase Doppler Particle Analyzer. The workpiece was very small so as to minimize the aerodynamic blockage of the spray and allow optical access at positions very near the workpiece surface. He observed that rebound was significant at low shaping air flow rate, but became negligible when sufficient shaping air was applied. Bai and Gosman (1995) built a diesel engine spray impingement model, which was incorporated in a computer program – EPISO-SPRAY. The model involved the analysis of the impingement regimes and associated post-impingement characteristics. The predicted spray pattern near the wall, wall spray radius, wall spray height and droplet velocities during a very short period of time were compared with measurement and good agreement was achieved. Recently, Fogliati et al. (2006) predicted the paint deposition distribution on rectangular target plates using FLUENT. Sprays injected from a fan nozzle were used in their study. The nozzle and the target plates were kept stationary. The sprays were simulated using the Euler- Lagrange approach. The initial droplet properties were set based on experimental results. They simulated the sprays and paint deposition at plate orientation angles of 45°, 60° and 90°. Unfortunately, they did not report any comparison between numerical prediction and experimental measurement for the paint distribution on the target plates.

2.4 Electrostatic Force in Spray Applications

Electrostatic paint spray application has been a widely used industrial process for many years. The electrostatic charge on spray droplets causes most of the paint to deposit on the workpiece.

The applied potential on the electrodes must be sufficiently high so that an electrostatic field is established in the vicinity of points where air molecules are disrupted by the electrostatic stress into ion-electron pairs. Electrode potentials of a few kilovolts and above are normally used. An electrode at a positive potential attracts negative electrons and repels positive ions away from it, thus behaving as a positive ion source. The positive ions attach to neutral paint molecules to form positive charged paint droplets. Although the electrostatic field is mainly dominated by the electric charge on the electrodes, it is also affected by the charge of the droplets and the movement of the charged droplets (Bailey (1988)).

A thorough and detailed determination of the electrostatic field is very complicated. Following Bailey (1998), Ellwood and Braslaw (1998) and Im (1999), the electrostatic field force F on the charged droplet can be expressed as

$$F = qE \quad (2.1)$$

where q is the charge of the droplet and E is the electric field strength, defined as

$$E = \frac{\partial \phi}{\partial s} \quad (2.2)$$

where ϕ is electric potential and s is distance.

Neglecting the effect of charged droplets on the electrostatic field, the governing equation for the electric potential is

$$\nabla^2 \phi = 0 . \quad (2.3)$$

The charge on the droplet is determined by many factors, including properties of the liquid, mass of the droplet, surface area of the droplet, strength of the electrostatic field, etc. Although a comprehensive formula for droplet charge is not available, charge-to-mass ratio ($c_{q,m}$) is a basic parameter that is widely used in charged droplet transfer simulations. Although Ellwood and Braslaw (1998) and Im (1999) used fixed charge-to-mass ratio in the whole domain of their simulations, the fact is that the charge-to-mass

ratio is not uniform to all the droplets in an electrostatic field. Gemci et al. (2002) calculated the individual droplet charge-to-mass ratio based on the drop size and velocity measured with a Phase Doppler Interferometer. He concluded that the droplet size decreased with increasing electric potential.

2.5 Numerical Simulations on Pressure-Swirl Atomizers

Four features are shared by pressure-swirl atomizers and rotary atomizers: (i) the liquid has high swirl near the exit of the atomizers, (ii) a liquid film forms along the atomizer wall near the exit, (iii) a cone of air exists at the centre of the atomizer, and (iv) a hollow cone spray is produced. There are also some important differences between them: (i) the swirling of liquid in pressure-swirl atomizers is caused by the helical channels, whereas the liquid swirling in rotary atomizers results from the rotation of the atomizer wall, (ii) the fluid rotational speed in a rotary atomizer is much higher than in a pressure-swirl atomizer, and (iii) the liquid film thickness at the rotary atomizer edge is much thinner, and so are the droplet sizes, compared to the pressure-swirl atomizer.

The similarities between the pressure-swirl atomizer and rotary atomizer, and the limited amount of literature on the rotary atomizer, make a review of the research on pressure-swirl atomizers necessary.

Yule and Chinn (1994) proposed a revised inviscid theory to calculate the discharge coefficient and spray angle for the pressure-swirl atomizer. By considering the conservation of axial momentum, this revised theory provided a better basis for the performance analysis and design of pressure-swirl atomizers.

Arcoumanis and Gavaises (2000) proposed a combined two-phase CFD nozzle model and 1D fuel injection system model to predict the flow development inside the discharge hole of a pressure-swirl atomizer connected to a common-rail based fuel injection system for DISI engines. The fuel injection model accounted for the transient pressure pulses that develop inside the common-rail and the injector upstream of the nozzle tip and predicted the fuel injection rate through the nozzle. The predicted transient velocity distribution upstream of the needle seat flow passage was used as the initial

condition to a 2D two-phase VOF model that solved for the location of the liquid-gas interface. These two-phase flow predictions were linked to experimental images.

Cousin and Nuglisch (2001) presented four models for predicting high pressure-swirl injector performance. A critical review of these models was made by using a huge experimental database where more than 3000 injectors were tested. The authors showed that one of the models predicted the flow rate and cone angle well. These authors also coupled this model with a model that predicted the linear stability of conical sheets. This coupling allowed the determination of a theoretical droplet diameter.

Moriyoshi et al. (2002) used the VOF model to simulate the two-phase flow inside the pressure-swirl injector and the liquid film formation process outside the nozzle. The Discrete Phase Model (DPM) was adopted to simulate a free fuel spray in a constant volume chamber. Multiphase simulation inside the pressure-swirl injector was also carried out by Alajbegovic and Meister (2001).

Chryssakis et al. (2003) developed a comprehensive model for pressure-swirl injectors. The model consisted of pre-spray and main spray modeling. The pre-spray modeling was based on an empirical solid cone approach with varying cone angle. The main spray modeling was based on the Liquid Instability Sheet Atomization approach. Compared with experimental data, some qualitative agreements of spray tip penetration and droplet size were achieved.

2.6 High-speed Rotary Atomizers

Although high-speed rotary atomizers have been investigated by some researchers, most of the published articles are focused on experiments. Some people have developed arguments about the general characteristics of the atomizer, others measured the droplet size. However, no universal formula about droplet size has been proposed.

Hinze and Milborn (1950) experimentally studied the atomization of liquids in a rotating cup. They proposed a formula for liquid film thickness at the edge of the cup. They observed that three different types of disintegration might take place around and beyond the edge of the cup: (a) direct drop formation disintegration, (b) ligament formation disintegration, and (c) film formation disintegration. Transition from (a) into

(b), or (b) into (c) is caused by an increased quantity of supply, an increased angular speed, a decreased diameter of the cup, an increased density, an increased viscosity, and a decreased surface tension of the liquid.

Bell and Hochberg (1981) studied the atomization, transportation and deposition of coatings of a high-speed electrostatic rotary atomizer. The dynamics of atomization and droplet deposition were examined using high-speed video recording techniques. They measured spray droplet sizes and speeds with laser scattering and Doppler methods. They also calculated the average droplet charge-to-mass ratio.

Corbeels et al. (1992) studied the effect of fluid properties and operational parameters on the atomization of a high-speed rotary bell paint applicator with serrations, using laser diffraction instrumentation and photography. They did not consider the influence of electrostatic force or shaping air. They found that a higher viscosity fluid filmed the bell more evenly and produced long regular ligaments.

Domnick and Thieme (2004) experimentally studied the atomization of the ESRB atomizer. They suggested that the atomization process could be divided into two models, viz., jet disintegration and turbulent disintegration. They also proposed empirical equations to determine the droplet SMD.

2.7 Summary of Previous Studies

Based upon the literature reviewed, the following observations can be made:

- Very few simulations of flow in a high-speed rotary atomizer have been performed.
- Few equations for the prediction of droplet size and velocity for a high-speed rotary atomizer have been proposed.
- Previous simulations of paint spray from a high-speed rotary atomizer are limited to the fully developed spray region.
- In previous droplet transfer simulations, the injected droplet properties have been specified based on experimental droplet size and velocity data.
- The effect of droplets on the air flow has been neglected.
- In most studies, droplet collision and breakup have been neglected.

- According to Gemci et al. (2002), the charge-to-mass ratio varies greatly with the droplet size in an electrostatic field. However, uniform charge-to-mass ratio values have been assumed without justification by previous researchers.
- Some researchers described the simulation of single droplet impingement with a target plate or liquid film. However, no simulation or calculation of paint film build on the target plate has been published.
- There has been little research on whether the impingement and deposition information is applicable to a paint film build calculation. Most of the previous work has focused only on single droplet impingement.
- Very few comparisons of simulated and experimental paint spray transfer efficiency (TE) have been published, although the TE value is one of the most important factors of concern to industry.
- The methodology that Moriyoshi et al. (2002) used is very instructive because it combines the atomization and droplet transfer simulation, although the atomizer they used is a pressure-swirl atomizer, instead of an ESRB atomizer.
- Although the atomizer used by Domnick and Thieme (2004) is a rotary atomizer, it is not the exact same type of atomizer used in the current study. For example, there is no centre hole in their atomizer. Furthermore, the droplet size they proposed was much less than the one used by Im (1999) and Im et al. (2001 & 2004), which was set based on their experimental data.

Analysis of the literature indicates that there is a critical need to develop a methodology to simulate the whole spray process, including atomization, droplet transfer and paint deposition. Having this capability will enable engineers to properly evaluate the result of a paint spray process so as to improve on the performance, i.e., increase transfer efficiency and paint film build uniformity, and decrease VOC emission.

CHAPTER 3 MULTIPHASE SIMULATION APPROACHES

The paint spray process under investigation in this study is a multiphase process. The liquid paint is pumped into the nozzle and pushed towards the outer wall of the atomizer by the centrifugal force produced by the high-speed rotation of the bell cup. At the edge of the bell cup, the paint is atomized into droplets. As these droplets move into the spray zone they undergo breakup, coalescence and collision. The trajectories of the droplets are affected by the aerodynamic force exerted by the air and the electrostatic force generated by the charged electrodes and grounded target plate. Furthermore, the charged moving droplets also affect the air flow and the electric field (Bailey, 1998). Finally, the droplets strike the target plate or paint film on the plate, and reflect or deposit onto it. The paint deposited on the plate will further spread out on the plate. Besides paint liquid and air, there are water and volatile organic compounds (VOC) of the paint that evaporate from the paint droplets and paint film on the plate. It is clear that paint spray is a very complex multiphase (paint, vapour and air) process.

Multiphase flow is usually simulated with the Euler-Euler approach or the Euler-Lagrange approach. These approaches are described in the next two sections.

3.1 Euler-Euler Approach

In the Euler-Euler approach, the different phases are treated mathematically as interpenetrating continua. Since the volume of one phase cannot be occupied by the other phases, it is convenient to introduce the concept of phase volume fractions. These volume fractions are assumed to be continuous functions of space and time, and their sum is equal to one. Conservation equations for each phase are derived to obtain a set of governing partial differential equations, which have a similar structure for all phases. These equations are closed by providing constitutive relations that are obtained from empirical information or from some theoretical arguments.

In FLUENT, three different Euler-Euler multiphase models are available: the Volume of Fluid (VOF) model, the mixture model, and the Eulerian model.

3.1.1 *The Eulerian Model*

The Eulerian model is the most complex of the multiphase models in FLUENT. The Eulerian multiphase model allows for the modeling of separate, yet interacting phases. The phases can be liquids, gases or solids in nearly any combination, and all phases are treated as continua. For n phases, it solves n sets of momentum and continuity equations, one set for each phase. Coupling is achieved through the pressure and interphase exchange coefficients. The manner in which this coupling is handled depends upon the type of phases involved; granular (fluid-solid) flows are handled differently than non-granular (fluid-fluid) flows. Momentum exchange between the phases is also dependent upon the type of the mixture being modeled. An Eulerian treatment is used for each phase, in contrast to the Eulerian-Lagrangian treatment that is used with the discrete phase model.

With the Eulerian multiphase model, the number of phases is limited only by memory requirements and convergence behaviour. Any number of secondary phases can be modeled, provided that sufficient memory is available. For highly complex multiphase flows, however, the solution may be limited by convergence behaviour.

3.1.2 *The Mixture Model*

The mixture model is designed for two or more phases (fluid or particulate). As in the Eulerian model, the phases are treated as interpenetrating continua. The mixture model solves one set of momentum equations, referred to as the mixture momentum equations.

The mixture model is a simplified multiphase model that can be used to model multiphase flows where the phases move at different velocities, but assume local equilibrium over short spatial length scales. The coupling between the phases should be strong. It can also be used to model homogeneous multiphase flows with very strong coupling and with the phases moving at the same velocity.

The mixture model can model n phases by solving the momentum, continuity, and energy equations for the mixture, the volume fraction equations for the secondary phases, and algebraic expressions for the relative velocities. Typical applications include

sedimentation, cyclone separators, particle-laden flows with low loading, and bubbly flows where the gas volume fraction remains low.

The mixture model is a good substitute for the full Eulerian multiphase model in several cases. Implementation of a full multiphase model may not be feasible when there is a wide distribution of a particulate phase or when the interphase laws are unknown or their reliability is questionable. In such cases a simpler model like the mixture model can perform as well as a full multiphase model while solving a smaller number of variables than the full multiphase model.

3.1.3 *The VOF Model*

The Volume of Fluid (VOF) model uses a surface-tracking technique applied on a fixed Eulerian mesh. It is designed for two or more immiscible fluids where the position of the interface between the fluids is of particular interest. In the VOF model, a single set of momentum equations is shared by the fluids, and the volume fraction of each of the fluids in each computational cell is tracked throughout the domain.

The VOF formulation relies on the assumption that two or more fluids (or phases) are not interpenetrating. For each additional phase added to the model, the volume fraction of the phase in the computational cell is introduced. In each control volume, the volume fractions of all phases sum to unity. The fields for all variables and properties are shared by the phases and represent volume-averaged values, as long as the volume fraction of each of the phases is known at each location. Thus the variables and properties in any given cell are either purely representative of one of the phases, or representative of a mixture of the phases, depending upon the volume fraction values.

Typical VOF applications include the prediction of jet breakup, the motion of large bubbles in a liquid, the motion of liquid after a dam break, and the steady or transient tracking of any liquid-gas interface.

3.2 Euler-Lagrange Approach

In the Euler-Lagrange approach, the fluid phase is treated as a continuum governed by the time-averaged Navier-Stokes equations, while the dispersed phase is

solved by tracking a large number of particles, bubbles, or droplets through the calculated flow field. The fluid and dispersed phases can exchange momentum, mass, and energy.

The Lagrangian discrete phase model (DPM) in FLUENT follows the Euler-Lagrange approach. In addition to solving the transport equations for the continuous phase, FLUENT simulates the discrete second phase in a Lagrangian frame of reference. This second phase consists of spherical particles (which may be taken to represent droplets or bubbles) that disperse throughout the continuous phase. FLUENT computes the trajectories of these discrete phase entities, as well as heat and mass transfer to and from them. Coupling between the phases and its impact on both the discrete phase trajectories and the continuous phase flow can be included. The droplet or particle trajectories can be computed individually at specified intervals during the fluid phase calculation.

A fundamental assumption made in the Euler-Lagrange model is that the dispersed second phase occupies a low volume fraction, even though high mass loading is acceptable.

3.3 Summary

According to the description in sections 3.1.1 – 3.1.3, the Eulerian model should be applied for the simulation of the complete paint spray process. But the reality is that it may not be affordable to use an Euler–Euler approach for the simulation on the whole spray process, due to the high cost associated with such calculations and the available computational resources. On the other hand, the discrete phase model cannot be applied for the whole process because (i) the paint inside the atomizer is continuous and there are no droplets, i.e., no dispersed phase, before atomization, and (ii) the discrete phase model cannot be used to simulate the atomization process.

A three-step procedure has been devised in the present study to accomplish the simulation of the complete paint spray process. The spray simulation in each region (see Figure 1.4) was treated with a different approach and modeled separately. An Euler-Euler model can be used to simulate the flow inside the atomizer (disintegration region) to predict the initial droplet size and velocities at the edge of the atomizer. These predicted

droplet properties are then taken to set the boundary and initial conditions for the droplet transfer simulation in the fully developed spray region, using the Euler-Lagrange approach and the discrete phase model. Finally, information related to the paint deposition on the target plate can be used to calculate the paint film thickness profiles and transfer efficiency.

CHAPTER 4 SIMULATION OF FLOW IN THE ATOMIZER

As indicated in previous chapters, a single simulation of the complete paint spray process, from inlet to target plate, is not feasible or practical. In order to simulate the flow in the fully developed spray region (see Figure 1.4), the paint particle size and velocities entering the spray region must be known. Of course, initial droplet sizes and velocities can be obtained through experiment. However, as discussed in Chapter 1, the expense involved in setting up and conducting experiments motivates one to consider a numerical method to acquire these droplet properties. Thus, in this chapter, we develop a numerical procedure to determine the flow in the high-speed rotary bell-shape atomizer, with particular emphasis on predicting the sizes and velocities of paint droplets leaving the outer rim of the bell cup.

Paint is supplied into the rotating atomizer from the end connected to the nozzle (see Figure 4.1). The paint attains its rotational speed because of the friction between the fluid and the wall of the atomizer. The centrifugal force pushes the paint towards the outer wall. At low rotational speed conditions, the paint will be sprayed into the air from both the central hole and the ring jet close to the rim. If the rotational speed is high enough, the paint will form a thin continuous film and leave the atomizer only at the rim of the bell cup, and the central hole will suck the air back into the atomizer. This indicates that a two-phase flow exists inside the atomizer. Thus, in order to determine the initial droplet sizes near the edge of the bell cup atomizer, a two-phase (paint and air) simulation should be conducted. Furthermore, since the paint is indirectly charged by the electrodes surrounding the nozzle, the electrostatic field can be neglected because it has no effect on the paint within the atomizer.

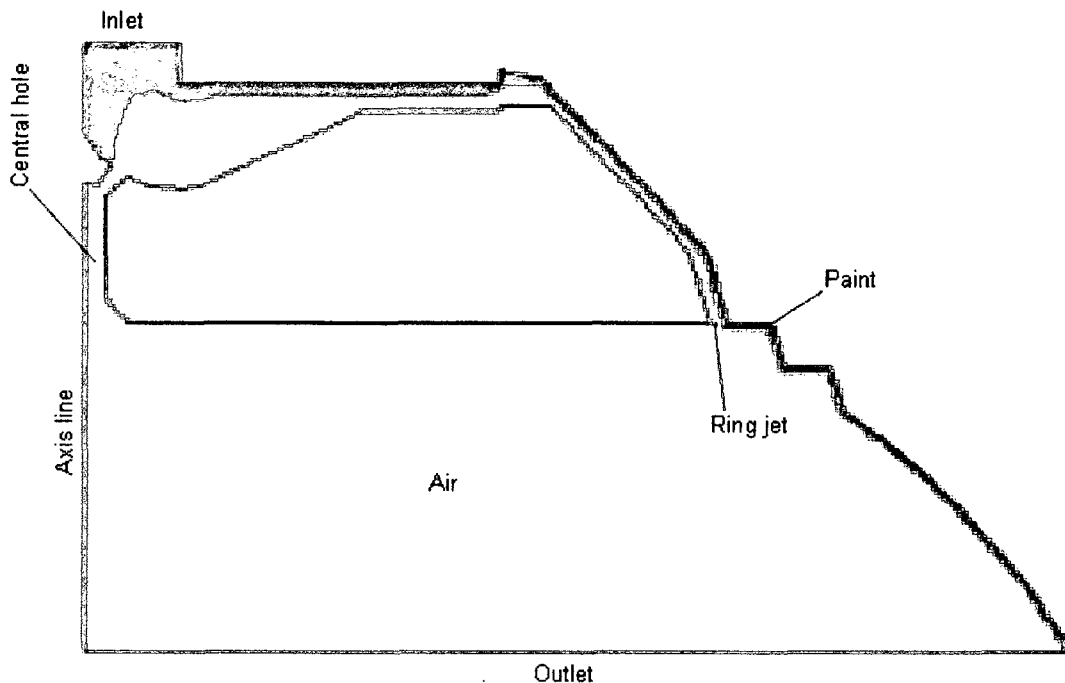


Figure 4.1 Schematic Meridian View of the Bell-shape Atomizer

As an initial test, FLUENT was used to set up a two-dimensional, two-phase simulation in the atomizer. Because the atomizer rotates at very high speed and there is no moving blade inside, the paint and air do not mix with each other in the atomizer. Since the VOF model is good for modeling immiscible fluids and is less computationally intensive compared to the other two multiphase models described in Chapter 3, it was selected for this simulation. The results of this simulation indicate that the paint is ejected from the ring jet, while air is sucked in through the central hole. However, this test case also demonstrated that even the two-dimensional, two-phase simulation using VOF model is still computationally expensive. In order to obtain the solution for this highly rotational two-phase flow, an unsteady solver, extremely small under-relaxation factors and very fine grids are required. All of these requirements place a high demand on computing resources. Thus, from an industrial perspective, a two-phase three-dimensional simulation of the flow in the atomizer may not be practical if an alternative can be found. Furthermore, a three-dimensional pure paint simulation in the atomizer also shows that paint flows out from the ring jet and that the paint flow direction reverses at

the central hole for high rotational speeds. These test simulations show that a dead zone develops at the entrance to the central hole channel, effectively blocking the mixing of the fluid entering through the inlet with that which flows through the channel. Thus, it is reasonable to assume that paint entering the atomizer from the inlet is not significantly affected by the type of fluid (paint or air) sucked in from the central hole of the atomizer at high rotating speeds. The flow of the paint entering from the inlet remains essentially the same regardless of whether a single-phase (pure paint) simulation or a two-phase (paint and air) simulation is performed. This makes it possible to derive the droplet sizes and other flow properties based on a pure paint steady flow simulation in the bell cup.

4.1 The Computational Domain

The physical domain is approximately conical with four small channels uniformly located along the circumferential direction at the centre of the atomizer, converging to the central hole of the atomizer downstream. Therefore, a one-fourth slice of the atomizer domain was chosen for the computation. Periodic boundary conditions were specified on both sides of the slice. Generally speaking, for a complicated irregular domain, it is easier to create a tetrahedral mesh rather than a hexahedral mesh. However, in order to meet the mesh quality requirements, such as small skewness, smoothness of cell volume change and at least five cells in a flow passage, the number of cells of a tetrahedral mesh needed for this bell cup would be more than 3 million. Furthermore, the convergence for solving the high-swirling flow based on a tetrahedral mesh is very slow. By using a hexahedral mesh, larger cell dimensions can be applied in the circumferential direction and along the wall of the ring jet, without jeopardizing the convergence and accuracy. Thus, a hexahedral mesh was created because it significantly reduced the total amount of cells needed for accurate simulation. The mesh is block-structured and was created using ANSYS ICEM CFD HEXA. There are 341,325 cells in the mesh (see Figure 4.2).

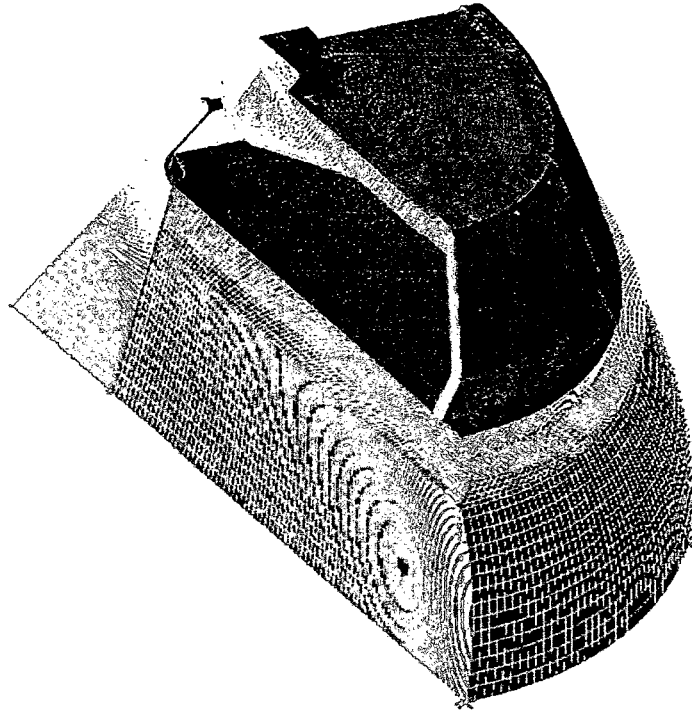


Figure 4.2 Mesh for One Quarter of the Atomizer

4.2 Numerical Algorithm

The momentum equations of fluid flow are known as the Navier-Stokes equations and can be written as

$$\rho \left(\frac{\partial u}{\partial t} + u \frac{\partial u}{\partial x} + v \frac{\partial u}{\partial y} + w \frac{\partial u}{\partial z} \right) = -\frac{\partial p}{\partial x} + \rho g_x + \mu \left(\frac{\partial^2 u}{\partial x^2} + \frac{\partial^2 u}{\partial y^2} + \frac{\partial^2 u}{\partial z^2} \right) \quad (4.1a)$$

$$\rho \left(\frac{\partial v}{\partial t} + u \frac{\partial v}{\partial x} + v \frac{\partial v}{\partial y} + w \frac{\partial v}{\partial z} \right) = -\frac{\partial p}{\partial y} + \rho g_y + \mu \left(\frac{\partial^2 v}{\partial x^2} + \frac{\partial^2 v}{\partial y^2} + \frac{\partial^2 v}{\partial z^2} \right) \quad (4.1b)$$

$$\rho \left(\frac{\partial w}{\partial t} + u \frac{\partial w}{\partial x} + v \frac{\partial w}{\partial y} + w \frac{\partial w}{\partial z} \right) = -\frac{\partial p}{\partial z} + \rho g_z + \mu \left(\frac{\partial^2 w}{\partial x^2} + \frac{\partial^2 w}{\partial y^2} + \frac{\partial^2 w}{\partial z^2} \right) \quad (4.1c)$$

where ρ is the density of the fluid, p is the pressure, μ is the viscosity, u , v , and w are velocities in x , y , and z directions respectively, and g_x , g_y and g_z are gravitational acceleration in x , y , and z directions respectively.

FLUENT, which is based on the finite volume method, has been implemented to solve the 3D Navier-Stokes equations (4.1). The steady state segregated solver, the cell-centre scheme, SIMPLE pressure-velocity coupling and first order upwind discretization scheme were used. The realizable $k - \epsilon$ turbulence model was used rather than the standard $k - \epsilon$ turbulence model because of the strong swirl in the bell atomizer. Because the thickness of the paint film (see Figure 4.3) is very small, very fine cells close to the bell wall are required for the accurate calculation of the film thickness. These small cell sizes along the wall resulted in a small y^+ value, which called for the enhanced wall treatment option in FLUENT. Mass flow rate inlet boundary condition and pressure outlet boundary condition with “Radial Equilibrium Pressure Distribution” were specified. When the “Radial Equilibrium Pressure Distribution” feature is active, the specified gauge pressure applies only to the position of minimum radius (relative to the axis of the rotation) at the boundary. The static pressure on the rest of the outlet zone is calculated from the assumption that radial velocity is negligible, so that the pressure gradient is given by

$$\frac{\partial p}{\partial r} = \frac{\rho v_\theta^2}{r} \quad (4.2)$$

where r is the radial distance from the centre of the bell and v_θ is the tangential velocity.

4.3 Droplet Properties at the Atomizer Edge

Since the paint entering the atomizer from the inlet is blocked and deflected by the fluid (paint or air) sucked in from the central hole of the atomizer at high rotating speed, as discussed previously, the paint from the inlet flows along the outer wall and forms a paint film, regardless of whether a single-phase (pure paint) simulation or a two-

phase (paint and air) simulation is performed. Thus a single-phase (paint) simulation has been used to calculate the paint flow characteristics at the edge of the bell cup. The electrostatic field has been neglected since it has no effect on the paint within the atomizer.

Once the simulation has been completed, the blob diameters and velocities at the bell cup edge can be estimated by employing the following steps:

1. Assume an initial film thickness δ_0 .
2. Construct an annular zone at the bell edge plane with outer radius R and inner radius $R - \delta_0$, where R is the radius of the bell cup at the edge (see Figure 4.3).
3. From the FLUENT simulation, determine the average axial velocity v_a of this annular zone.
4. Calculate the film thickness δ from the following equation:

$$\delta = \frac{\dot{Q}}{2\pi\rho_p(R - \frac{\delta_0}{2})v_a} \quad (4.3)$$

where \dot{Q} is the paint mass flow rate at the inlet and ρ_p is the paint density.

5. If $\delta \neq \delta_0$, let $\delta_0 = \delta$ and go to step 2. Otherwise, stop the calculation.

A flow chart of this procedure is described in Figure 4.4.

The calculated film thickness value can be used to estimate the paint droplet size at the edge of the bell cup. The three-dimensional velocities within the paint film can be adopted as inlet droplet velocities for subsequent calculations in the fully developed spray region between the atomizer and the target plate, as described in Chapter 5.

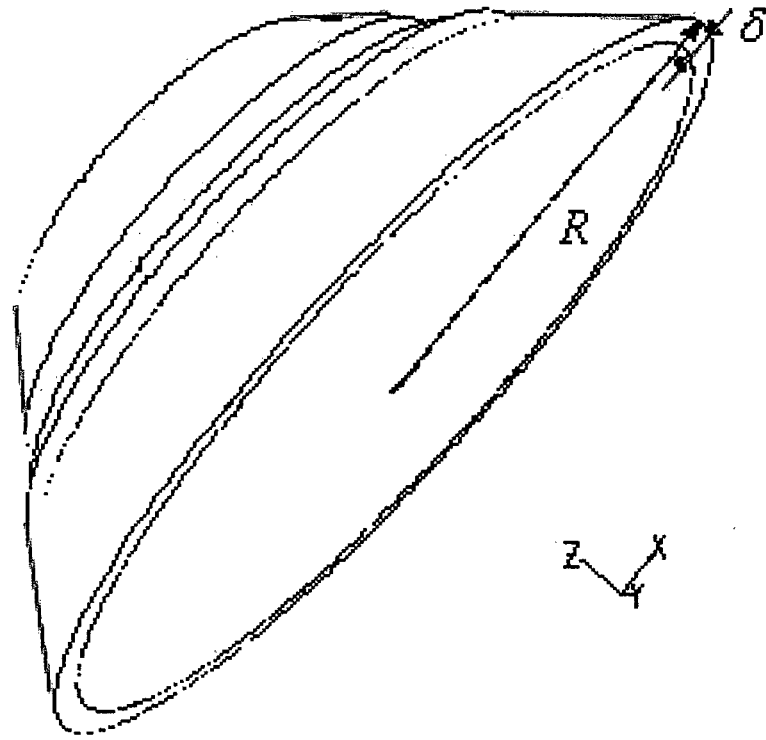


Figure 4.3 3D Illustration of Paint Film Thickness at the Bell Edge

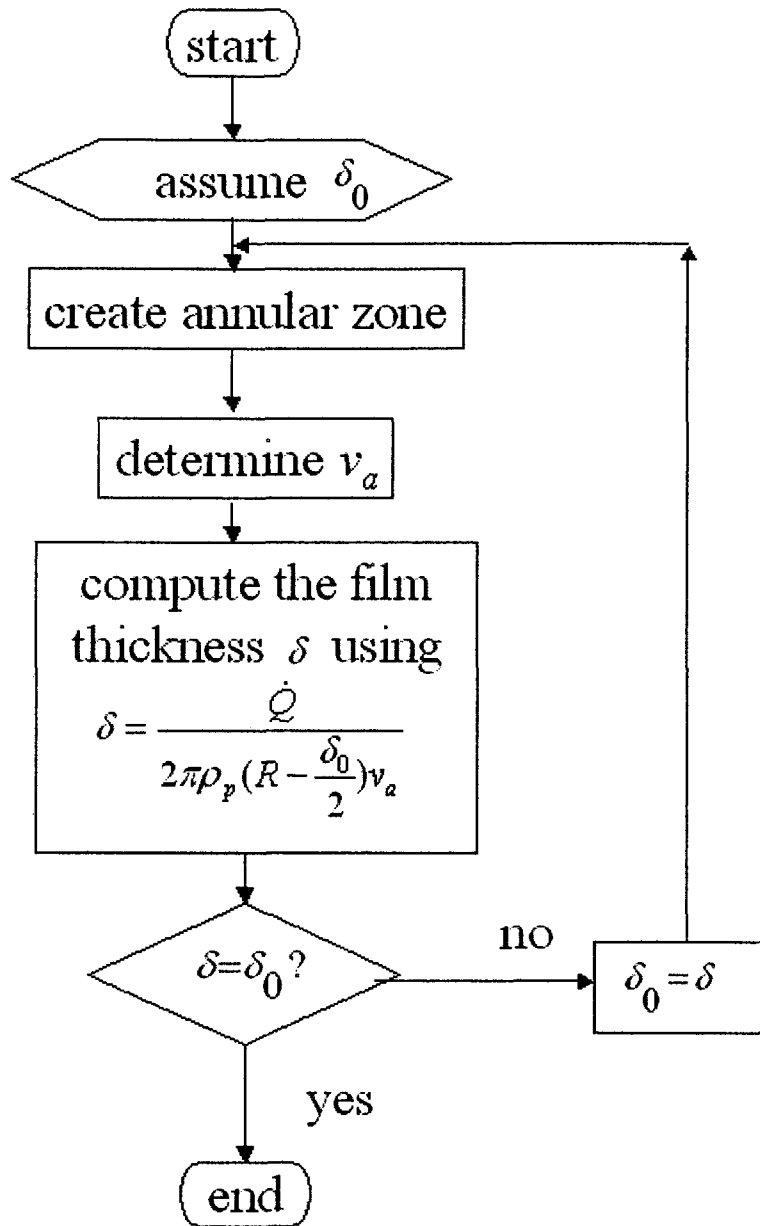


Figure 4.4 Flow Chart for Calculating the Paint Film Thickness at the Bell Edge

4.4 Simulation Conditions

The paint density and viscosity are taken as 1241 kg/m^3 and 0.065 kg/(m*s) , respectively. Numerical simulations of the flow in the atomizer were performed at

different operating conditions, by varying paint flow rate and bell rotating speed. Fixing the paint flow rate at 150 cc/min, the cases given in Table 4.1 were considered.

Bell Rotating Speed (rpm)
25000
30000
34000
38000
44000
50000
55000
60000

Table 4.1 Numerical Simulation Conditions for Paint Flow Rate of 150 cc/min

Specifying the bell rotation speed at 38000 rpm, the simulation cases outlined in Table 4.2 were carried out.

Paint Flow Rate (cc/min)
100
150
200
240
250
300
320

Table 4.2 Numerical Simulation Conditions for Bell Rotating Speed of 38000 rpm

4.5 Results and Discussion

Velocity vectors on a meridian plane are displayed in Figure 4.5, with a closeup view of the inlet region shown in Figure 4.6. The reversing flow in the central hole channel and the dead zone are labeled in these two figures, confirming that the paint

injected at the inlet moves along the outer wall of the bell cup. These velocity vectors are coloured by velocity magnitude (m/s).

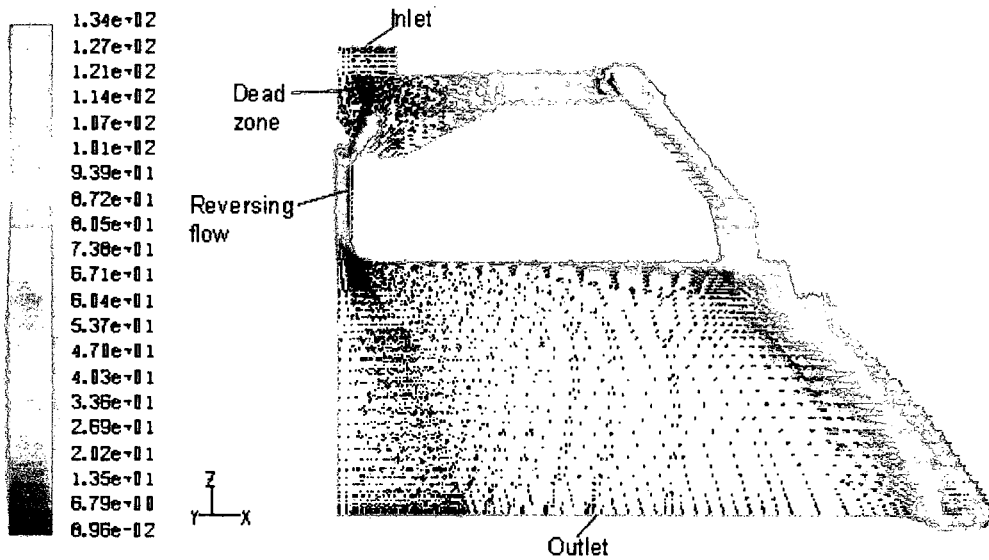


Figure 4.5 Velocity Vectors on a Meridian Plane of the Bell-shape Atomizer

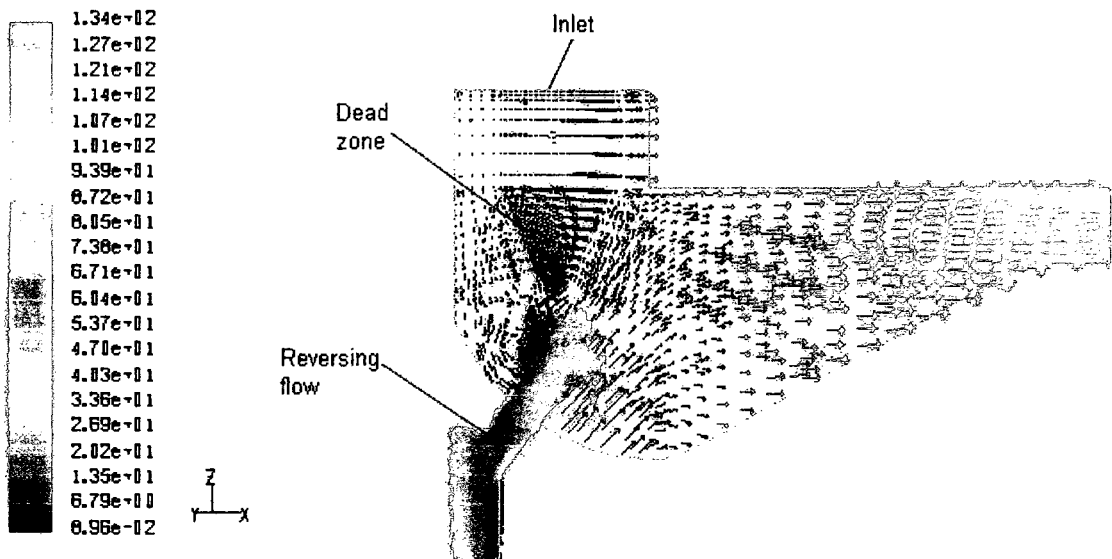


Figure 4.6 Velocity Vectors on a Meridian Plane near the Inlet of the Bell-shape Atomizer

The Reynolds numbers, based on rotational speed and diameter of the bell cup, of this study are approximately 10^7 . The width of the films obtained by the procedure outlined in Section 4.3 is in the range of 6 to 12 micron. This film thickness agrees very

well with data published by Domnick and Thieme (2004) (see Figure 4.7), which shows the film thickness varying between 15 micron at Reynolds number 10^6 to around 5 micron at Reynolds number of 10^7 .

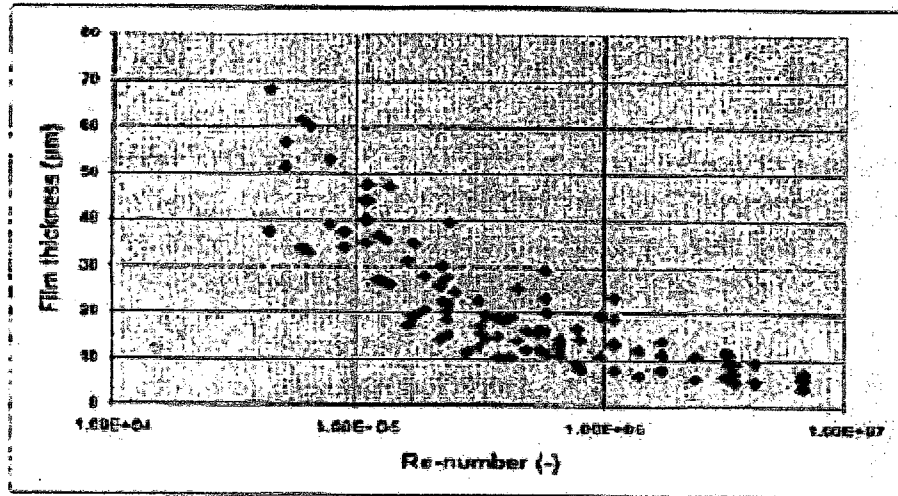


Figure 4.7 Film Thickness at the Bell Edge as a Function of Reynolds Number [from Domnick & Thieme (2004)]

The variations of the calculated droplet size with bell rotational speed and paint flow rate are presented in Figure 4.8 and Figure 4.9. These figures indicate that, over the range of parameters considered, the droplet size increases linearly with the paint flow rate and decreases linearly with the rotational speed of the bell cup. This trend was also observed experimentally by Bauckage et al. (1994 & 1995) and predicted numerically by Im (1999) and Im et al. (2004).

The predicted droplet velocities are plotted in Figure 4.10 – Figure 4.13. The droplet velocity magnitude at the edge of the atomizer is dominated by the tangential component, increasing with the increase of bell rotational speed and decreasing as the flow rate increases.

The droplet size and velocities in Figure 4.8 - Figure 4.13 show a linear relation with the horizontal coordinate variables. Using the least square curve fit method, these linear relations can be summarized in the formula

$$y = ax + b . \tag{4.4}$$

Table 4.3 shows the coefficients and R^2 values of the linear least square curve fit for variables in Figure 4.8 - Figure 4.13.

Relationship	Slope a	Intercept b	R^2	Fig. No.
Droplet size vs. bell rotational speed	-0.0001	12.39	0.9924	4.8
Droplet size vs. paint flow rate	0.0238	4.5366	0.9931	4.9
Droplet axial velocity vs. bell rotational speed	2E-05	0.5673	0.9933	4.10
Droplet radial velocity vs. bell rotational speed	1E-05	0.2969	0.9915	4.10
Droplet axial velocity vs. paint flow rate	0.0041	0.7962	0.9661	4.11
Droplet radial velocity vs. paint flow rate	0.0021	0.416	0.9731	4.11
Droplet tangential velocity vs. bell rotational speed	0.0034	-0.2239	1	4.12
Droplet tangential velocity vs. paint flow rate	-0.017	132.75	0.9445	4.13

Table 4.3 Coefficients and R^2 Values of Linear Curve Fit

It can be seen that all the R^2 values are close to 1, which indicates there are strong linear relations for these data.

The spray angle θ is defined as

$$\theta = \tan^{-1}\left(\frac{v_r}{v_a}\right) \quad (4.5)$$

where v_a is the axial velocity of the droplet and v_r is the radial velocity of the droplet. The variation of the calculated spray angle with bell rotational speed and inlet flow rate are presented in Figure 4.14 and Figure 4.15. The spray angle is determined by both the axial and radial components of the droplet velocity. Its value remains approximately constant at 27.5° over a typical range of flow rates and rotating speeds.

4.6 Conclusions

This chapter presents a numerical procedure to calculate the paint droplet sizes and velocities at the edge of the high-speed rotary atomizer, by performing a single-phase paint flow simulation inside the bell cup.

The simulations indicate that the droplet size and velocities vary linearly with rotational speed and flow rate. There is no such linearity observed for the spray angle.

The droplet properties obtained through this procedure can be used as inputs for the droplet transfer simulation. The details of droplet transfer simulation will be discussed in Chapter 5. The results indicate that this method is a good alternative to more expensive droplet measurement experiments.

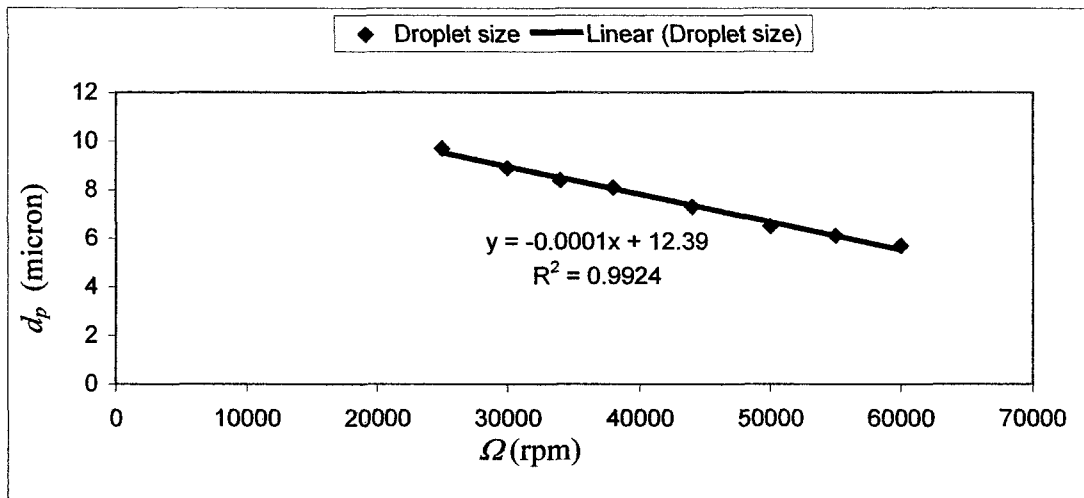


Figure 4.8 Droplet Size vs. Bell Rotation Speed (paint flow rate = 150 cc/min)

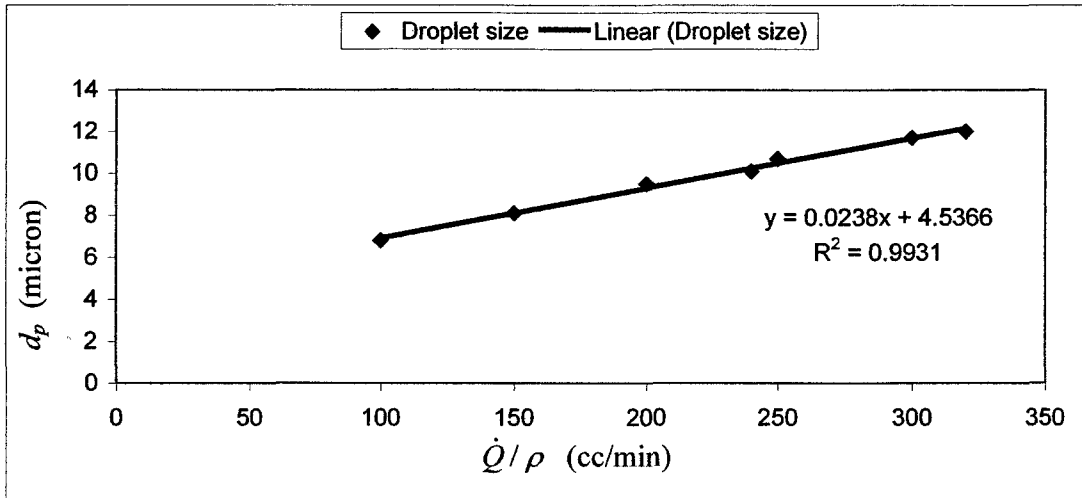


Figure 4.9 Droplet Size vs. Paint Flow Rate (bell rotation speed = 38000 rpm)

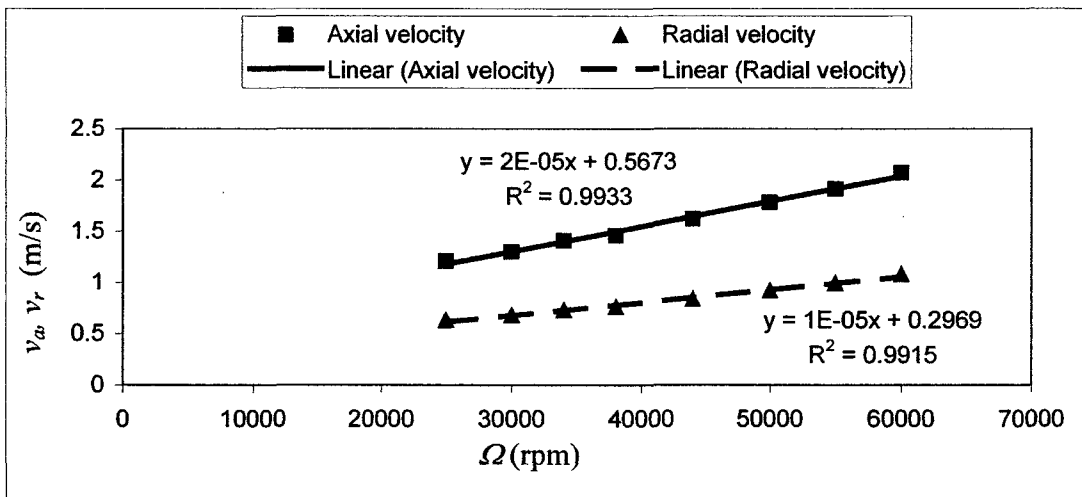


Figure 4.10 Droplet Axial and Radial Velocities vs. Bell Rotation Speed (paint flow rate = 150 cc/min)

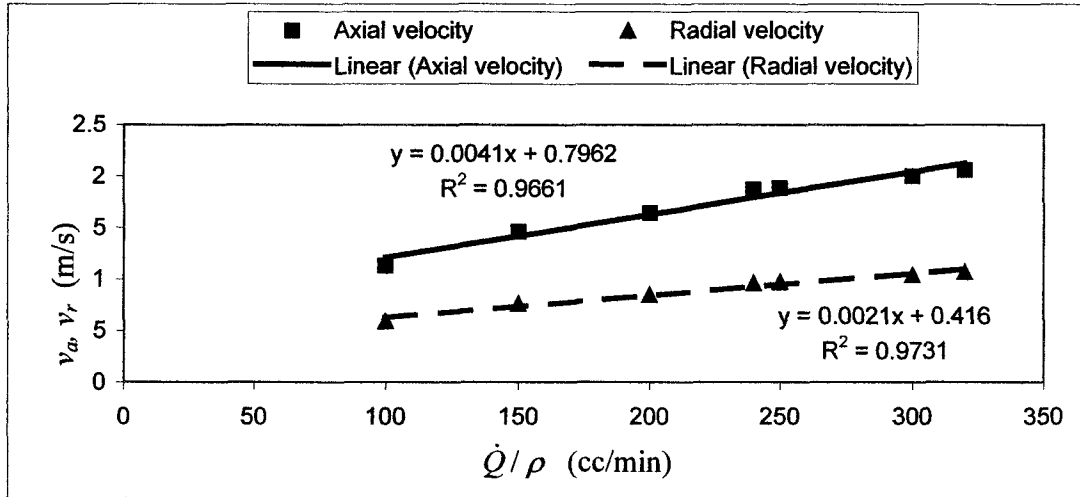


Figure 4.11 Droplet Axial and Radial Velocities vs. Paint Flow Rate (bell rotation speed = 38000 rpm)

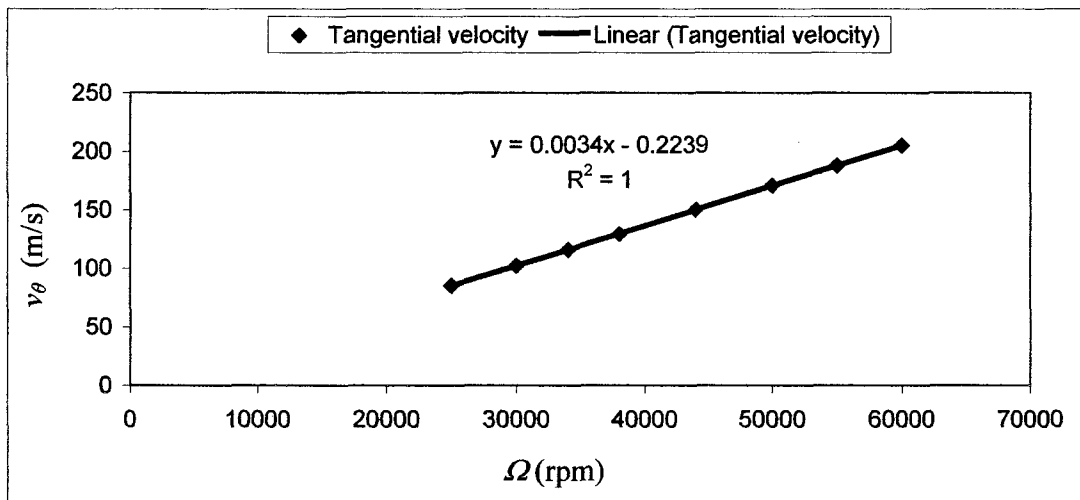


Figure 4.12 Droplet Tangential Velocities vs. Bell Rotation Speed (paint flow rate = 150 cc/min)

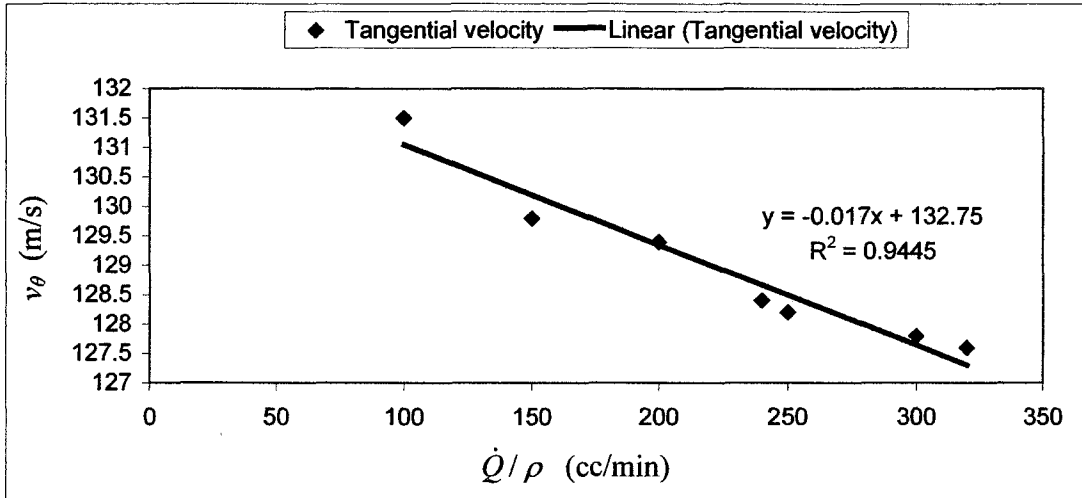


Figure 4.13 Droplet Tangential Velocities vs. Paint Flow Rate (bell rotation speed = 38000 rpm)

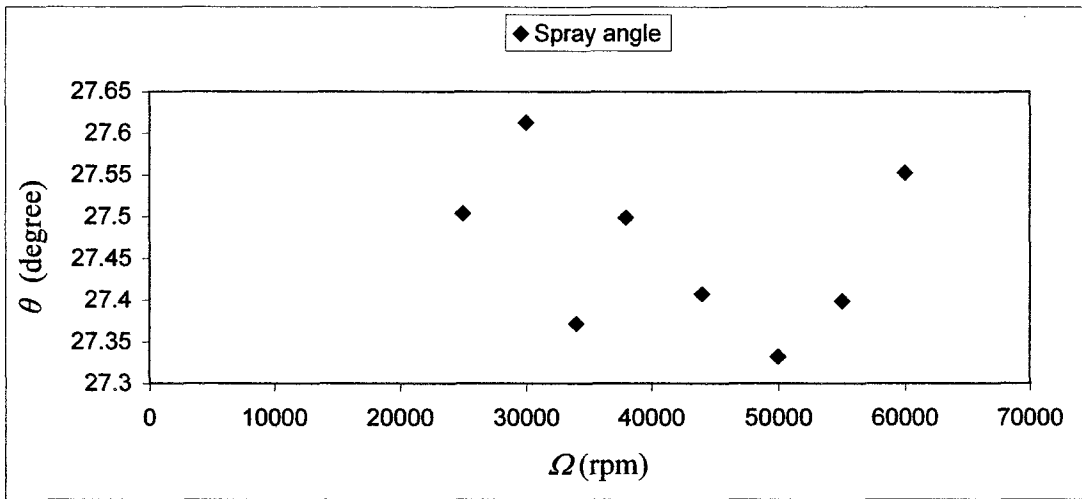


Figure 4.14 Spray Angle vs. Bell Rotation Speed (paint flow rate = 150 cc/min)

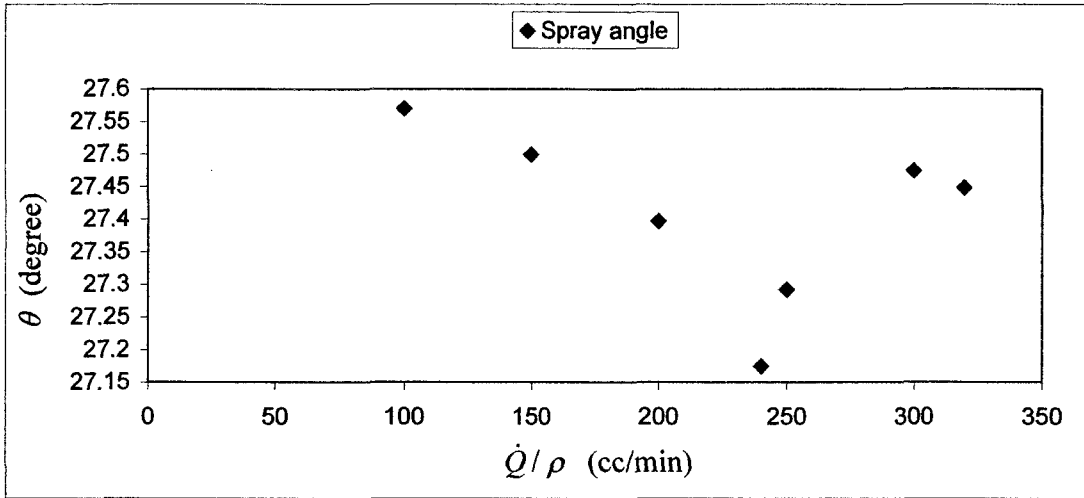


Figure 4.15 Spray Angle vs. Paint Flow Rate (bell rotation speed = 38000 rpm)

CHAPTER 5 DROPLET TRANSFER SIMULATION

In the fully developed spray region, the paint droplets can be viewed as dispersed throughout a continuum of air. In order to simulate the paint droplet transfer process, the discrete phase model of FLUENT, following the Euler-Lagrange approach, was adopted. This approach treats the air and droplets as a continuous phase and a dispersed phase respectively, without solving the Navier-Stokes equations for both phases (see details in Chapter 3), which effectively saves computer resources without sacrificing the accuracy of the droplet transfer process simulation. The Euler-Lagrange approach has been adopted by Bai and Gosman (1995), Dooley et al. (1997), Yarin and Weiss (1995), Mundo et al. (1995c), Huang et al. (2000) and Im (1999) and Im et al. (2001 & 2004) for their investigations of the droplet transfer.

In this chapter, descriptions of FLUENT's discrete phase model, spray models, electrostatic force incorporation, turbulent dispersion modeling, computational domain, numerical algorithm and simulation conditions are presented. Then, discussion and comparison of the air flow field and paint trace under various operating conditions are presented.

For figures shown in this thesis, the units corresponding to the numbers on the colour scale are as follows:

- for pressure, Pa
- for velocity magnitude, m/s
- for electric potential, V
- for electric field strength, V/m
- for droplet residence time, s
- for turbulence kinetic energy, m^2/s^2
- for turbulence dissipation rate, m^2/s^3

5.1 FLUENT's Discrete Phase Model

FLUENT predicts the trajectory of a discrete phase droplet (or particle or bubble) by integrating the force balance on the droplet, which is written in a Lagrangian reference

frame. This force balance equates the droplet inertia with the forces acting on the droplet, and can be written as

$$\frac{d\bar{u}_p}{dt} = f_D(\bar{u} - \bar{u}_p) + \frac{\bar{g}(\rho_p - \rho)}{\rho_p} + \bar{F} \quad (5.1)$$

where $f_D(\bar{u} - \bar{u}_p)$ is the drag force per unit paint droplet mass, \bar{u} is the fluid phase velocity, \bar{u}_p is the paint droplet velocity, ρ is the density of the continuous phase, i.e., air, ρ_p is the density of the paint droplet and \bar{F} is any additional force acting on the droplet, such as lift force, centrifugal force, Coriolis force, etc. The coefficient f_D can be written as

$$f_D = \frac{18\mu C_D \text{Re}_d}{\rho_p d_p^2 24} \quad (5.2)$$

where μ is the viscosity of the fluid, C_D is the drag coefficient and d_p is the droplet diameter. The droplet Reynolds number is defined as

$$\text{Re}_d = \frac{\rho d_p |\bar{u}_p - \bar{u}|}{\mu} . \quad (5.3)$$

Considering the droplet effect on the continuous phase, the momentum equations for the air flow become

$$\rho \left(\frac{\partial u}{\partial t} + u \frac{\partial u}{\partial x} + v \frac{\partial u}{\partial y} + w \frac{\partial u}{\partial z} \right) = -\frac{\partial p}{\partial x} + \rho g_x + \mu \left(\frac{\partial^2 u}{\partial x^2} + \frac{\partial^2 u}{\partial y^2} + \frac{\partial^2 u}{\partial z^2} \right) + F_{D,x} \quad (5.4a)$$

$$\rho \left(\frac{\partial v}{\partial t} + u \frac{\partial v}{\partial x} + v \frac{\partial v}{\partial y} + w \frac{\partial v}{\partial z} \right) = -\frac{\partial p}{\partial y} + \rho g_y + \mu \left(\frac{\partial^2 v}{\partial x^2} + \frac{\partial^2 v}{\partial y^2} + \frac{\partial^2 v}{\partial z^2} \right) + F_{D,y} \quad (5.4b)$$

$$\rho \left(\frac{\partial w}{\partial t} + u \frac{\partial w}{\partial x} + v \frac{\partial w}{\partial y} + w \frac{\partial w}{\partial z} \right) = -\frac{\partial p}{\partial z} + \rho g_z + \mu \left(\frac{\partial^2 w}{\partial x^2} + \frac{\partial^2 w}{\partial y^2} + \frac{\partial^2 w}{\partial z^2} \right) + F_{D,z} \quad (5.4c)$$

where $F_{D,x}$, $F_{D,y}$ and $F_{D,z}$ are components of the droplet force \bar{F}_D in x, y and z directions respectively. \bar{F}_D is the force on the continuous phase exerted by droplets, defined as

$$\bar{F}_D = -f_D(\bar{u} - \bar{u}_p) . \quad (5.5)$$

5.2 Components of the Spray Model

In order to simulate the spray, several types of models need to be selected in advance to account for various aspects of the complex physical phenomena that occur during the spray process.

5.2.1 Injection Model

Because the simulations of paint in the bell cup indicates that the paint is drawn back to the bell cup at the centre, it can be deduced that the droplets are injected into the spray zone only from the rim of the bell cup and form a hollow cone. Thus the “hollow cone injection model” is chosen to simulate the droplet transfer process.

In order to use FLUENT’s hollow cone model, the values of cone angle and swirl fraction need to be specified. In this study, θ described in section 4.5 is taken as the spray angle, determined from

$$\theta = \tan^{-1}\left(\frac{v_r}{v_a}\right). \quad (5.6)$$

Swirl fraction is the fraction of the velocity magnitude that is accounted for by the swirl component of the flow. Therefore, the value of the swirl fraction (S_f) is determined from

$$S_f = \frac{v_\theta}{\sqrt{v_a^2 + v_r^2 + v_\theta^2}} \quad (5.7)$$

where v_a , v_r , and v_θ are axial, radial and tangential velocities of the injected droplet from the bell cup simulation described in Chapter 4.

5.2.2 Droplet Collision Model

FLUENT provides an option for estimating the number of droplet collisions and their outcomes in a computationally efficient manner. The difficulty in any collision calculation is that for N droplets, each droplet has $N - 1$ possible collision partners. Thus,

for large N , the number of possible collision pairs is approximately $\frac{1}{2}N^2$.

Since a spray can consist of several million droplets, the computational cost of a collision calculation for the real number of droplets is prohibitive. This motivates one to consider the concept of parcels. Parcels are statistical representations of a number of individual droplets. For example, if FLUENT tracks a set of parcels, each of which represents 1000 droplets, rather than tracking each individual droplet, the cost of the collision calculation is reduced by a factor of 10^6 .

The algorithm of O'Rourke (1981) is used to calculate the collisions. It efficiently reduces the computational cost of the spray calculation. Rather than using geometry to determine whether parcel paths intersect, O'Rourke's method is a stochastic estimate of collisions. O'Rourke also makes the assumption that two parcels may collide only if they are located in the same continuous-phase cell. These assumptions are valid only when the continuous-phase cell size is small compared to the size of the spray. For these conditions, the method of O'Rourke is second-order accurate at estimating the chance of collisions. The concept of parcels together with the algorithm of O'Rourke makes the calculation of collision possible for practical spray problems. Once it has been decided that two parcels of droplets collide, the algorithm further determines the type of collision. Only coalescence and bouncing outcomes are considered. The probability of each outcome is calculated from the collisional Weber number and a fit to experimental observations. The properties of the two colliding parcels are modified based on the outcome of the collision.

5.2.3 *Spray Breakup Model*

The Taylor Analogy Breakup (TAB) model is used in this study. The TAB model is a classic method for calculating droplet breakup, which is applicable to many engineering sprays. This method is based upon Taylor's analogy (Taylor (1963)) between an oscillating and distorting droplet and a spring-mass system. Table 5.1 illustrates the analogous components.

Spring-Mass System	Distorting and Oscillating Droplet
Restoring force of spring	Surface tension forces
External force	Droplet drag force
Damping force	Droplet viscosity forces

Table 5.1 Analogy between a Spring-Mass System and a Distorting Droplet

The resulting TAB model equation set, which governs the oscillating and distorting droplet, can be solved to determine the droplet oscillation and distortion at any given time. When the droplet oscillations grow to a critical value the “parent” droplet will break up into a number of smaller “child” droplets. As a droplet is distorted from a spherical shape, the drag coefficient will change. A drag model that incorporates the distorting droplet effects is available in FLUENT, and described in the next section.

5.2.4 Drag Model

The spherical drag model is used in this simulation. The drag coefficient C_D in Eq. (5.2) is defined as

$$C_D = a_1 + \frac{a_2}{Re_d} + \frac{a_3}{Re_d^2} \quad (5.8)$$

where a_1 , a_2 and a_3 are constants given by Morsi and Alexander (1972). These constants change with droplet Reynolds number Re_d , for example,

$$C_D = \frac{24}{Re_d} \text{ for } Re_d < 0.1$$

$$C_D = 3.69 + \frac{22.73}{Re_d} + \frac{0.0903}{Re_d^2} \text{ for } 0.1 < Re_d < 1$$

$$C_D = 1.222 + \frac{29.1667}{Re_d} - \frac{3.889}{Re_d^2} \text{ for } 1 < Re_d < 10$$

.....

.....

$$C_D = 0.46 - \frac{490.546}{Re_d} + \frac{57.87 * 10^4}{Re_d^2} \text{ for } 5000 < Re_d < 10000$$

$$C_D = 0.5191 - \frac{1662.5}{Re_d} + \frac{5.4167 * 10^6}{Re_d^2} \text{ for } 10000 < Re_d < 50000 .$$

The droplet Reynolds number Re_d is defined in equation (5.3).

5.3 Electrostatic Force Incorporation

The electrostatic field force on the charged droplet is

$$F = qE \quad (5.9)$$

where q is the charge of the droplet and E is the electric field strength, which is equal to $\frac{\partial\phi}{\partial s}$, where ϕ is electric potential and s is distance. Neglecting the effect of charged droplets on the electrostatic field, the electric potential equation is

$$\nabla^2\phi = 0. \quad (5.10)$$

This equation can be defined and solved using the User Defined Scalar (UDS) transport modeling feature in FLUENT (FLUENT 6.1, UDF Manual).

Charge on the droplet is determined by many factors, including property of the liquid, mass of the droplet, surface area of the droplet, strength of the electrostatic field, etc. Although a comprehensive formula for droplet charge is not available, charge-to-mass ratio ($c_{q,m}$) is a basic parameter that is widely used in charged droplet transfer simulations. In general, the charge-to-mass ratio is not uniform for all the droplets in an electrostatic field. Gemci et al. (2002) measured the charge-to-mass ratio of droplets in a spray of an electrostatic rotary bell atomizer, and plotted these charge-to-mass ratios versus drop diameter (see Figure 5.1 and Figure 5.2). The fluid they used was water. It can be seen that there is no significant difference of charge-to-mass ratio with the change of operating voltage. Since water-based paint is used in the current study and most cases studied in this research are at 70 kV operating voltage, a charge-to-mass ratio vs. drop size function was produced with the least squares curve fit method, using the data in Figure 5.2. The relation between the charge-to-mass ratio and the droplet diameter is:

$$c_{q,m} = \frac{10^{-0.00005*d_p^3 + 0.0052*d_p^2 - 0.1873*d_p + 3.3829}}{1000} \quad (5.11)$$

where d_p is the paint droplet diameter.

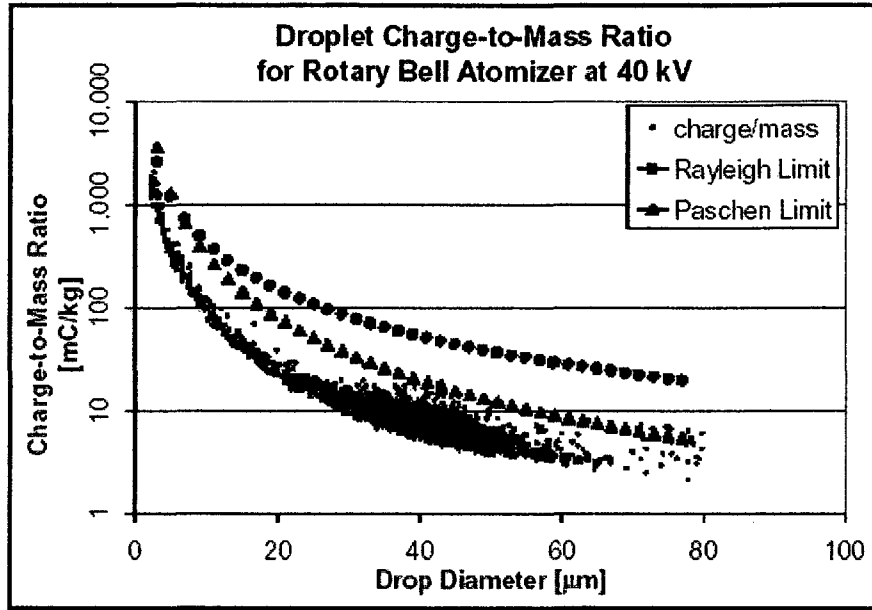


Figure 5.1 Charge-to-Mass Ratio vs. Drop Diameter for the Rotary Bell Atomizer at 40 kV Operating Voltage [from Gemci et al. (2002)]

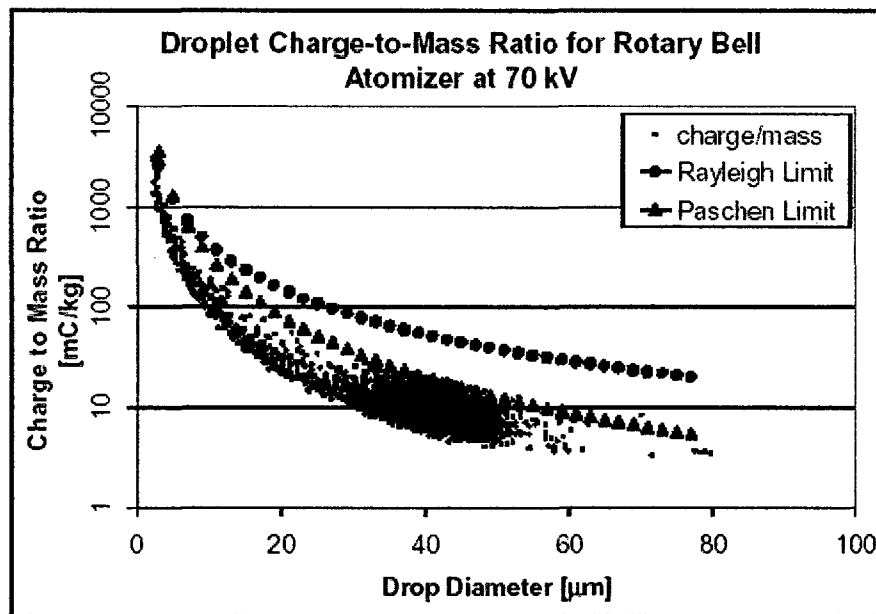


Figure 5.2 Charge-to-Mass Ratio vs. Drop Diameter for the Rotary Bell Atomizer at 70 kV Operating Voltage [from Gemci et al. (2002)]

5.4 Modeling Turbulent Dispersion of Droplets

A stochastic tracking method is used to capture the effects of the turbulent dispersion. In the stochastic tracking approach, FLUENT predicts the turbulent dispersion of droplets by integrating the trajectory equations along the droplet path for individual droplets. By computing the trajectory in this manner for a sufficient number of representative droplets, the random effects of turbulence on the droplet dispersion may be accounted for. In FLUENT, the Discrete Random Walk (DRW) model is used. In this model, the fluctuating velocity components are discrete piecewise constant functions of time. Their random value is kept constant over an interval of time given by the characteristic lifetime of the eddies

5.5 The Computational Domain

Based on the geometric simplicity and features of the flow domain, a cylindrical computational domain was adopted. ANSYS ICEM HEXA was used to create a block-structured mesh. Separate meshes were constructed for the electric field and the flow field simulations. This is appropriate and feasible for the following reasons:

- In order to capture the very small sized electrodes, very small cells must be generated around them.
- Small cells should be created at the inlets and outlets in order to accurately propagate the boundary effects into the domain and obtain acceptable results.
- Viscous stress is dominant and changes rapidly in the wall boundary layer. The effect of the viscous stress plays an important role in the development of the entire flow field. In order to capture the characteristics of the viscous force, a very fine grid is required at wall boundaries.
- In order to achieve accuracy and convergence, a fine mesh is required in the high swirling regions.
- Droplet deposition on the target plate needs to be accurately predicted in order to calculate the film build, which is one of the most important

objectives of this study. Obviously, a coarse mesh along the target plate would be unacceptable.

- The fine grid size for inlets, wall boundary layers, high swirling regions and droplet deposition is not required in a pure electrostatic field simulation. A coarse mesh can be applied in these regions when calculating the electrostatic field.
- Because rapid changes in cell volume between adjacent cells translate into larger truncation errors and perhaps divergence, only meshes with moderate cell volume change can be used.
- Im (1999) reported that although the high electric potential existed near the electrodes, the potential soon became circumferentially uniform away from the electrodes. This indicates that there is no need to use a fine grid aligned to the shape of the electrodes in the fully developed spray region, which significantly reduces the mesh size and makes the droplet transfer simulation over a larger period of physical time feasible.

A single mesh satisfying all the above requirements would have too many cells. The simulation with such a mesh would require too much time and computer resources, so the simulation could only be carried out for a very short physical time period. This would not give a significant film thickness profile and therefore be of little use for the coating industry.

Neglecting the effect of droplet movement on the electrostatic field, it is feasible to solve the electrostatic field using one mesh, and incorporate the obtained electrostatic potential value into the other mesh used for the air flow and droplet transfer simulation.

5.5.1 Mesh for Electrostatic Field Simulation

As mentioned above, one mesh is used just for solving the electrostatic field. The axial length of this computational domain is 0.327 m, which is the distance from the workpiece to the base of the electrode leads. The diameter of the cylindrical domain is 0.9144 m, which is equal to 36 inches, i.e., the width of the workpiece used in the experiments. There are six electrodes located at the top of the domain, represented by six

small cuboids. The bottom of the domain represents the target plate, i.e., the workpiece. There are 632,886 cells in this mesh. Figure 5.3 shows this domain for the electrostatic potential calculation. Figure 5.4 shows a cutaway view, illustrating the mesh distribution.

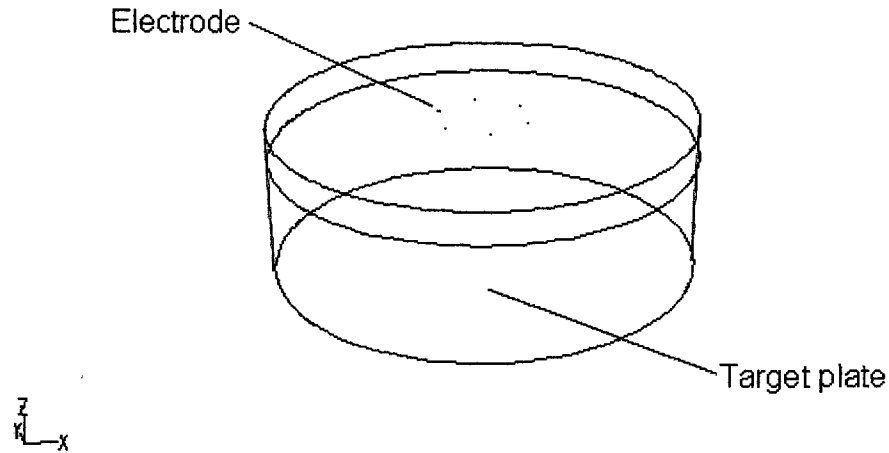


Figure 5.3 Computational Domain for Electrostatic Potential Calculation

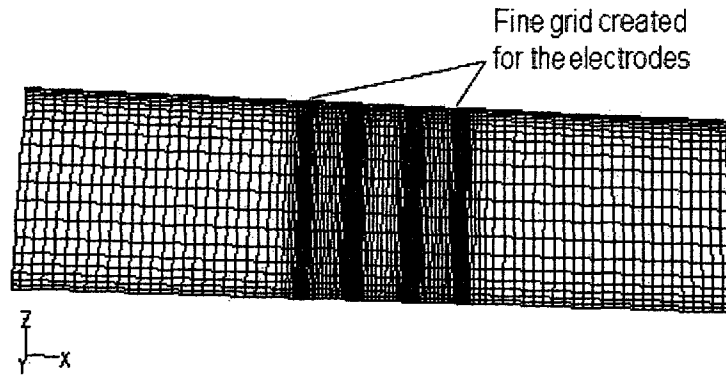


Figure 5.4 Computational Mesh Distribution for Electrostatic Potential Calculation

5.5.2 Mesh for Droplet Transfer Simulation

The second cylindrical domain, used for the droplet and air flow simulation, covers the region from the target plate to the edge of the bell cup, from which the droplets are sprayed. Turbine air, bearing air and shaping air are injected separately from two annular surfaces at the top of this domain. The inlets of turbine air, bearing air and shaping air are located on the same top plane. The droplets are injected along a ring of

0.0682 m diameter, i.e., the inner edge of the bell cup. The axial length of this domain is 0.256 m, 0.071 m shorter than the previous one.

In order to determine the appropriate diameter of the computational domain, two 2-D axisymmetric swirl simulations were executed. The difference between these two simulations is the radial extent of the domains, one is the same as the radius of the target plate, and the other is two times that radius. Applying the same boundary conditions, pure air flow simulations (without droplets) were conducted. Figure 5.5 and Figure 5.6 show static pressure contours for these two simulations. Figure 5.7 and Figure 5.8 show the velocity magnitude contours. Comparison of these contours indicates that there is no significant difference in the results from these two domains. Thus the domain with the same radius as the plate, i.e., 0.4557 m, is adopted in order to reduce the total amount of cells for the paint spray simulation.

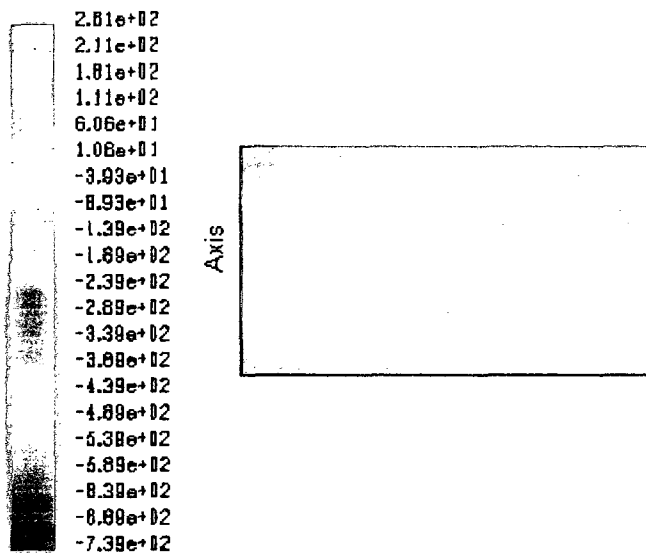


Figure 5.5 Static Pressure Contours from 2D Air Jet Simulation

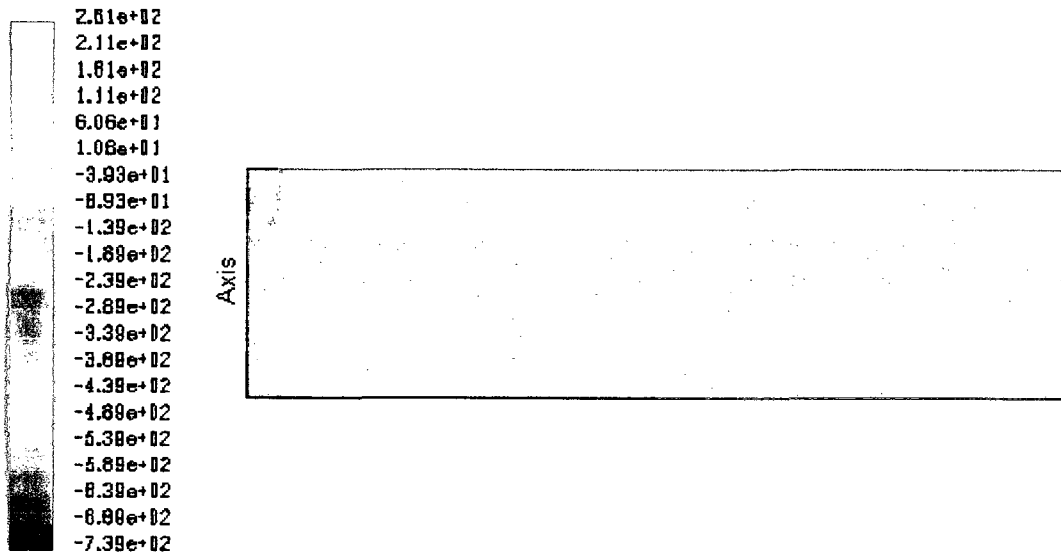


Figure 5.6 Static Pressure Contours from 2D Air Jet Simulation with Extended Domain

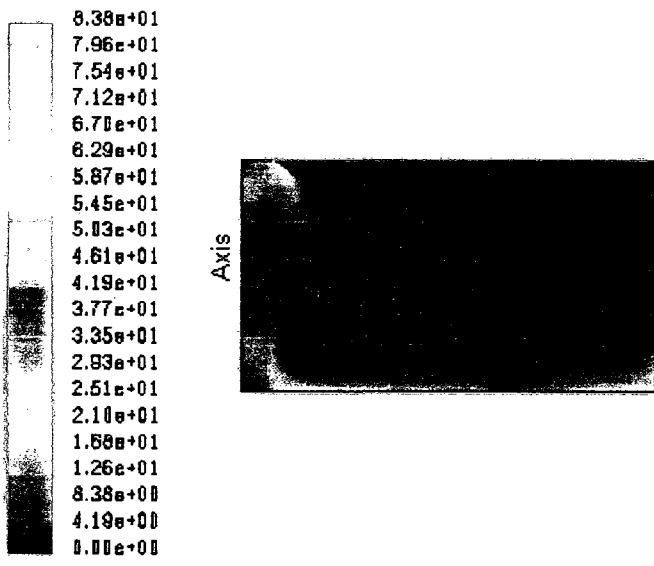


Figure 5.7 Velocity Magnitude Contours from 2D Air Jet Simulation



Figure 5.8 Velocity Magnitude Contours from 2D Air Jet Simulation with Extended Domain

Im (1999) indicated that the high electric potential was concentrated around the six electrodes and that the potential was circumferentially uniform in most of the zone away from the electrodes location. Since the air flow, droplet injection and electrostatic field are all uniform in the circumferential direction, one quarter of the cylindrical domain with circumferentially uniform mesh was used for the droplet transfer simulations so as to further reduce the mesh size of the simulation.

In order to accurately predict the droplet deposition on the target plate, very fine cells near the plate are required. Figure 5.9 shows the mesh distribution for the droplet transfer simulation. The properties of the two meshes are summarized in Table 5.2.

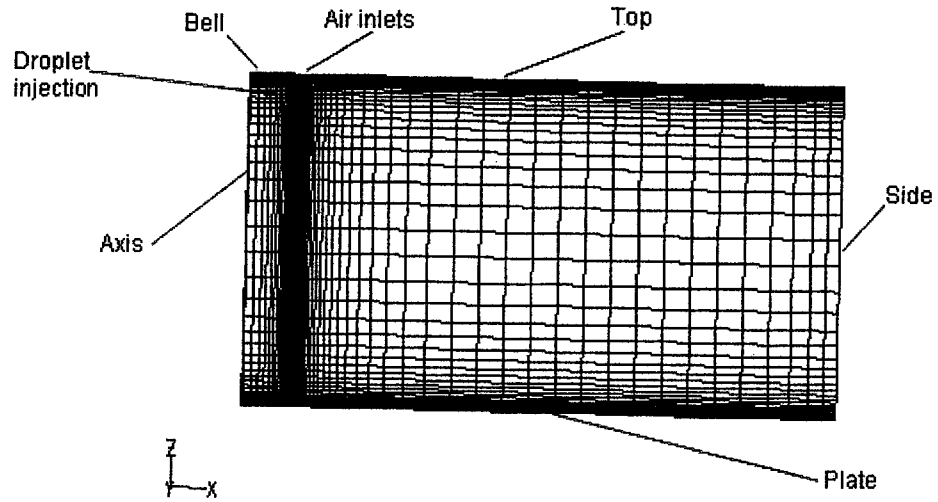


Figure 5.9 Mesh Distribution for Air Flow and Droplet Transfer Simulation

Domain Name	Axial Length (m)	Diameter (m)	Domain Shape	Mesh Size
Electrostatic field domain	0.327	0.9114	Cylindrical	632,886
Droplets and air flow domain	0.256	0.9114	Quarter of cylindrical	103,212

Table 5.2 Characteristics of Electrostatic Field Domain and Flow Domain

5.6 Numerical Algorithm

The numerical algorithm is chosen differently for the electric field simulation and the droplet/air flow simulation.

5.6.1 Numerical Algorithm for Electric Field Simulation

The electric potential was set as a user defined scalar (UDS). The UDS at the surface of the electrodes was set with positive potential values. Zero UDS value was applied at the target plate. Zero UDS flux was specified on the rest of boundaries.

In the electric field simulations, by turning off the flow equations, only the UDS equations are solved, using the finite volume method, with structured hexahedral and prismatic cells. The steady, segregated solver with the cell-centred scheme was implemented.

5.6.2 Numerical Algorithm for Droplet/Airflow Field Simulation

For the droplets/air flow simulation, the electric potential values calculated from the electric field domain were imported, and the potential values at cells in the droplet/air flow mesh were interpolated from the imported data. Using FLUENT's User Defined Function, the three-dimensional electric field strength vector, i.e., gradient of the electric potential, was calculated and stored in User Defined Memory, and the electrostatic force was applied on the droplets as a body force. See UDF1 and UDF2 in Appendix for details.

FLUENT has been used to solve the unsteady 3-D Navier-Stokes equations. Structured hexahedral and prismatic cells, cell-centre scheme, unsteady and segregated solver, SIMPLE pressure-velocity coupling scheme, first order upwind discretization scheme, realizable $k - \epsilon$ turbulence model and enhanced wall treatment are used. In a comparison study, Fogliati (2006) has shown that the realizable $k - \epsilon$ model performs better than the RNG $k - \epsilon$ model. Velocity inlet boundary conditions are specified for the air inlets. The air flow satisfies the no-slip wall boundary condition at the target plate, and pressure outlet boundary is specified at all the other boundaries of the domain. A typical time step for this study is $\Delta t = 0.0005$ s.

When a droplet reaches a boundary (e.g., a wall or outlet boundary), FLUENT applies a discrete phase boundary condition to determine the fate of the trajectory at that boundary. The boundary condition, or trajectory fate, can be defined separately for each boundary. There are three discrete phase boundary conditions available in FLUENT, the “reflect” boundary condition, the “trap” boundary condition and the “escape” boundary condition. “Reflect” means the droplet rebounds off the boundary and goes back into the domain. The trajectory calculation of the droplet continues after reflection. “Trap” implies that the trajectory calculation of the droplet is terminated and the fate of the droplet is recorded as “trapped”. “Escape” indicates the fate of the droplet is reported as “escaped” when it hits the boundary and no more trajectory calculation is done on this droplet. In this study, the discrete phase boundary conditions are set as “escape” at the outlets. The discrete phase boundary conditions are set as “reflect” at the air inlets because the droplets can not leave the domain from the inlets. Since droplets bouncing off the target plate may hit the plate again and only one type of discrete phase boundary condition can be specified at the plate, the “trap” boundary condition is specified at the plate so as to simplify the calculation on the droplet.

5.7 Simulation Conditions

The baseline working conditions for a spray simulation were set as:

- Paint flow rate = 150 cc/min
- Bell rotational speed = 38000 rpm
- Shaping air flow rate = 250 cc/min
- Electrodes potential = 70 kV
- Downdraft air flow speed = 0.31 m/s

A parametric study was carried out by changing some of the parameters while keeping the remaining parameters at the baseline condition. Numerical simulations of the droplet transfer were performed at the conditions summarized in Table 5.3 to Table 5.6. The effect of different spray cone angle, i.e., 22.5°, 27.5° and 32.5° was also tested. The droplet size formula proposed by Domnick and Thieme (2004) estimated the droplet

diameter is about one-tenth of the film thickness at the bell edge. The effect of droplet size was tested by using one-fifth and one-tenth of the droplet film thickness at the bell edge while keeping the rest of the parameters unchanged.

Electrodes Potential (kV)
50
70
90

Table 5.3 Numerical Simulation Conditions of Droplet Transfer Process for Varying Electric Charge

Paint Flow Rate (cc/min)
150
175
200

Table 5.4 Numerical Simulation Conditions of Droplet Transfer Process for Varying Paint Flow Rate

Shaping Air Flow Rate (cc/min)
150
200
250

Table 5.5 Numerical Simulation Conditions of Droplet Transfer Process for Varying Shaping Air Flow Rate

Bell Rotational Speed (rpm)
34000
38000
42000

Table 5.6 Numerical Simulation Conditions of Droplet Transfer Process for Varying Bell Rotational Speed

5.8 Results and Discussion

The results and discussion are organized in the following subsections: (i) electric field simulation, (ii) air and droplet flow fields (baseline conditions), (iii) effect of voltage, (iv) effect of droplet diameter, (v) effect of bell rotational speed, (vi) effect of paint flow rate, (vii) effect of shaping air flow rate, and (viii) effect of spray angle.

5.8.1 *Electric Field Simulation*

Figure 5.10 shows the horizontal view of the electric potential contours at $Z = 0.327$ m, i.e., the top plane of the electric potential simulation domain. It can be seen that the potential close to the six electrodes is high, i.e., 70 kV, and falls dramatically a short distance away from the electrodes.

Figure 5.11 presents the electric potential contours on the plane $Z = 0.2$ m. The electric potential is circumferentially uniform on this plane, which agrees well with the results of Im (1999). Figure 5.12 shows the meridian view of the electric potential. The electric potential is high near the electrodes and falls to 0 V at the target plate. Because this plane does not pass through the electrodes, the highest potential in this figure is 4.91 kV, instead of 70 kV. The electric field strength vectors in a meridian plane are shown in Figure 5.13. The direction of these vectors show that the electric force points outwards in the radial direction close to the electrodes and points downward towards the workpiece in most of the domain. Thus we anticipate that the electric force expands the spray near the sprayer, but confines the spray in most of the domain. Like the electric potential, the field strength diminishes rapidly from the electrodes to the target plate.

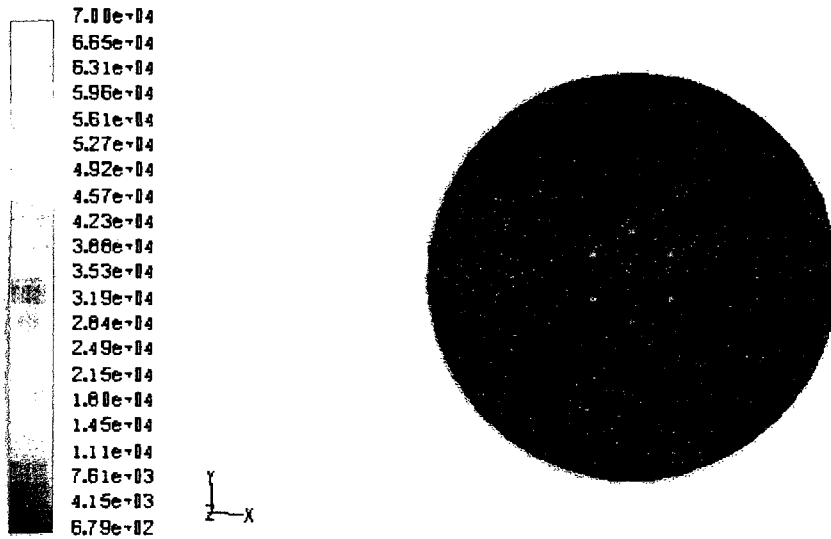


Figure 5.10 Horizontal View of Electric Potential Contours at $Z = 0.327$ m

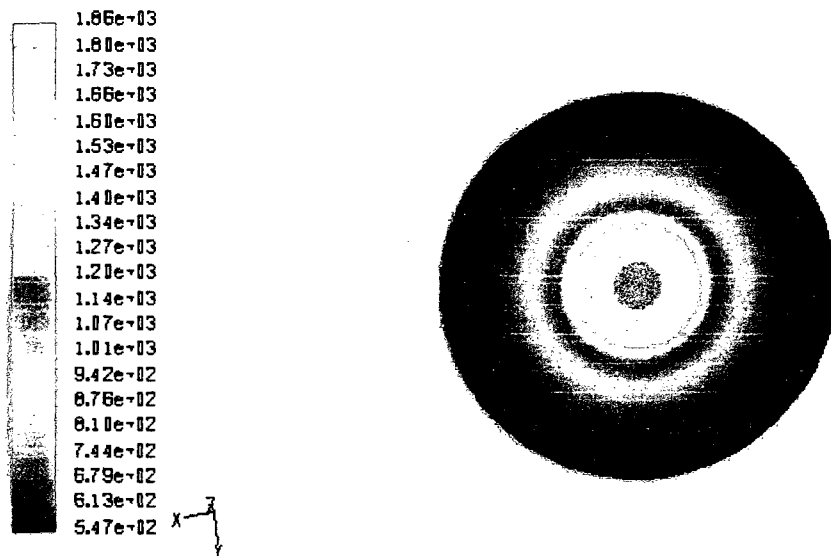


Figure 5.11 Horizontal View of Electric Potential Contours at $Z = 0.2$ m

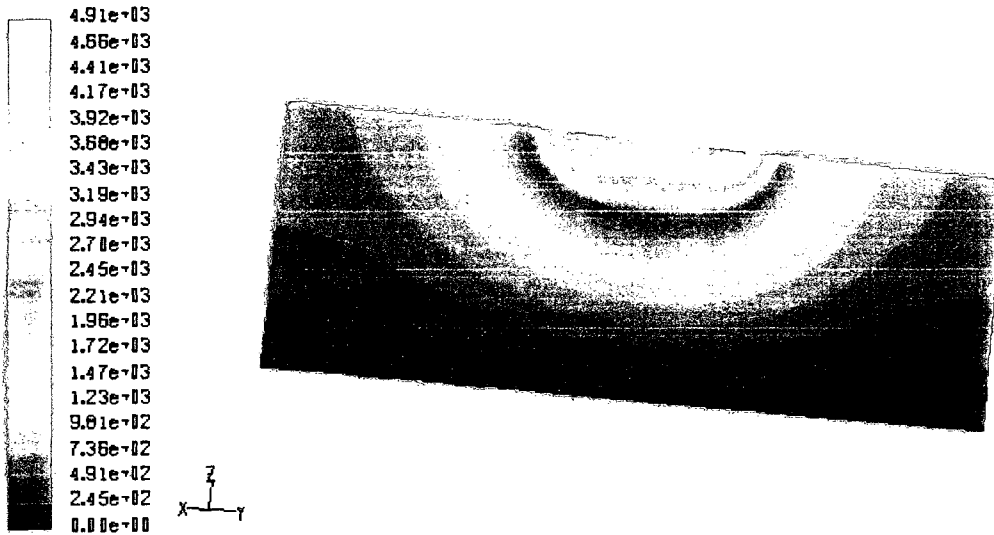


Figure 5.12 Meridian View of Electric Potential Contours

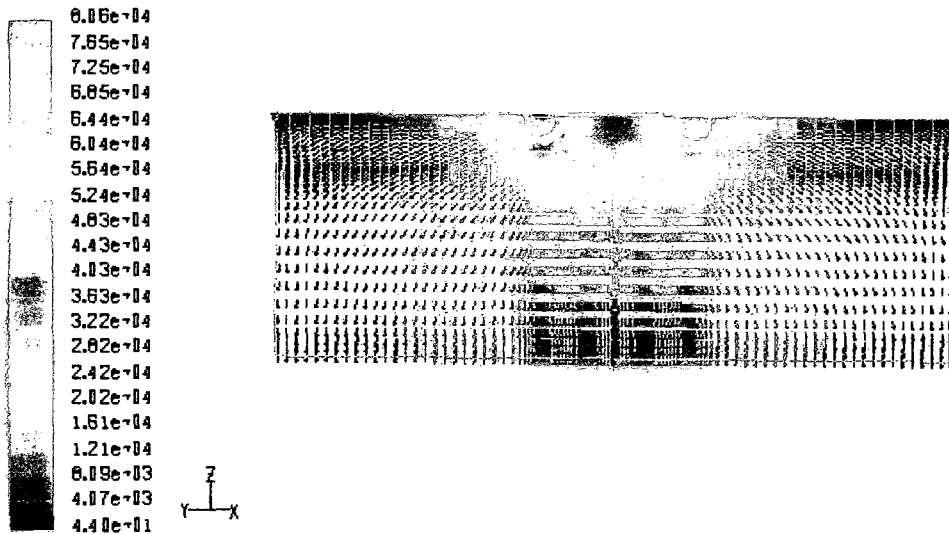


Figure 5.13 Meridian View of Electric Field Strength Vectors

5.8.2 Air and Droplet Flow Fields (Baseline Conditions)

Figure 5.14 shows the static pressure contours on the target plate for a pure air spray simulation on the full cylindrical domain (without paint droplets or electric field). It can be seen, as expected, that the static pressure is circumferentially uniform, with higher pressure near the centre of the plate. We also note that the pressure is essentially constant

over the outer two-thirds of the plate. These observations support the validity of using one quarter of the cylindrical domain for the droplet transfer simulation and applying periodical boundary conditions on the two meridian boundaries.

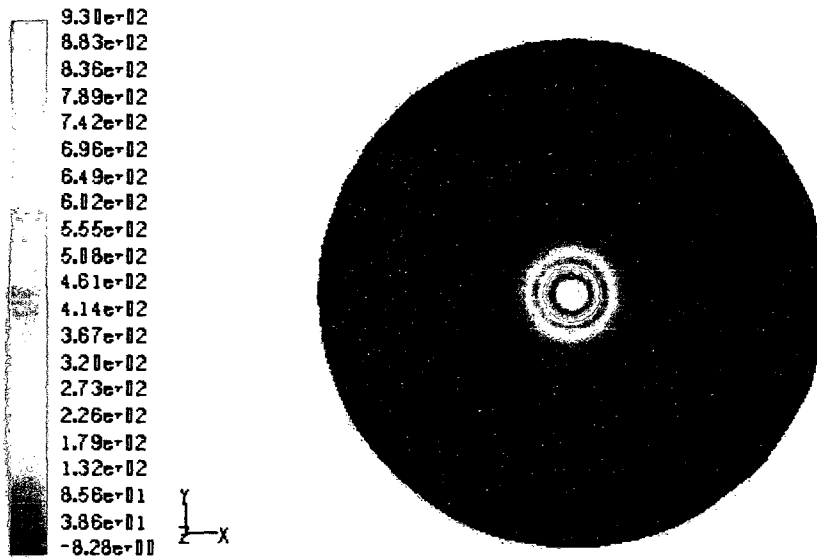


Figure 5.14 Static Pressure Contours on the Target Plate for a Pure Air Spray (shaping air flow rate = 250 cc/min)

Figure 5.15 shows a meridian view of the air velocity vectors of the spray at paint flow rate of 150 cc/min and shaping air flow rate of 250 cc/min (baseline conditions). It illustrates that a large circulation zone forms between the nozzle and workpiece. This circulation zone was also observed experimentally by Bauckage et al. (1994 & 1995) and predicted numerically by Im (1999) and Im et al. (2004). A high velocity zone exists in the vicinity of the strong combined turbine-bearing air inlet. In this and subsequent figures, the range has been clipped in order to see the variation of the parameter in the flow field. The actual velocity magnitude in Figure 5.15 ranges from 0 m/s at the target plate to 86 m/s near the turbine-bearing air inlet.

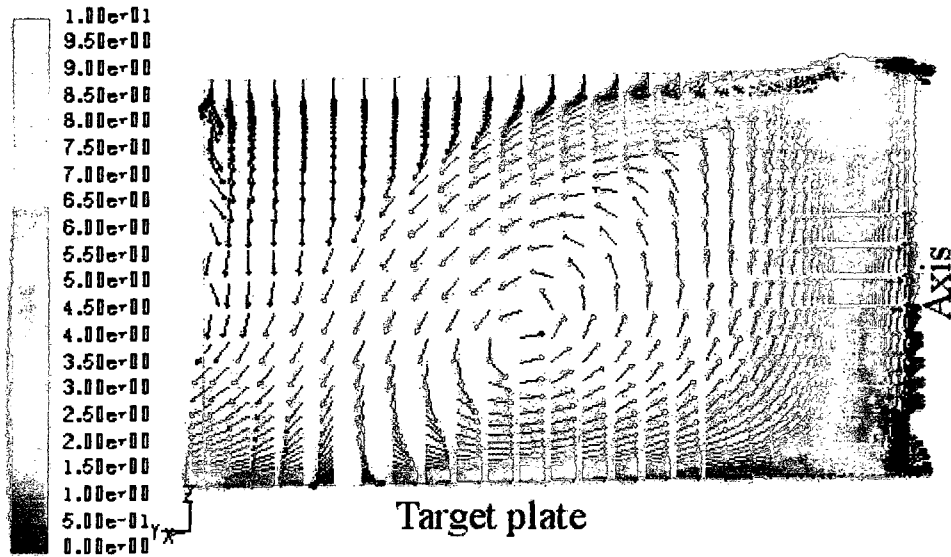


Figure 5.15 Meridian View of Air Velocity Vectors (paint flow rate = 150 cc/min, shaping air flow rate = 250 cc/min)

Figure 5.16 shows a meridian view of the air velocity magnitude contours at the baseline conditions. The higher velocity zone and the relatively lower velocity zone at the centre of this figure represent the turbine-bearing air inlet region and the circulation region, respectively. This figure also shows that the velocity at the upper part of the boundary of the domain is very low, essentially undisturbed by the spray. The electric field, the downdraft and the shaping air orientation and velocity combine to confine the spray. The velocity in the region where the mixed turbine-bearing air and shaping air stream strike the plate is also very low.

Figure 5.17 shows the meridian view of the static pressure contours at the baseline conditions. The actual pressure ranges from -1195 Pa to 251 Pa. The high speed stream caused by the turbine-bearing air flow creates a minimum pressure zone next to it. A low pressure zone forms around the axis of the domain. The circular low pressure zone at the centre of this figure corresponds to the circulation zone seen in Figure 5.15.

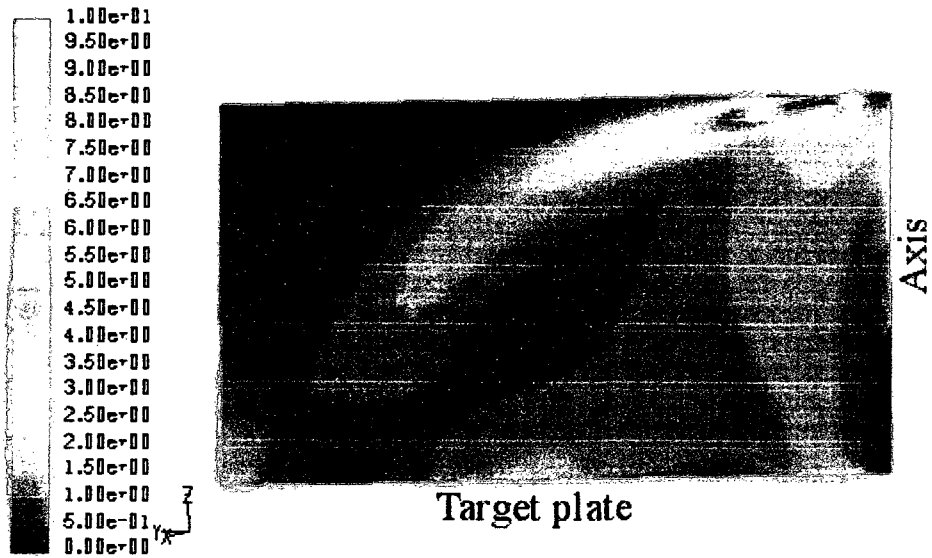


Figure 5.16 Meridian View of Air Velocity Magnitude Contours (paint flow rate = 150 cc/min, shaping air flow rate = 250 cc/min)

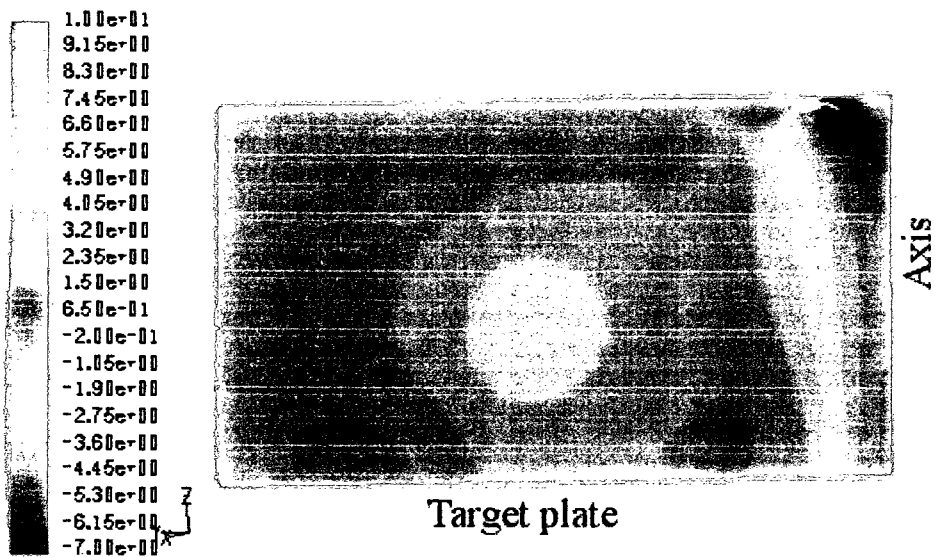


Figure 5.17 Meridian View of Static Pressure Contours (paint flow rate = 150 cc/min, shaping air flow rate = 250 cc/min)

Turbulent kinetic energy distribution is shown in Figure 5.18. The actual turbulent kinetic energy value ranges from $5e^{-6} \text{ K}\cdot\text{m}^2/\text{s}^2$ to $779.2 \text{ K}\cdot\text{m}^2/\text{s}^2$. The higher turbulent kinetic energy zone, in the region of the turbine-bearing air stream, characterizes the stronger turbulent zone. The strong turbulence in this region near the bell cup enhances the paint and air mixing and promotes the atomization process.

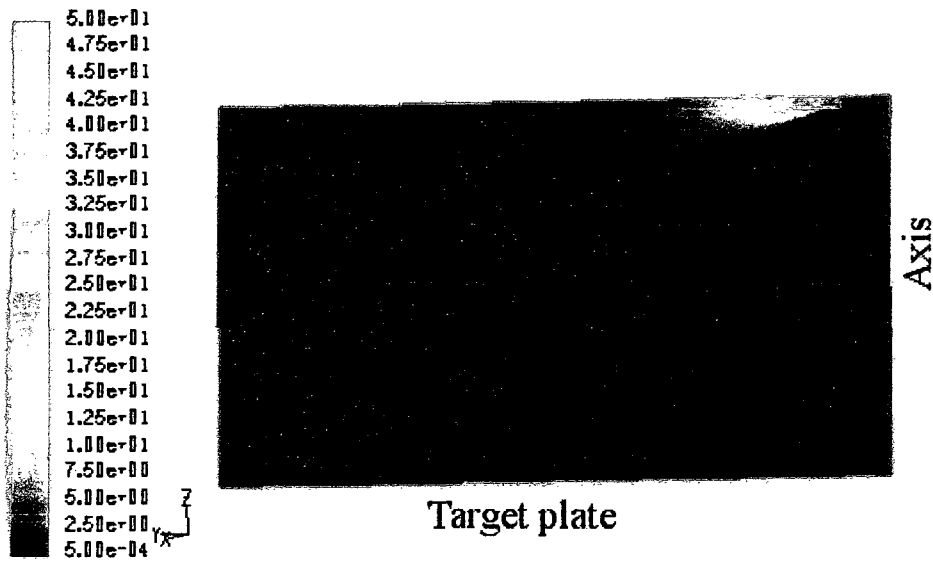


Figure 5.18 Meridian View of Turbulent Kinetic Energy Contours (paint flow rate = 150 cc/min, shaping air flow rate = 250 cc/min)

Figure 5.19 shows the turbulent dissipation rate contours. The actual range of the turbulent dissipation rate is from $1.4e^{-6} \text{ m}^2/\text{s}^3$ to $4.3e^7 \text{ m}^2/\text{s}^3$. It can be seen that the turbulent dissipation rate is higher in the turbine-bearing air region and, like the turbulent kinetic energy, uniformly low over the rest of the spray region.

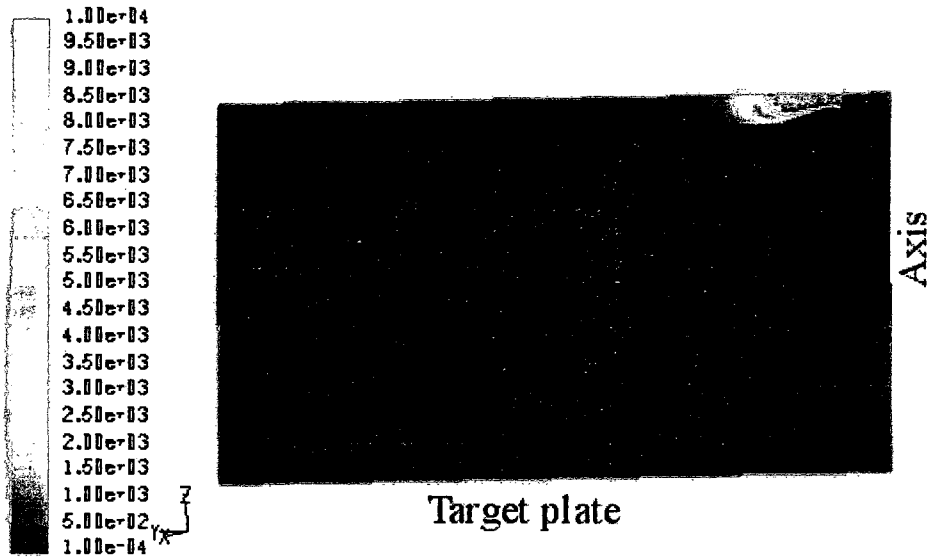


Figure 5.19 Meridian View of Turbulent Dissipation Rate Contours (paint flow rate = 150 cc/min, shaping air flow rate = 250 cc/min)

Figure 5.20 shows the static pressure distribution on the target plate. The pressure is very low at the centre of the target plate. An annular high pressure zone is formed in the area where the air velocity decreases sharply. Comparing Figure 5.14 and Figure 5.20, it is seen that the injection of the paint droplets has a dramatic effect on the plate pressure. The pressure, which decreases with radius for the pure air spray, now has its lowest value at the plate centre, increases out to about one-third of the plate radius, then decreases slightly before increasing again to reach its maximum value at approximately 70% of the distance to the edge of the plate. This variation is caused by the rotating vortex seen above the plate in Figure 5.15.

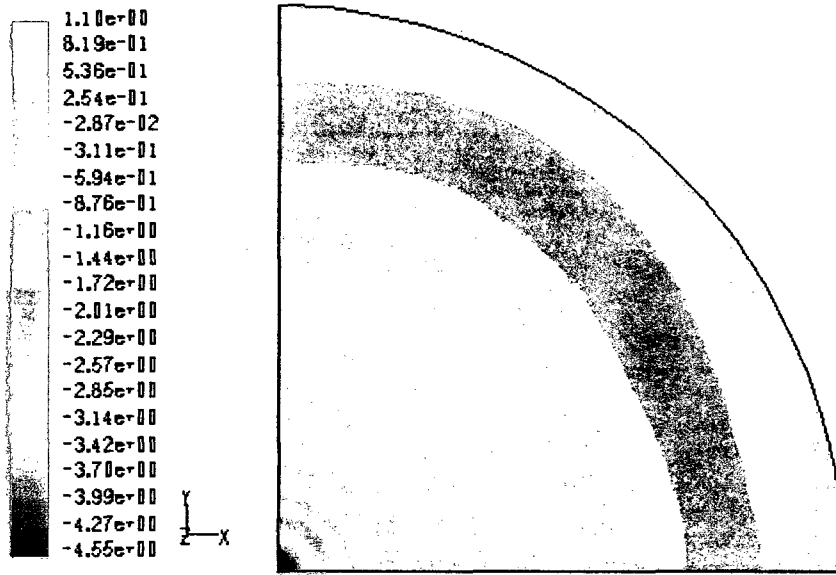


Figure 5.20 Static Pressure Contours on the Target Plate (paint flow rate = 150 cc/min, shaping air flow rate = 250 cc/min)

Figure 5.21 shows a closeup view of static pressure near the centre of the target plate. These pressure contours show fairly good uniformity along the circumferential direction and an increase in pressure in the radial direction for this section of the plate.

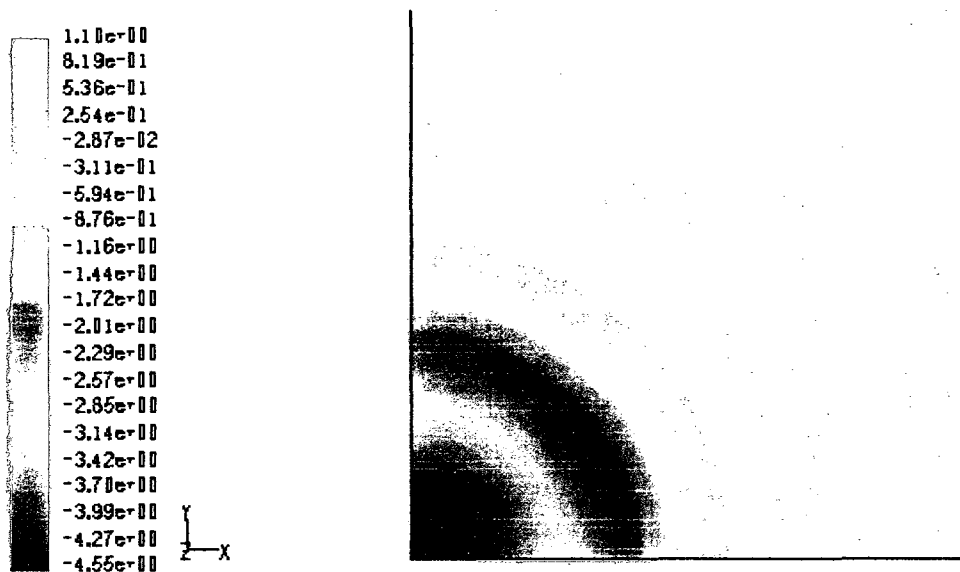


Figure 5.21 Static Pressure Contours at the Centre of the Target Plate (paint flow rate = 150 cc/min, shaping air flow rate = 250 cc/min)

Figure 5.22 and Figure 5.23 show the complete and centre closeup view of the turbulent kinetic energy on the target plate, respectively. The contour shapes illustrate that the turbulent kinetic energy is more circumferentially uniform near the centre of the plate. These figures also show that the plate turbulent kinetic energy, which is very low across the entire plate, attains its maximum value close to the plate centre.

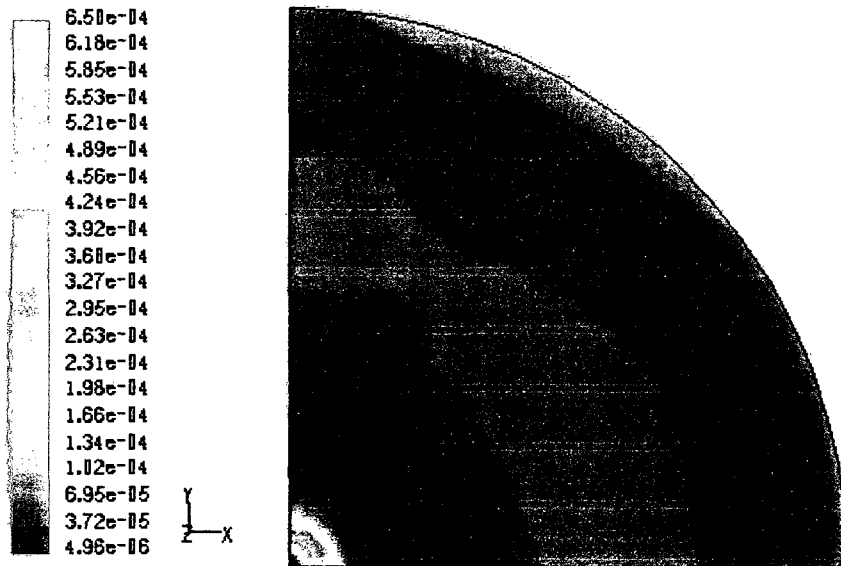


Figure 5.22 Turbulent Kinetic Energy Contours on the Target Plate (paint flow rate = 150 cc/min, shaping air flow rate = 250 cc/min)

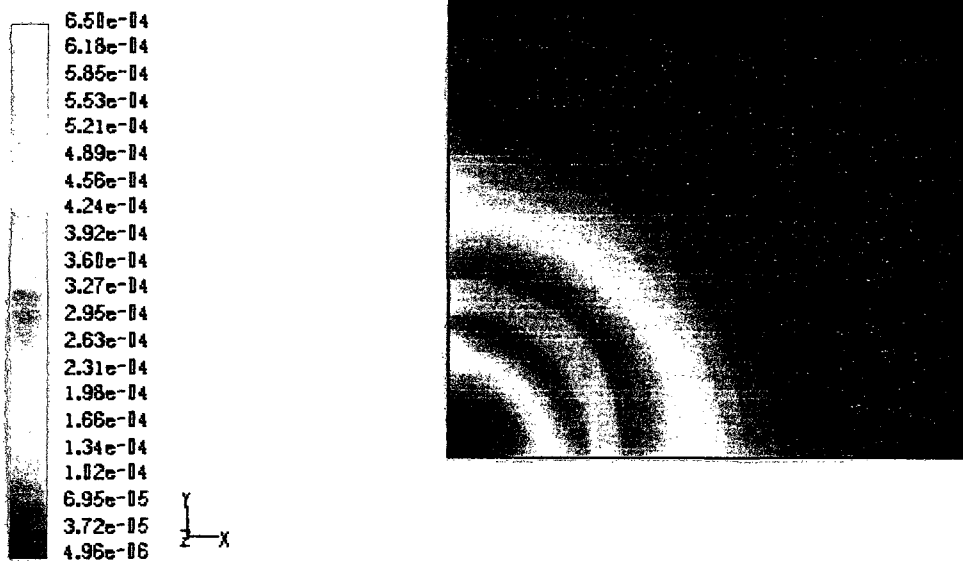


Figure 5.23 Turbulent Kinetic Energy Contours at the Centre of the Target Plate (paint flow rate = 150 cc/min, shaping air flow rate = 250 cc/min)

Figure 5.24 and Figure 5.25 show the complete and centre closeup view of the turbulent dissipation rate contours on the target plate, respectively. Like pressure and turbulent kinetic energy, the turbulent dissipation rate contours are more circumferentially uniform at the centre of the plate.

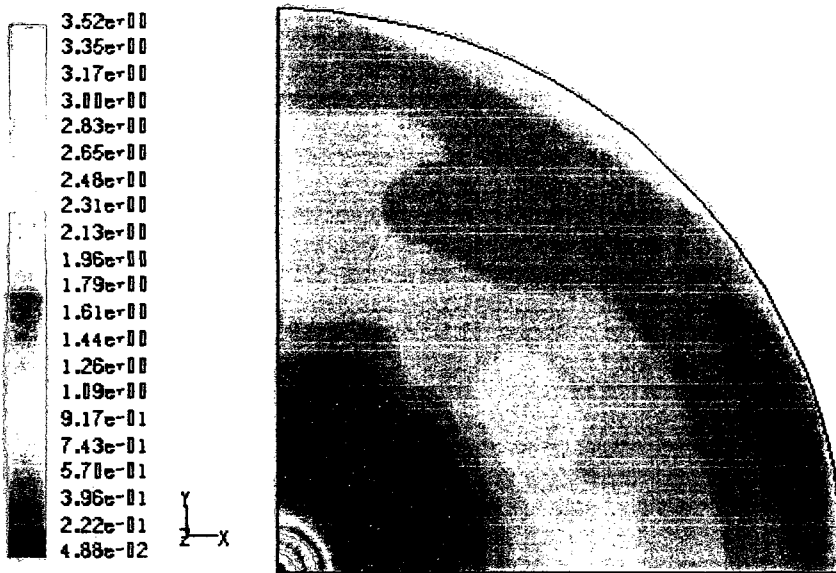


Figure 5.24 Turbulent Dissipation Rate Contours on the Target Plate (paint flow rate = 150 cc/min, shaping air flow rate = 250 cc/min)

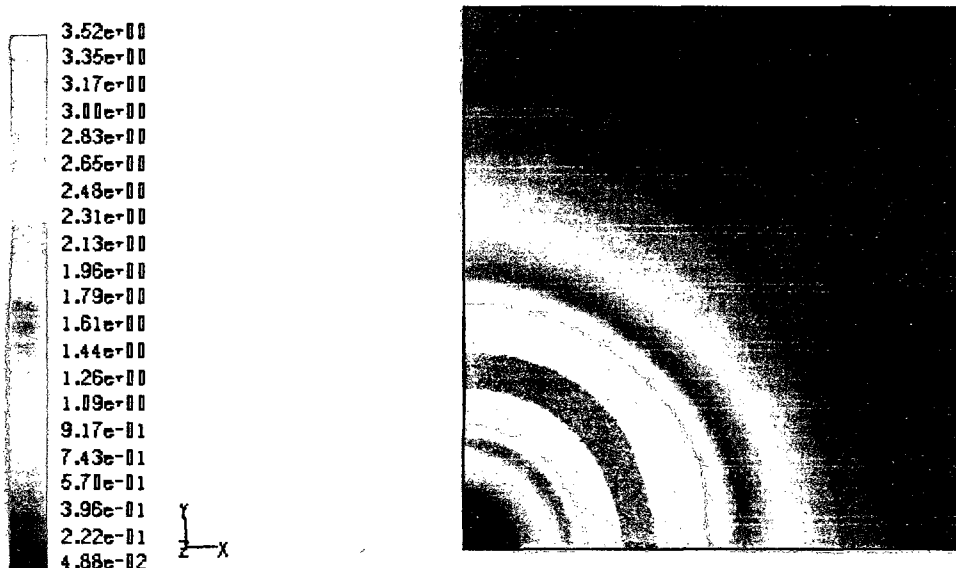


Figure 5.25 Turbulent Dissipation Rate Contours at the Centre of the Target Plate (paint flow rate = 150 cc/min, shaping air flow rate = 250 cc/min)

Figure 5.26 illustrates the droplet distribution at baseline conditions. This figure shows that the droplets at the centre of the spray cone experience longer residence time. Examining Figure 5.15 and Figure 5.26, it can be seen that the droplets fly along the edge of the spray cone soon after the injection. Some of them deposit when they hit the target plate, some of them fly out of the domain, and the majority of them are drawn back towards the centre of the spray cone and circulate with the air vortex. Most of these circulating droplets eventually deposit near the centre of the target plate.

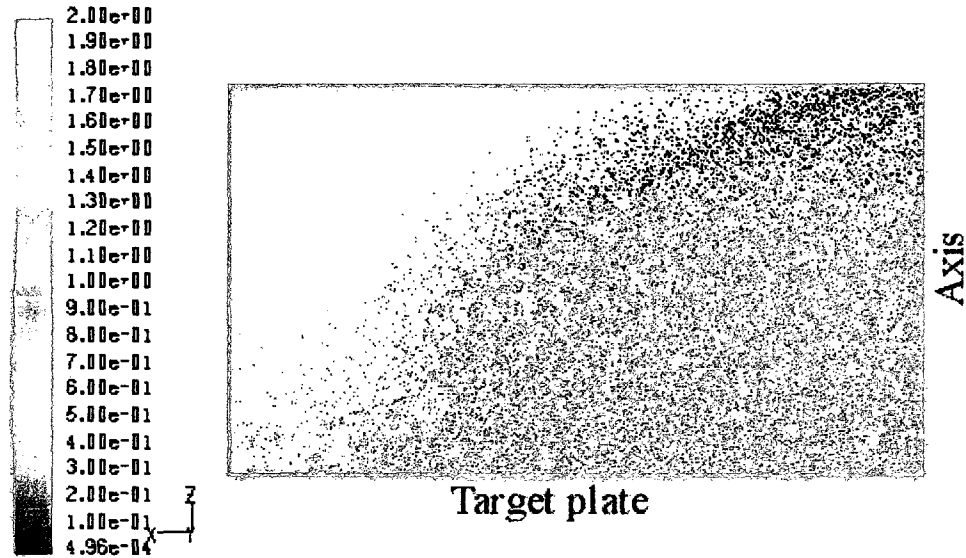


Figure 5.26 Droplet Trace Coloured by Droplet Residence Time (paint flow rate = 150 cc/min, shaping air flow rate = 250 cc/min)

5.8.3 Effect of Voltage

Figure 5.27 and Figure 5.28 show the meridian view of air velocity magnitude contours for sprays with 50 kV and 90 kV electric charge respectively. All other parameters are kept at their baseline values. Comparing Figure 5.16, Figure 5.27 and Figure 5.28, it can be seen that there is no significant difference in the air velocity field among these three conditions.

Static pressure distribution on the target plate for 50 kV and 90 kV are plotted in Figure 5.29 and Figure 5.30, respectively. Comparing Figure 5.20, Figure 5.29 and Figure 5.30, we observe that the pressure contour shapes for 70 kV and 90 kV are very close, which agrees well with the observation from experiments reported by Im et al. (2001).

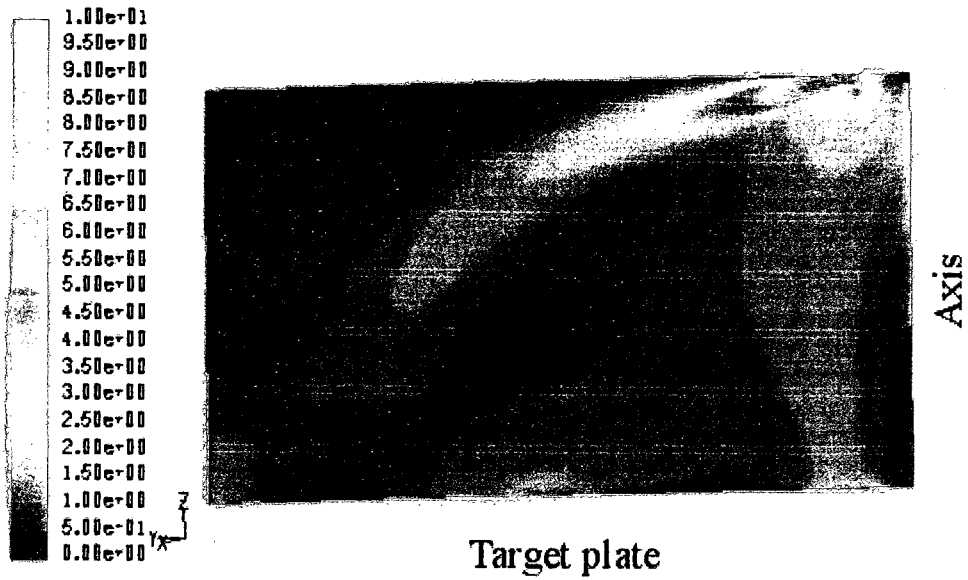


Figure 5.27 Meridian View of Air Velocity Magnitude Contours at 50 kV



Figure 5.28 Meridian View of Air Velocity Magnitude Contours at 90 kV

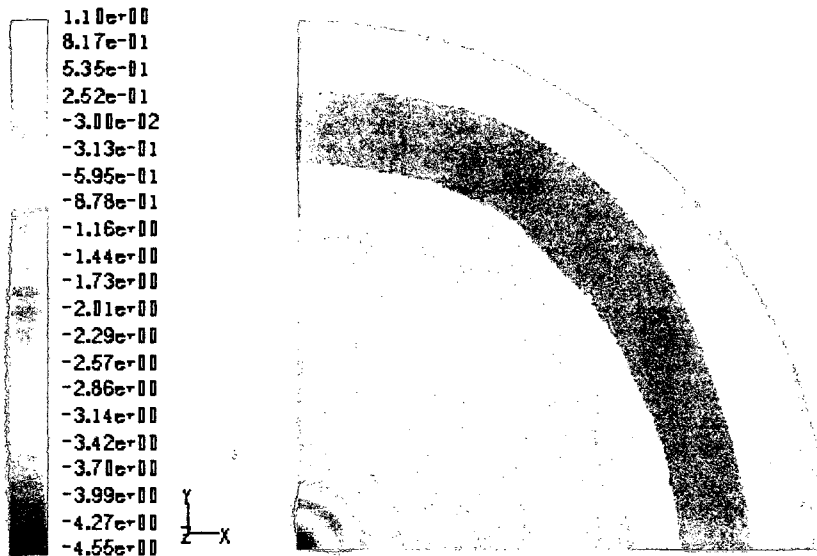


Figure 5.29 Static Pressure Contours on the Target Plate at 50 kV

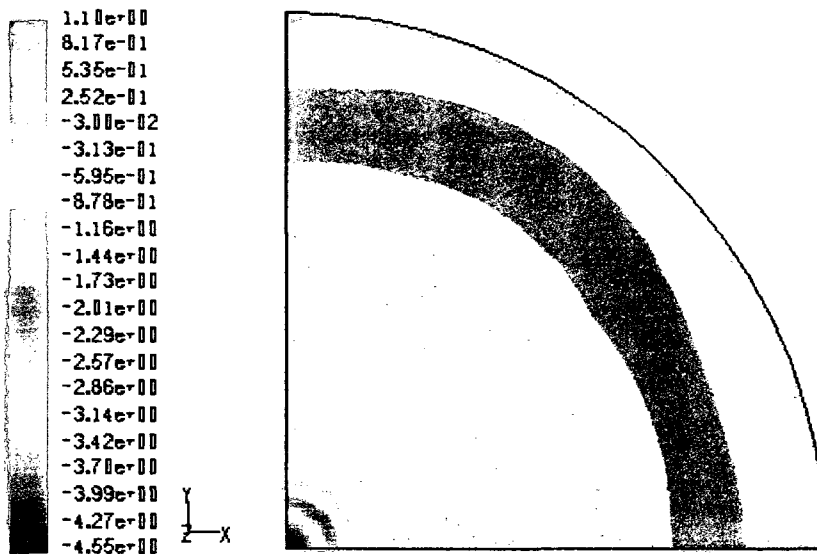


Figure 5.30 Static Pressure Contours on the Target Plate at 90 kV

Droplet tracks for sprays with 50 kV and 90 kV are plotted in Figure 5.31 and Figure 5.32, respectively. Compared with Figure 5.26, it can be seen that there is no significant difference between the 70 kV and 90 kV cases, while the spray is more confined in the 70 kV case than in the 50 kV case.

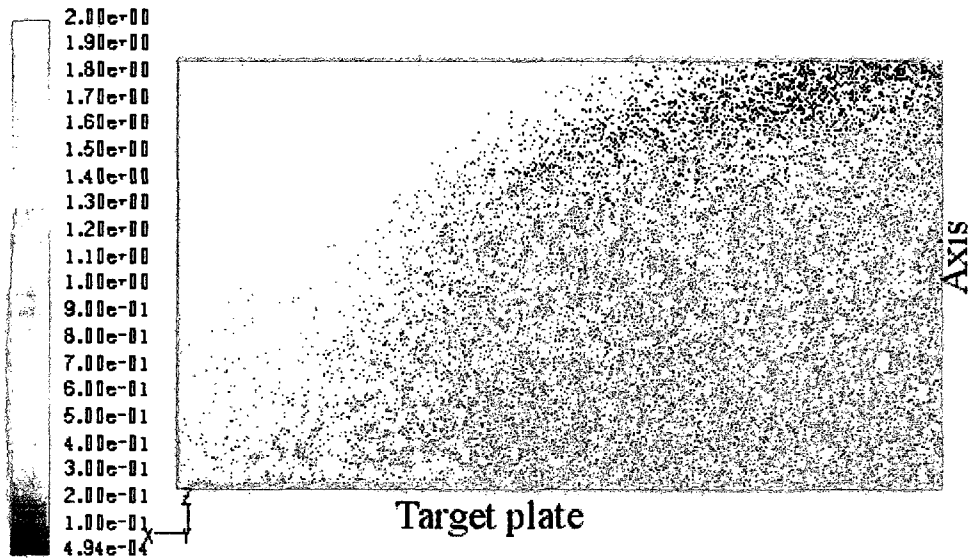


Figure 5.31 Droplet Trace Coloured by Droplet Residence Time at 50 kV

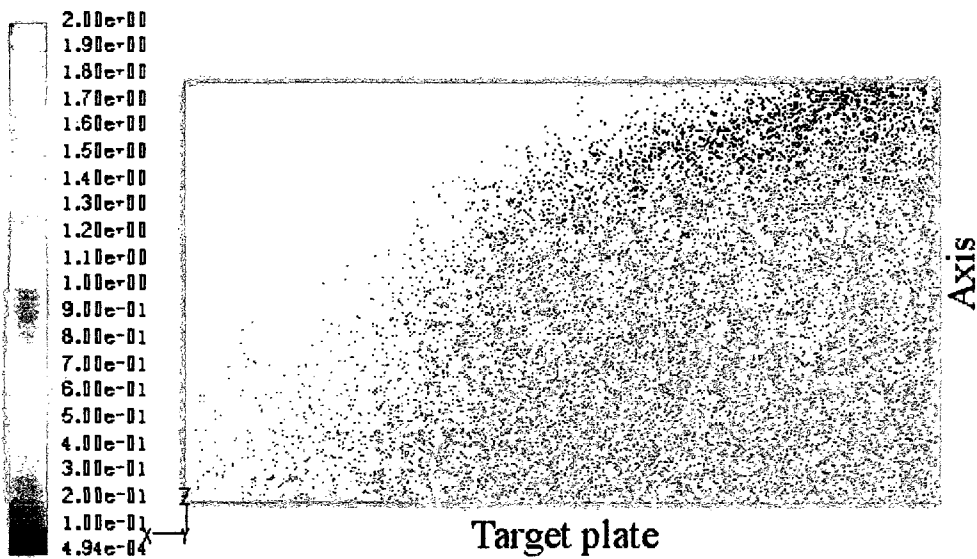


Figure 5.32 Droplet Trace Coloured by Droplet Residence Time at 90 kV

5.8.4 Effect of Droplet Diameter

As mentioned previously, there is no definitive formula to determine the size of the droplets resulting from the atomization in the bell cup. Based on our earlier discussion, we have taken the initial droplet size at the inlet of the spray region to be the same as the paint film thickness at the outer edge of the bell cup. As seen in Figure 4.8

and Figure 4.9, we use droplet sizes in the range of 6 to 12 microns, depending upon operating conditions. Other researchers, such as Domnick and Thieme (2004), estimated droplets sizes in the range of 5 to 15 microns, while Im (1999) and Huang et al. (2000) used a droplet diameter of 25 microns based on their experimental data. The average droplet size that Bauckage et al. (1994 & 1995) calculated based on their experimental data was about 30 microns. On the other hand, empirical formulae suggested by Domnick and Thieme (2004) estimate droplet sizes that are an order of magnitude smaller than those used here. To test the effect of initial droplet size, spray simulations were conducted for initial droplet diameters of one-fifth and one-tenth the paint film thickness at the bell edge.

Figure 5.33 to Figure 5.37 show contours and droplet trace obtained by using one-tenth of the film thickness at the bell edge as the initial droplet diameter, with all other parameters set at the baseline values. Compared to the baseline condition, the contours of velocity magnitude, turbulent kinetic energy, turbulent dissipation rate and static pressure (see Figure 5.17 and Figure 5.33) on the meridian plane do not change. The plate pressure is unchanged (see Figure 5.20 and Figure 5.34), while the turbulent kinetic energy and turbulent dissipation rate on the plate differ only slightly (compare Figure 5.22 with Figure 5.35, and Figure 5.24 with Figure 5.36). The droplets residence time is somewhat larger in this case, as seen from Figure 5.26 and Figure 5.37. This indicates that the smaller droplets tend to circulate with the circulating air because their lower momentum is more easily overcome by the air flow, while the larger droplets tend to overcome the air flow and fly out of the spray cone. Im (1999) and Im et al. (2001) also reached this conclusion based on their measurements. Overall, it appears that the initial droplet diameter has very little effect on the spray flow field. Thus, all subsequent results correspond to simulations for which the droplet size is taken to be the same as the paint film thickness at the edge of the bell cup.

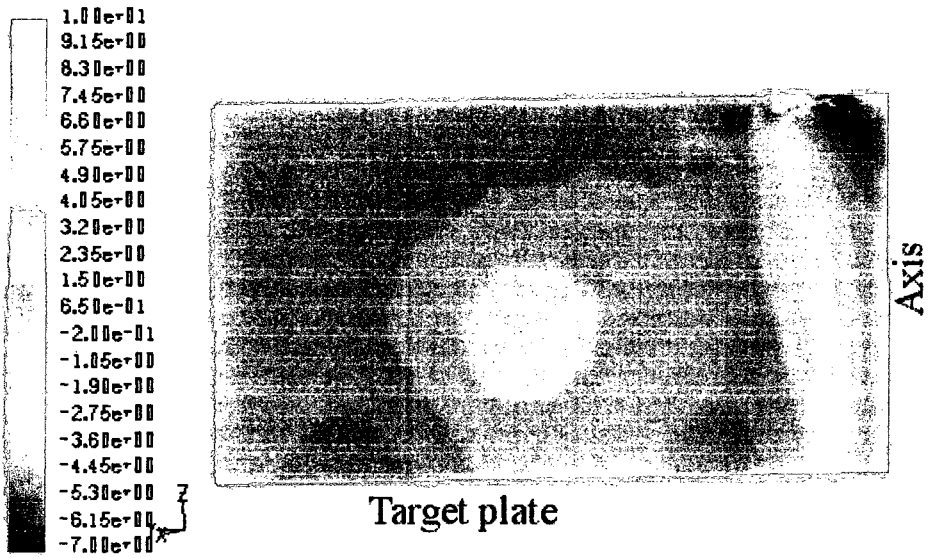


Figure 5.33 Meridian View of Static Pressure Contours using One-tenth of Film Thickness at the Bell Edge as Initial Droplet Diameter

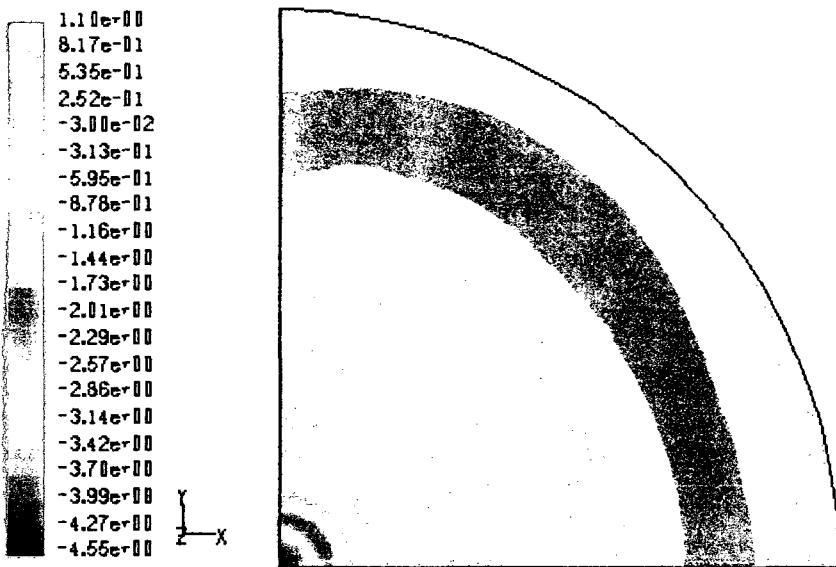


Figure 5.34 Static Pressure Contours on the Target Plate using One-tenth of Film Thickness at the Bell Edge as Initial Droplet Diameter

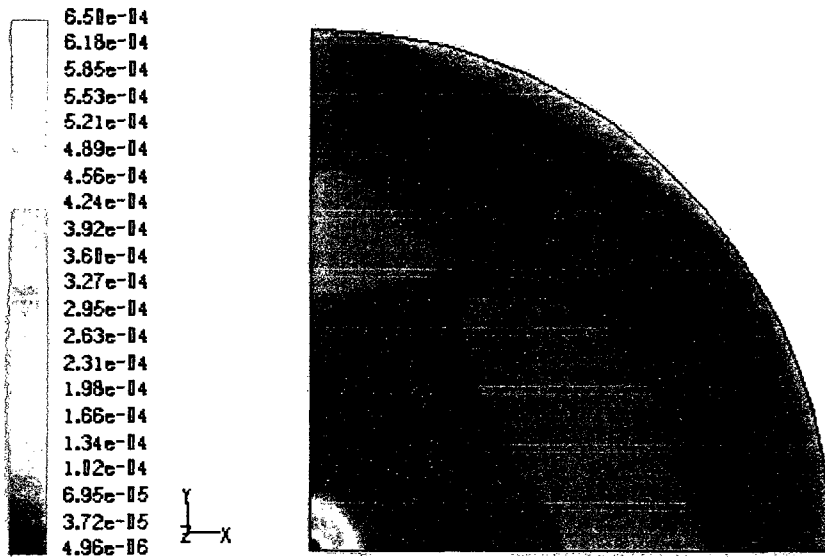


Figure 5.35 Turbulent Kinetic Energy Contours on the Target Plate using One-tenth of Film Thickness at the Bell Edge as Initial Droplet Diameter

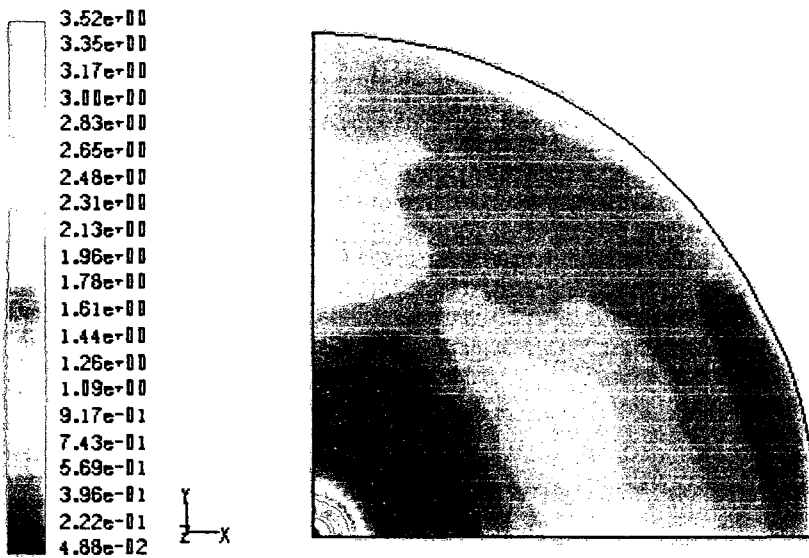


Figure 5.36 Turbulent Dissipation Rate Contours on the Target Plate using One-tenth of Film Thickness at the Bell Edge as Initial Droplet Diameter

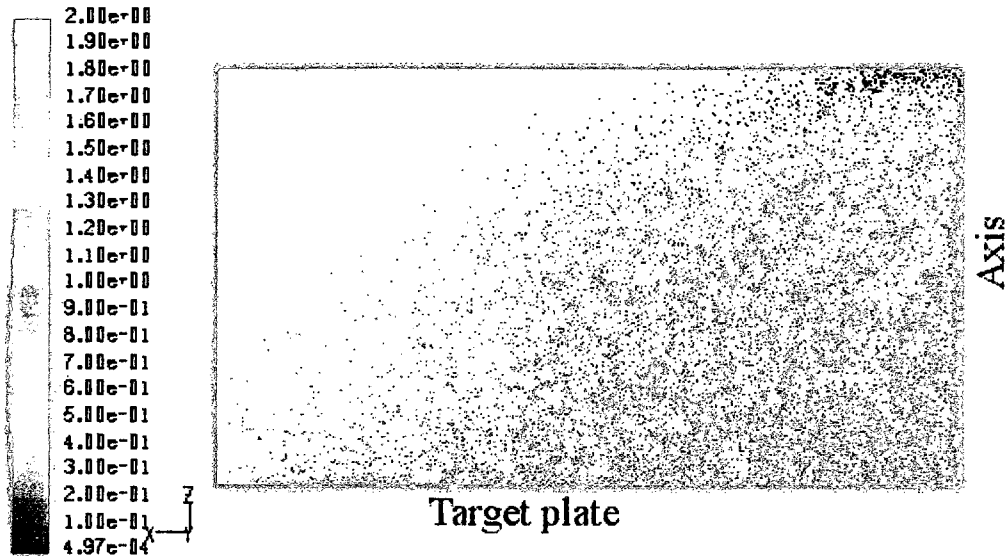


Figure 5.37 Droplet Trace Coloured by Droplet Residence Time using One-tenth of Film Thickness at the Bell Edge as Initial Droplet Diameter

5.8.5 Effect of Bell Rotational Speed

Figure 5.38 to Figure 5.42 show the contours at bell rotational speed of 42000 rpm. Compared with the baseline condition (38,000 rpm), the velocity vectors close to the turbine-bearing air inlet are more horizontal (see Figure 5.15 and Figure 5.42), which suggest higher circumferential velocity caused by the higher bell rotational speed. Figure 5.39 shows a corresponding change in the pressure field, particularly near this air inlet. Although there is no noticeable difference for the static pressure on the target plate (see Figure 5.21 and Figure 5.40), the turbulent kinetic energy and dissipation rate on the target plate show significant difference (compare Figure 5.23 with Figure 5.41, and Figure 5.25 with Figure 5.42).

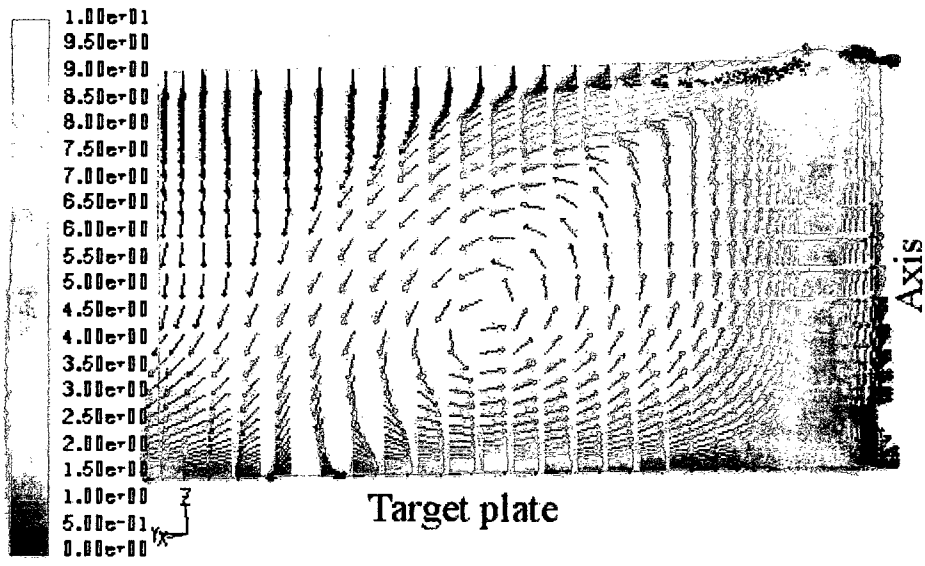


Figure 5.38 Meridian View of Velocity Vectors (bell rotational speed = 42000 rpm)

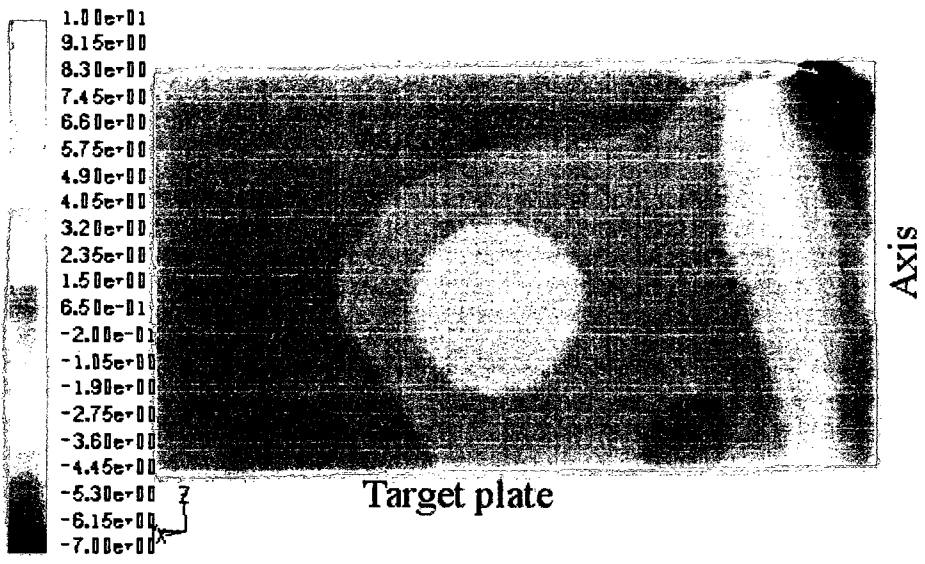


Figure 5.39 Meridian View of Static Pressure (bell rotational speed = 42000 rpm)

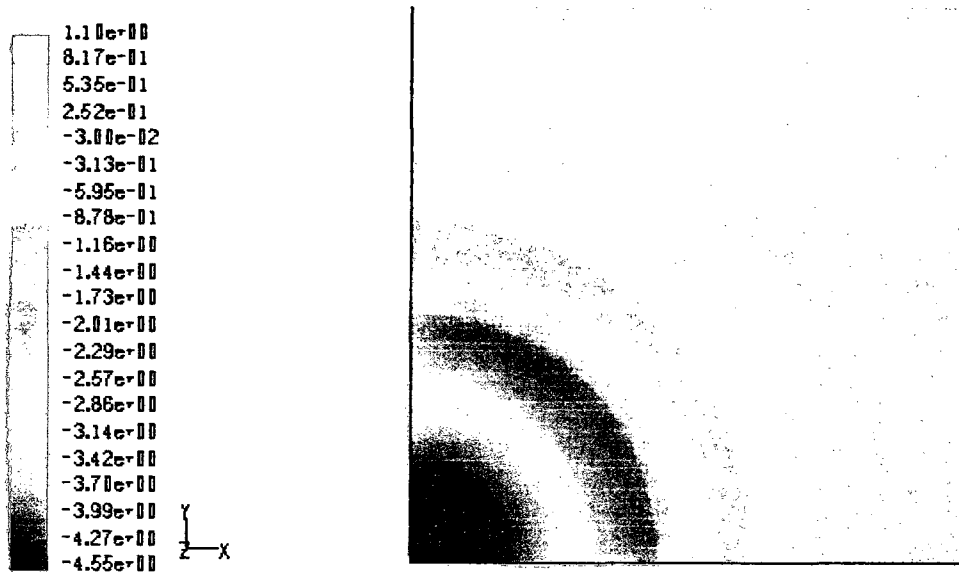


Figure 5.40 Static Pressure Contours at the Centre of the Target Plate (bell rotational speed = 42000 rpm)

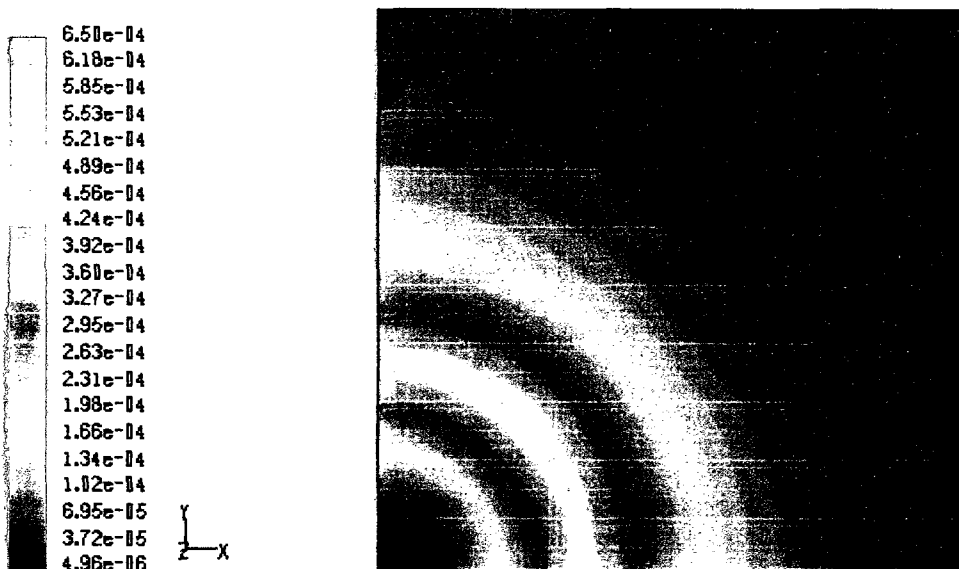


Figure 5.41 Turbulent Kinetic Energy Contours at the Centre of the Target Plate (bell rotational speed = 42000 rpm)

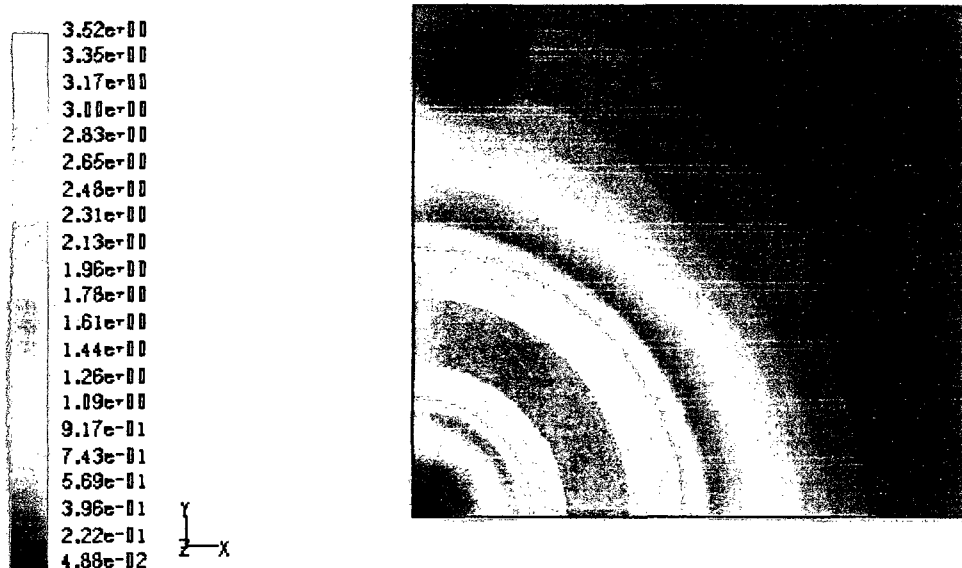


Figure 5.42 Turbulent Dissipation Rate Contours at the Centre of the Target Plate (bell rotational speed = 42000 rpm)

5.8.6 Effect of Paint Flow Rate

Figure 5.43 to Figure 5.46 show contours and droplet trace at paint flow rate of 200 cc/min, with shaping air flow rate the same as at the baseline condition, i.e., 250 cc/min. Compared with the baseline case, there are some minor differences in the contours shape of pressure, both near the bell cup and near the target plate (see Figure 5.17 and Figure 5.43, Figure 5.21 and Figure 5.44). The turbulent kinetic energy and turbulent dissipation rate on the central portion of the plate are noticeably different (compare Figure 5.45 with Figure 5.23, and Figure 5.46 with Figure 5.25). The droplets residence time (Figure 5.47) at the centre of the spray cone in this case is larger than in the baseline case (Figure 5.26), which indicates more droplets deposit at the centre of plate and the paint film is expected to be thicker at the centre.

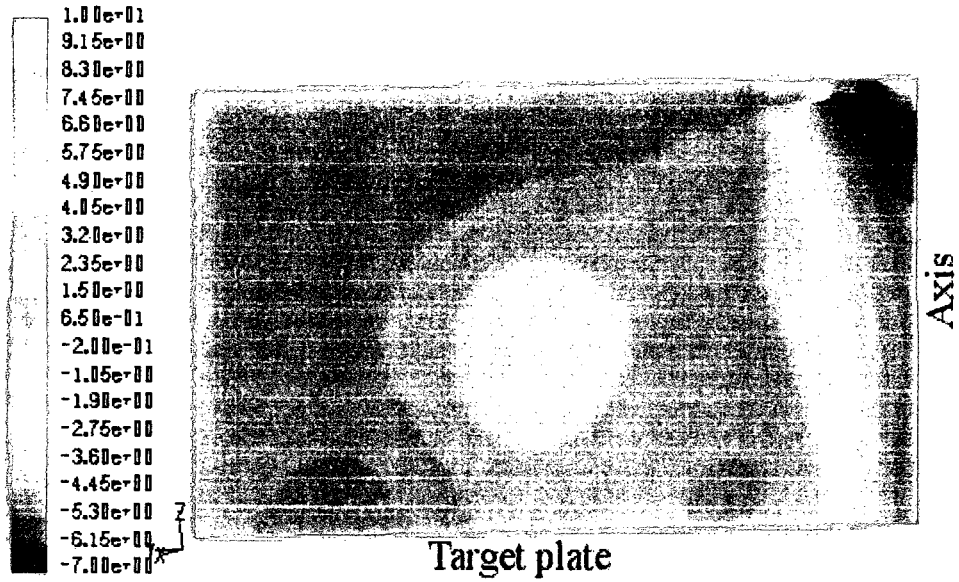


Figure 5.43 Meridian View of Static Pressure Contours (paint flow rate = 200 cc/min, shaping air flow rate = 250 cc/min)

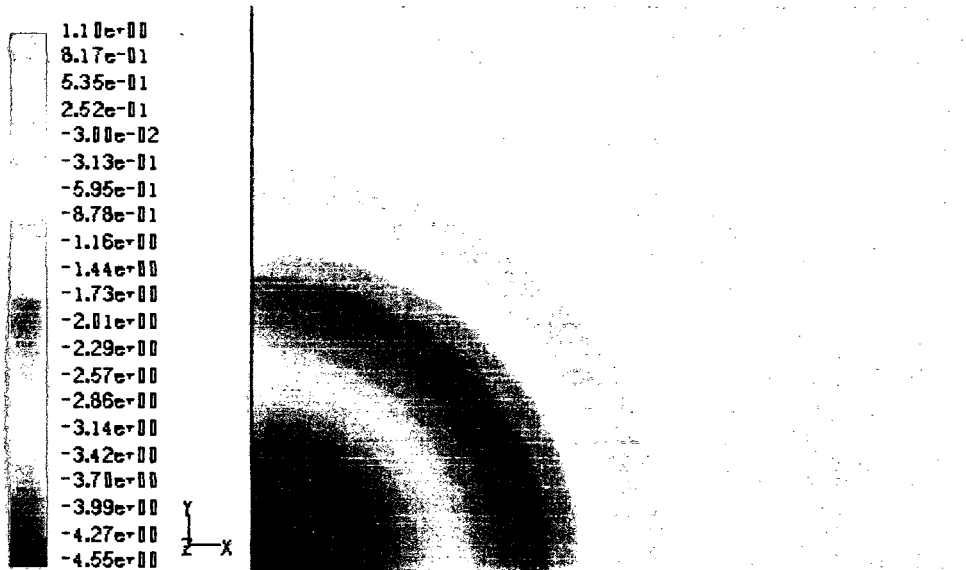


Figure 5.44 Static Pressure Contours at the Centre of the Target Plate (paint flow rate = 200 cc/min, shaping air flow rate = 250 cc/min)

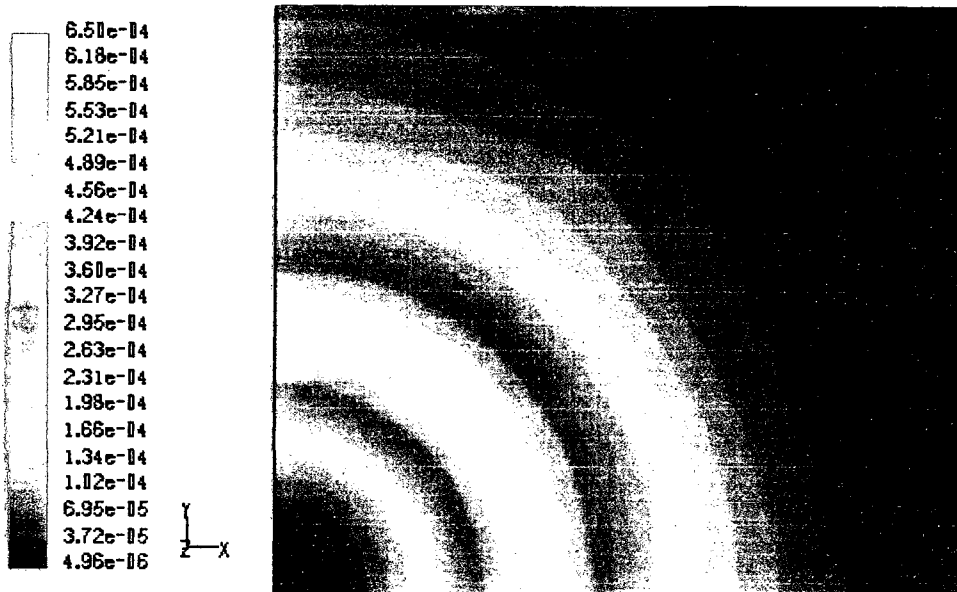


Figure 5.45 Turbulent Kinetic Energy Contours at the Centre of the Target Plate (paint flow rate = 200 cc/min, shaping air flow rate = 250 cc/min)

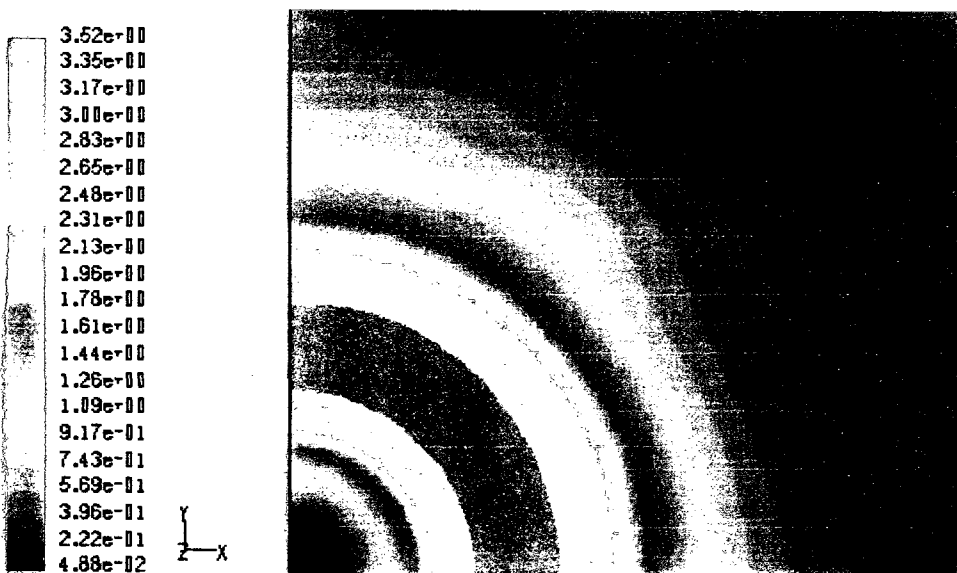


Figure 5.46 Turbulent Dissipation Rate Contours at the Centre of the Target Plate (paint flow rate = 200 cc/min, shaping air flow rate = 250 cc/min)

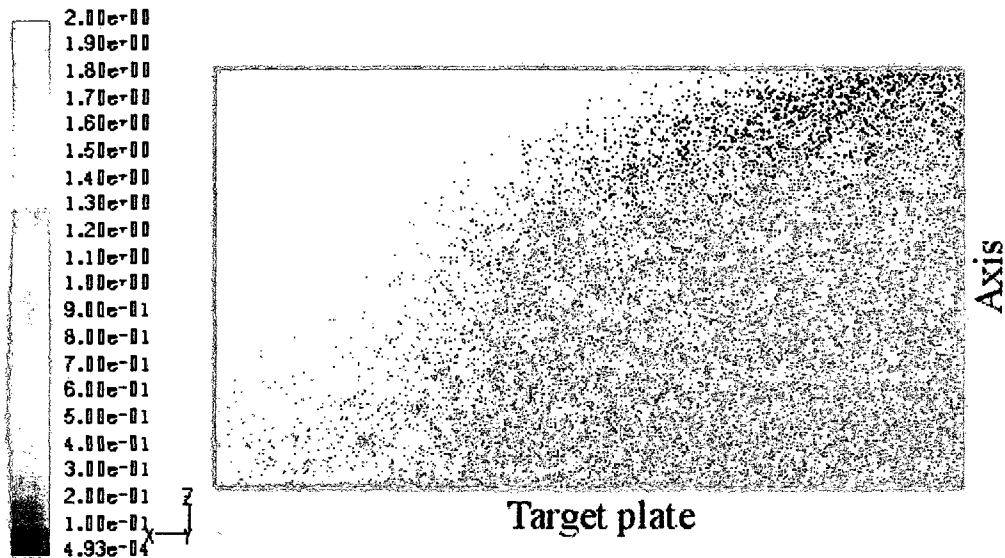


Figure 5.47 Droplet Trace Coloured by Droplet Residence Time (paint flow rate = 200 cc/min, shaping air flow rate = 250 cc/min)

5.8.7 Effect of Shaping Air Flow Rate

Figure 5.48 to Figure 5.51 show the contours at paint flow rate of 175 cc/min, with shaping air flow rate of 150 cc/min. Figure 5.52 to Figure 5.55 show these contours at the same paint flow rate, but with a shaping air flow rate of 250 cc/min. Comparing these two cases, the most significant differences are seen in the contours for pressure (Figure 5.48 and Figure 5.52, Figure 5.49 and Figure 5.53), turbulent kinetic energy (Figure 5.50 and Figure 5.54) and turbulent dissipation rate (Figure 5.51 and Figure 5.55).

Significant differences cannot be observed in the droplets trace plots for these flow rates, although the higher shaping air flow rate does tend to confine the spray more than the lower flow rates.

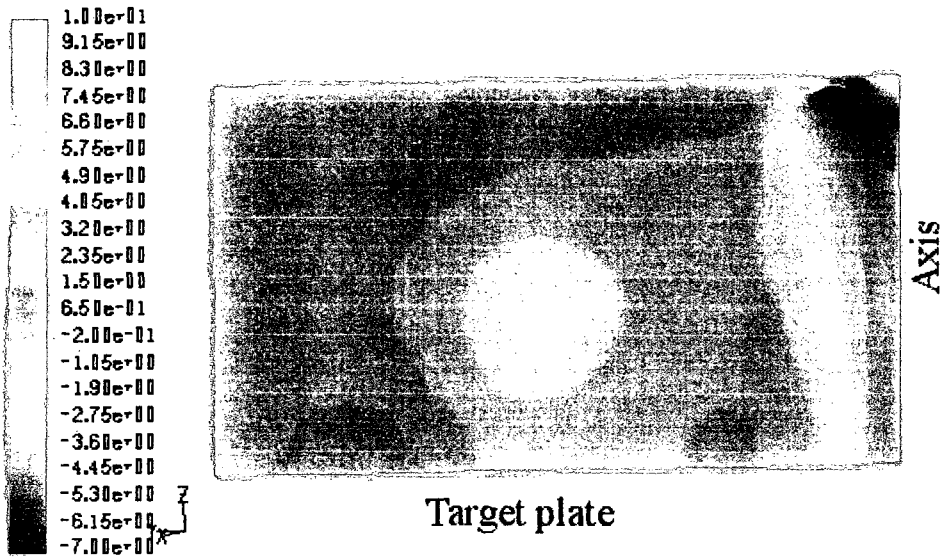


Figure 5.48 Meridian View of Static Pressure Contours (paint flow rate = 175 cc/min, shaping air flow rate = 150 cc/min)

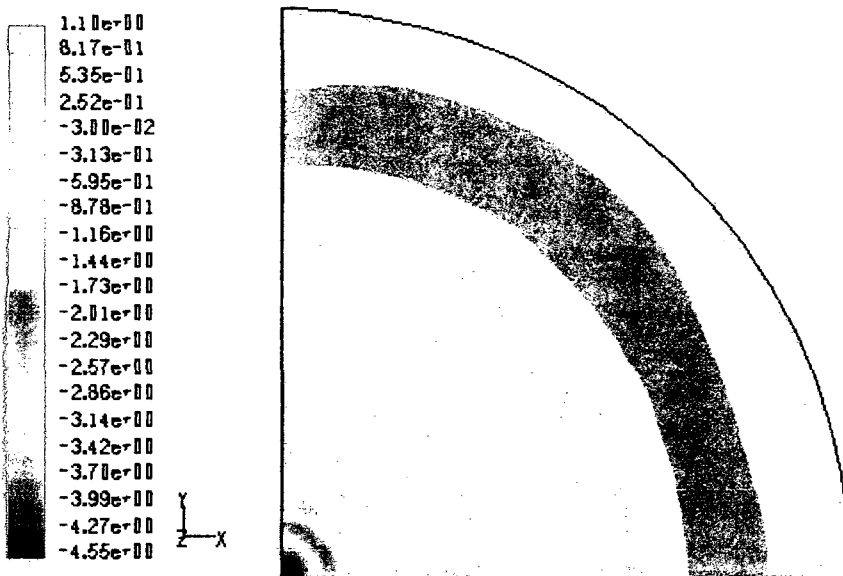


Figure 5.49 Static Pressure Contours on the Target Plate (paint flow rate = 175 cc/min, shaping air flow rate = 150 cc/min)

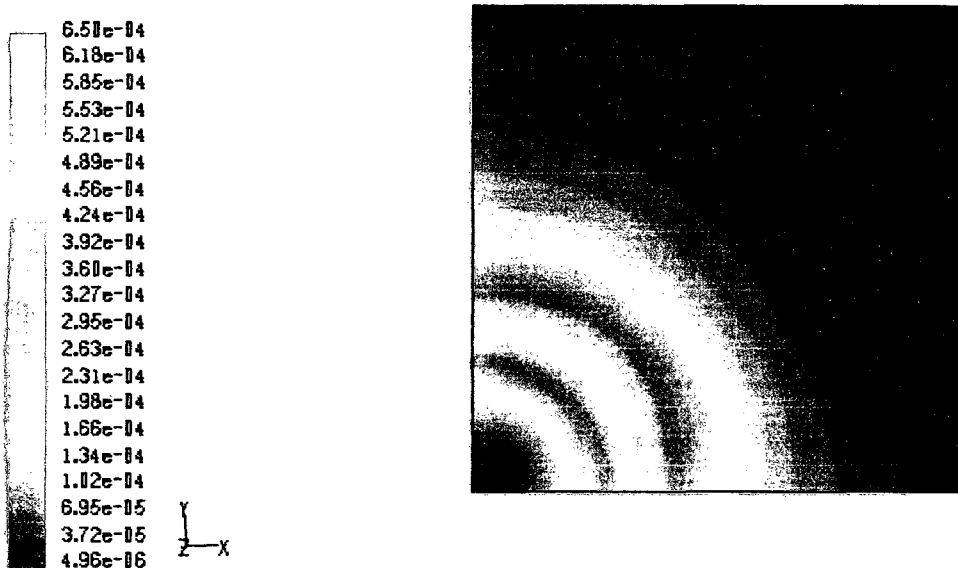


Figure 5.50 Turbulent Kinetic Energy Contours at the Centre of the Target Plate (paint flow rate = 175 cc/min, shaping air flow rate = 150 cc/min)

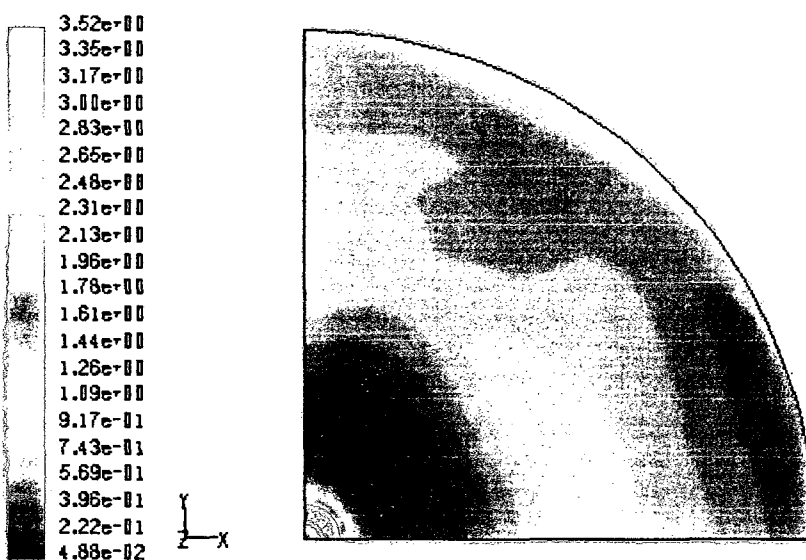


Figure 5.51 Turbulent Dissipation Rate Contours on the Target Plate (paint flow rate = 175 cc/min, shaping air flow rate = 150 cc/min)

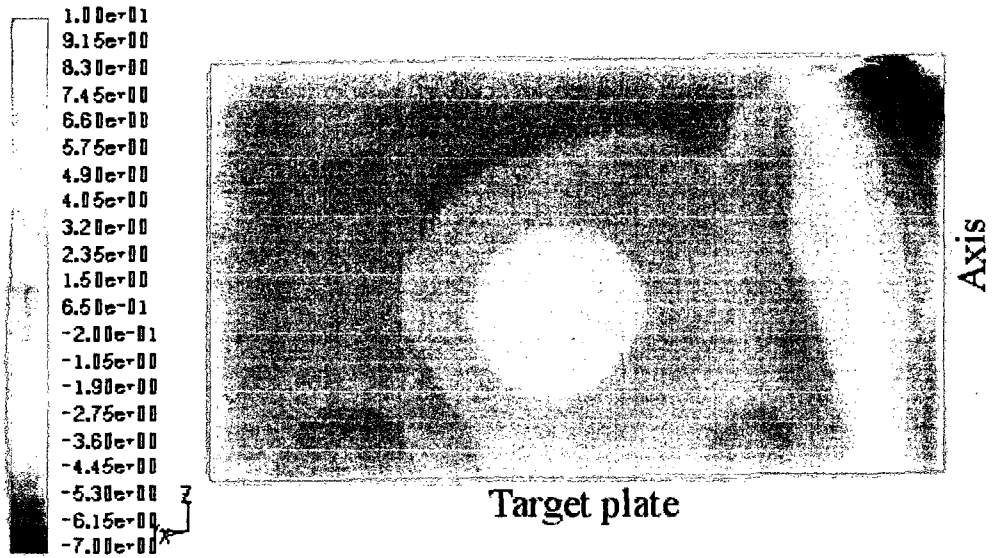


Figure 5.52 Meridian View of Static Pressure Contours (paint flow rate = 175 cc/min, shaping air flow rate = 250 cc/min)

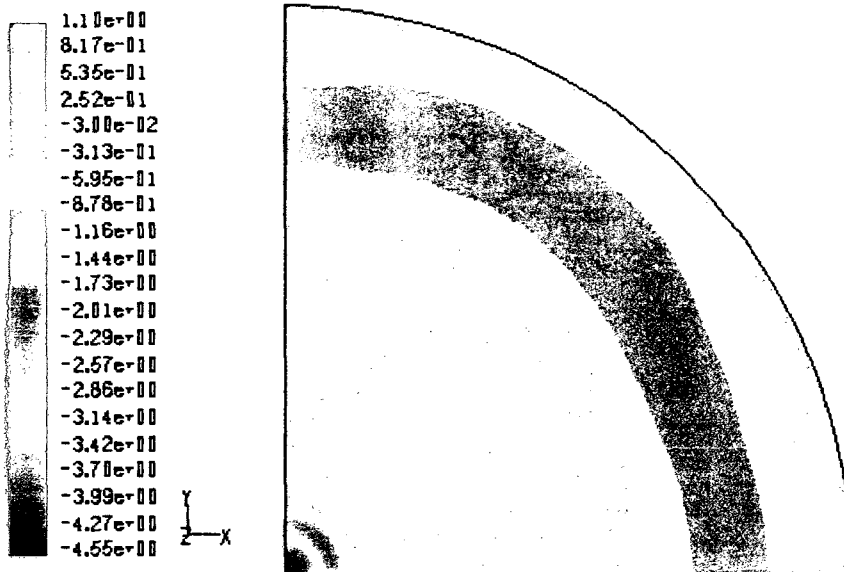


Figure 5.53 Static Pressure Contours on the Target Plate (paint flow rate = 175 cc/min, shaping air flow rate = 250 cc/min)

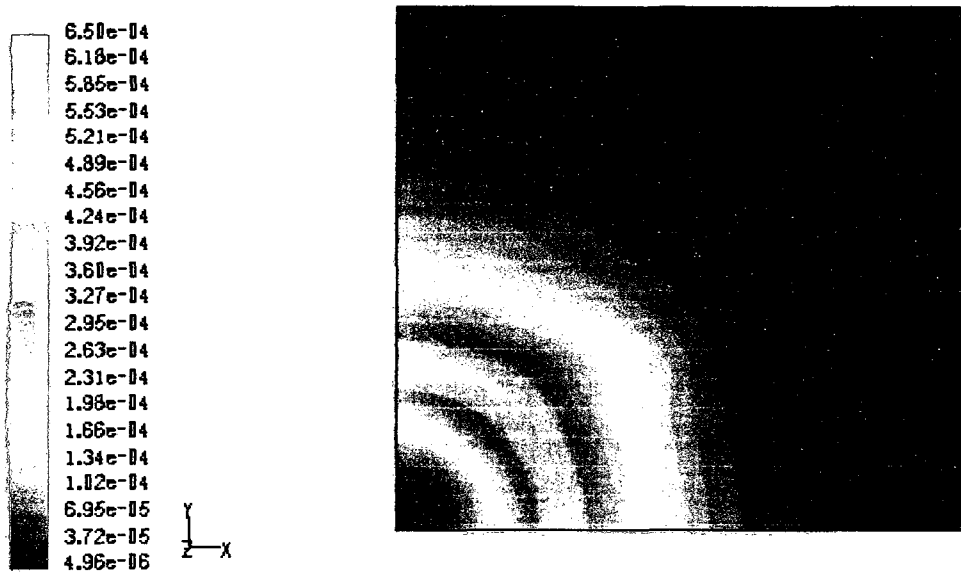


Figure 5.54 Turbulent Kinetic Energy Contours at the Centre of the Target Plate (paint flow rate = 175 cc/min, shaping air flow rate = 250 cc/min)

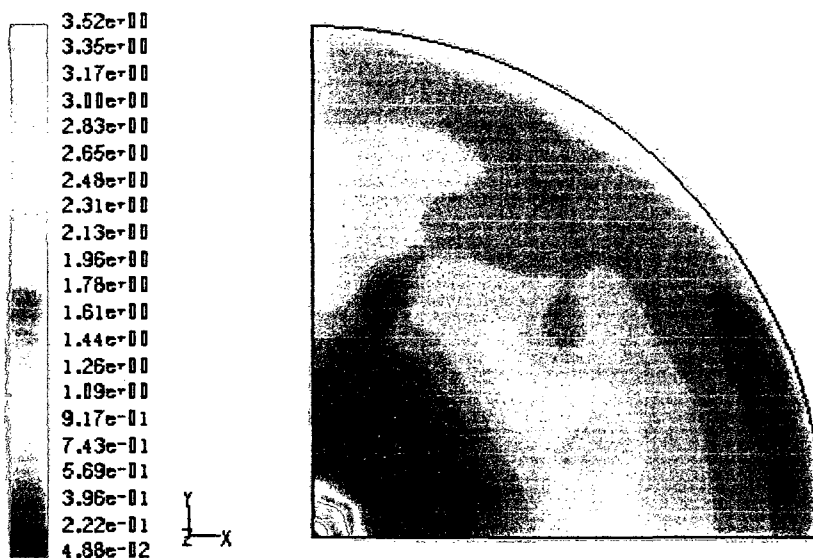


Figure 5.55 Turbulent Dissipation Rate Contours on the Target Plate (paint flow rate = 175 cc/min, shaping air flow rate = 250 cc/min)

5.8.8 Effect of Spray Angle

In previous sections we have examined the effects that the various flow parameters, which can be adjusted by the user, have on the spray. In an attempt to also see how the bell cup design can affect the spray, two additional simulations were performed. In one, the angle at which the paint droplets are injected into the domain has been decreased from 27.5° to 22.5°, in the other the spray angle was increased to 32.5°. All other parameters are kept at their baseline values. Figure 5.56 to Figure 5.59 show the contours at 22.5° spray angle. Compared with the baseline, the high pressure zone close to the turbine-bearing air inlet is smaller in this case (see Figure 5.17 and Figure 5.56). There is no significant difference for the static pressure on the target plate, as seen by comparison of Figure 5.20 and Figure 5.57. However, the turbulent kinetic energy (see Figure 5.23 and Figure 5.58) and the turbulent dissipation rate (see Figure 5.24 and Figure 5.59) on the target plate are quite different.

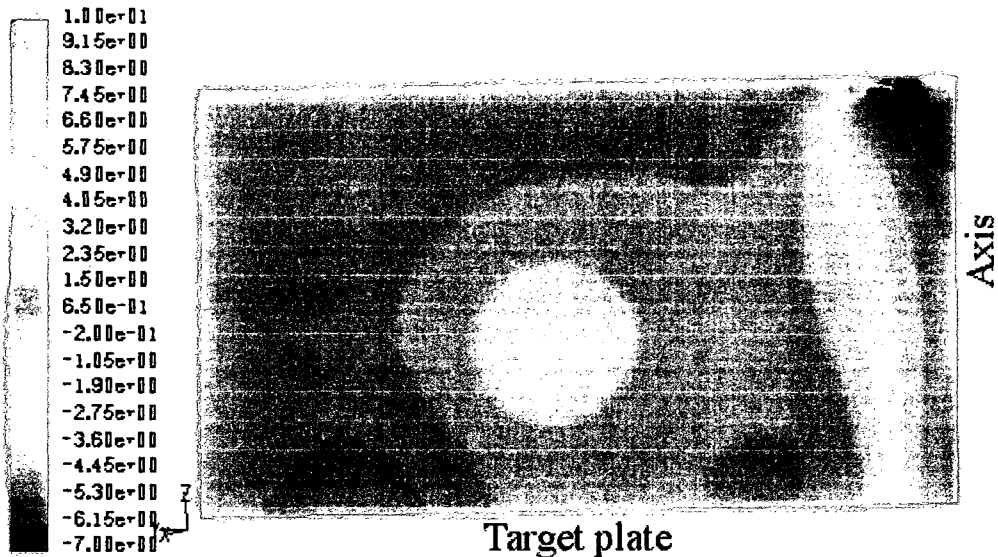


Figure 5.56 Meridian View of Static Pressure Contours (spray angle = 22.5°)

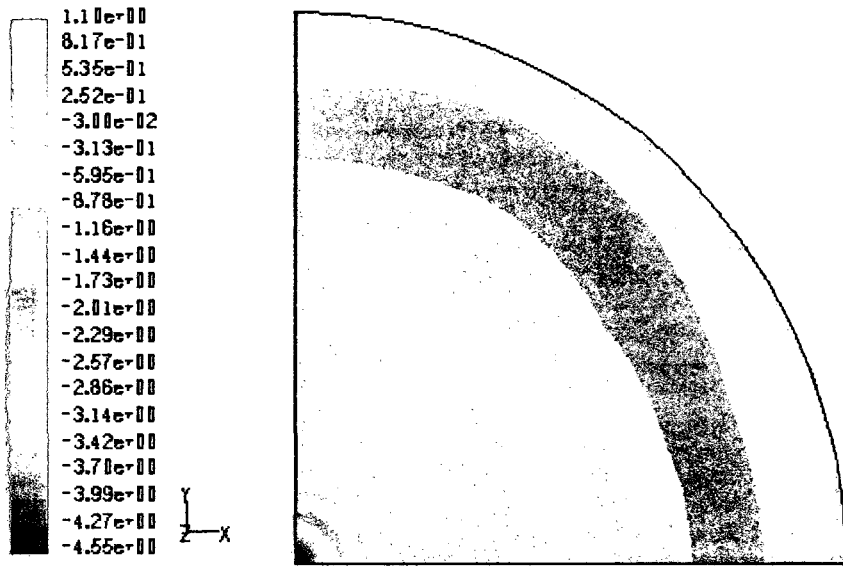


Figure 5.57 Static Pressure Contours on the Target Plate (spray angle = 22.5°)

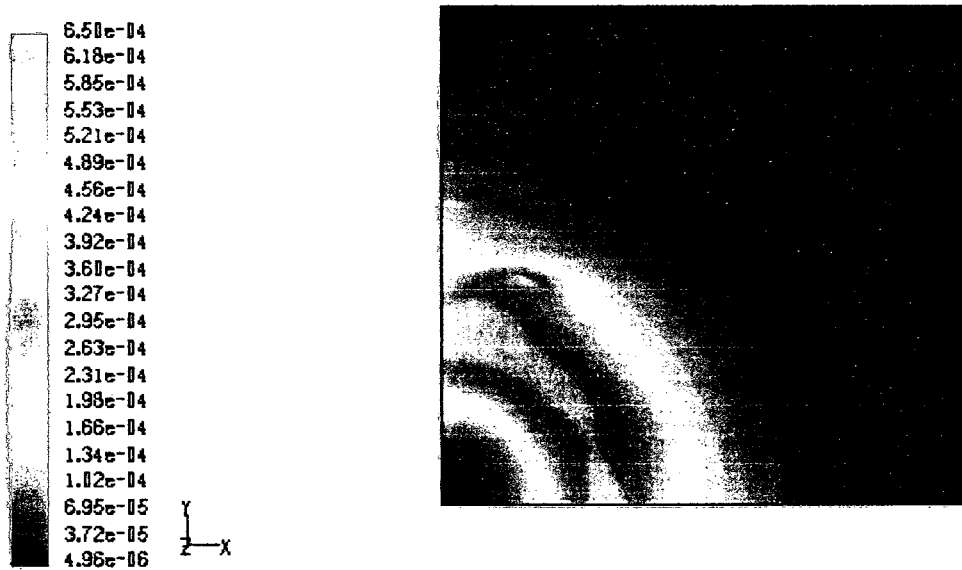


Figure 5.58 Turbulent Kinetic Energy Contours at the Centre of the Target Plate (spray angle = 22.5°)

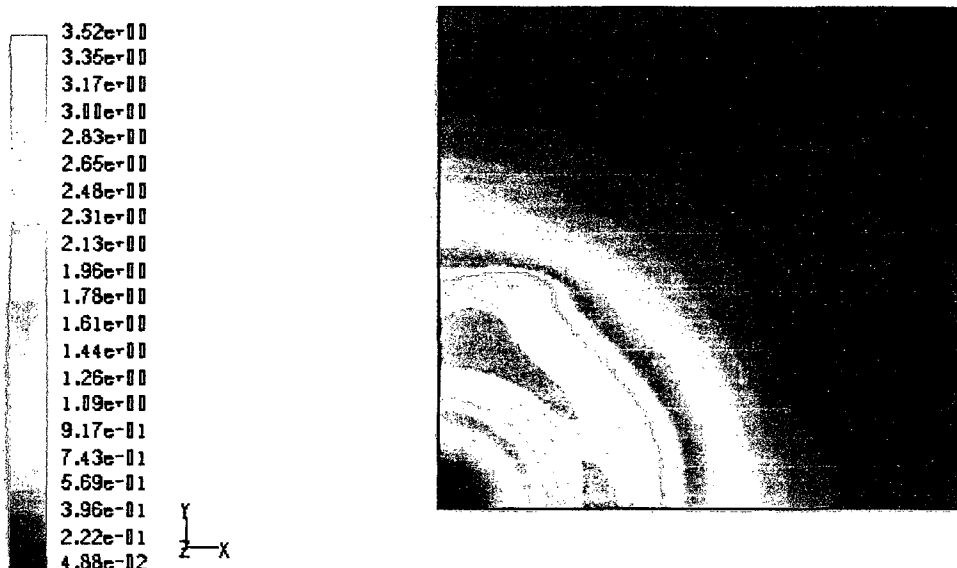


Figure 5.59 Turbulent Dissipation Rate Contours at the Centre of the Target Plate (spray angle = 22.5°)

5.9 Conclusions

Based on the simulations undertaken in this chapter, the following conclusions can be drawn.

It is advantageous to use separate meshes for the electric field calculation and the droplet transfer calculation. The circumferential uniformity of the electric potential (shown in Figure 5.11) confirms the plausibility and feasibility of calculating the electric field in a mesh that is clustered (but not circumferentially uniform) around the electrodes. Then, the results can be imported into a circumferentially uniform mesh, provided the electric field is circumferentially uniform in the region where the second mesh is constructed.

The droplet transfer simulations can be carried out in reasonable time. The predicted electric potential contours, electric field strength and spray pattern are realistic. The predicted air circulation zone was observed by previous researchers. It can be concluded that the mesh structure, spray models and numerical algorithm applied in the present study are appropriate.

CHAPTER 6 PAINT FILM THICKNESS AND TRANSFER EFFICIENCY

When a droplet hits the target plate (wall), it may deposit or rebound, and some of the rebounded droplets may fall to the plate again and deposit onto it. The paint droplets that deposit onto the plate accumulate to form the paint film. Assuming that the fate of all the droplets hitting the plate is to deposit, a method is developed in this chapter to predict the paint film thickness profile on the plate. Information from the film thickness profile can then be used to estimate the spray transfer efficiency.

The Discrete Phase Model in FLUENT is capable of computing the accretion at a cell face j of the wall, defined as:

$$R_j = \frac{1}{A_j} \sum_{i=1}^{N_j} m_i \quad (6.1)$$

where m_i is the mass of a droplet i that hits that cell face on the wall, A_j is the area of that cell face, and N_j is the total number of droplets striking that cell face. By turning on the Erosion/Accretion option of FLUENT, the accretion at the wall boundary faces is calculated when the droplet tracks are updated. Figure 6.1 shows the paint accretion on the target plate after 0.25 s, at the baseline condition.

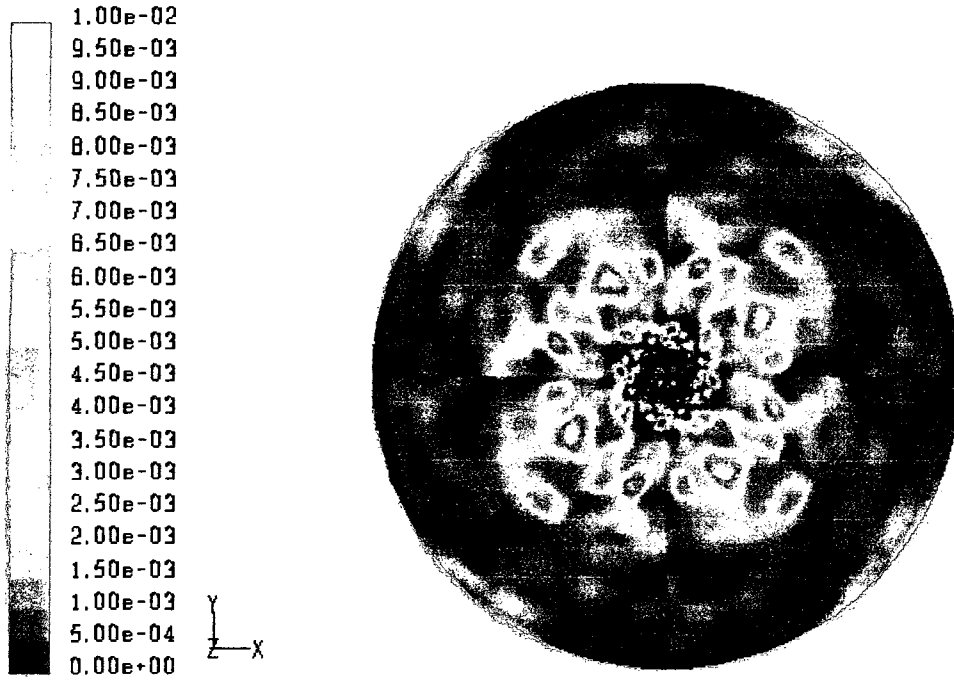


Figure 6.1 Paint Accretion on the Target Plate for 0.25 s at the Baseline Operating Condition (kg/m^2)

6.1 Paint Film Thickness Calculation

Since the measurement data were taken at 36 points with uniform interval along the central line of the target plate, the circular surface of the plate used in the numerical simulations was divided into 36 bands with equal width in the x direction. Figure 6.2 shows the bands created for the paint film thickness calculation. The circular plate represents the target plate boundary in the computational domain. The rectangular plate corresponds to the actual 36 inch x 4 inch workpiece used in the experiment.

The total mass of the paint deposited in a band k can be calculated from the accretion as

$$M_k = \sum_{j=1}^L R_j A_j = \sum_{j=1}^L \sum_{i=1}^{N_j} m_i \quad (6.2)$$

where A_j is now the face area of a cell in the band k of the plate and L is the total number of cells in band k . This calculation can be accomplished by using the UDF

feature of FLUENT. The details associated with this calculation can be obtained by close examination of UDF3 found in the Appendix.

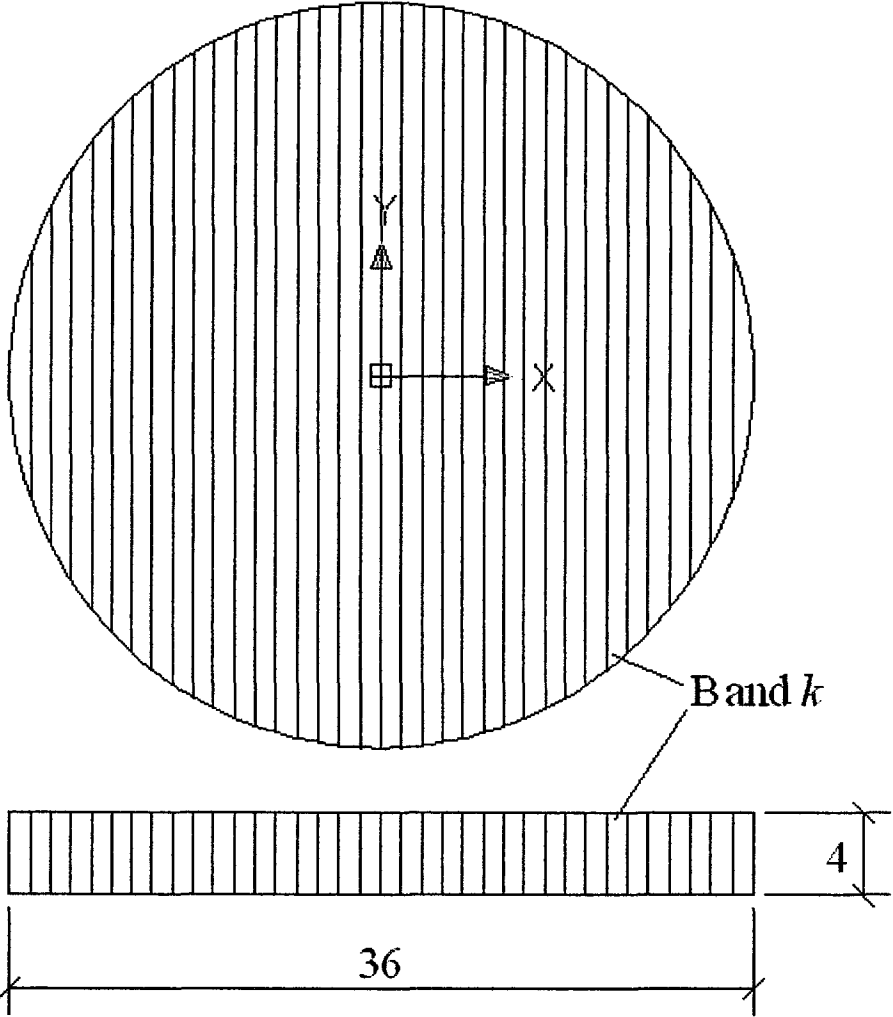


Figure 6.1 Bands Created for Paint Film Thickness Calculation

In the experiments, the workpiece passed below the spray nozzle with a speed of 3.2 inch/s and the width of the workpiece is 4 inch. Therefore, it takes 1.25 seconds for the workpiece to pass through the nozzle. Considering the workpiece to be divided into 36 bands, the width of each band is 1 inch. Thus, the area of a band on the workpiece is four square inches. All the paint deposited on the band k of the circular plate in the 1.25

seconds actually, in the experiments, deposits on the band k of the workpiece. The averaged wet film thickness Δ_k on band k of the workpiece can be calculated using

$$\Delta_k = \frac{M_k}{A_k \rho_p} \quad (6.3)$$

where A_k is the area of band k on the workpiece, i.e. 4 inch², and ρ_p is the paint density.

Once the predicted wet film thickness is calculated, it can be converted into a corresponding dry film thickness by multiplying by the volumetric solid component ratio C_v of the paint. The experimental and CFD paint film thickness profiles will be compared in Section 6.3.

6.2 Transfer Efficiency Calculation

The spray transfer efficiency is defined as the ratio of the mass of droplets deposited on the plate to the mass of paint injected from the nozzle in a specified period of time, i.e.,

$$TE = \frac{\text{Mass of deposition}}{\text{Mass of injection}} \quad (6.4)$$

In the current work, the mass of deposition is the mass of paint accreted on the plate and the mass of injection is the total mass of paint injected from the nozzle.

FLUENT can report the mass of paint accretion on the target plate during a specific period of time, by evaluating a surface integral within the DPM. The mass of paint injection is the product of the paint mass flow rate and the time taken.

6.3 Results and Discussion

The paint film thickness and transfer efficiency have been calculated based on the total accretion in a time interval of 0.25 seconds after the spray region has become fully developed. This length of time corresponds to that in the experiments.

6.3.1 Paint Film Thickness Profile and Spray Transfer Efficiency at Baseline Condition

Figure 6.3 show the paint film thickness profile and transfer efficiency (TE) of the spray at paint flow rate of 150 cc/min and shaping air flow rate of 250 cc/min (baseline conditions). Overall the predicted profile is more flat than the profile measured in the experiment. Of course, since the simulation has been carried out on a quarter cylindrical domain with periodic boundary conditions, the predicted film thickness profile is symmetric about the centre of the plate. On the left part of the target plate, the predicted profile is a little lower than the experimental result. Although a similar feature is observed at the right end of the plate, the predicted profile is higher than the experimental one over most of the plate. The transfer efficiency of 0.69 from the CFD prediction agrees very well with the experimental value of 0.67.

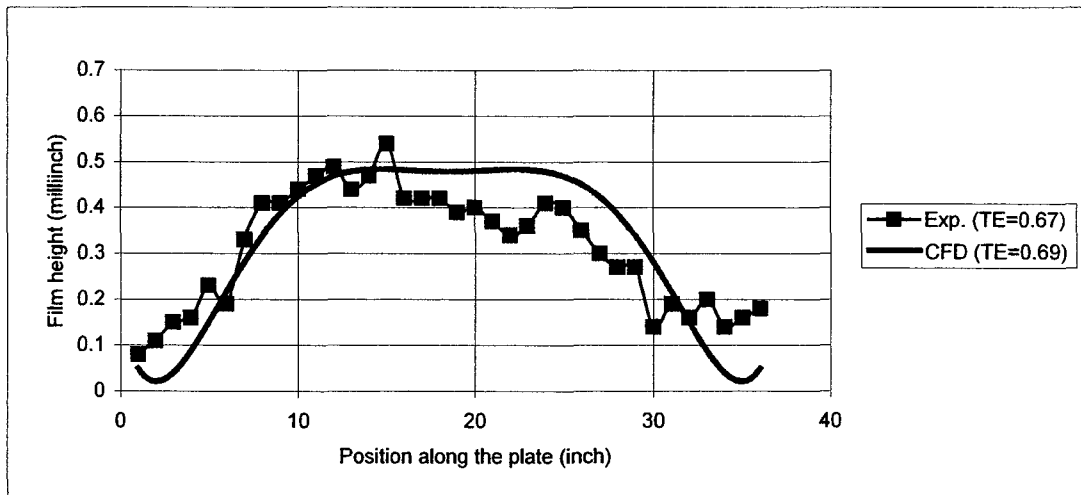


Figure 6.3 Paint Film Thickness Profile and Transfer Efficiency (paint flow rate = 150 cc/min, shaping air flow rate = 250 cc/min)

6.3.2 Effect of Voltage

Figure 6.4 shows the effect of electric potential on the film build profile. It is obvious that the voltage of 50 kV results in a wavy profile shape and very low paint deposition. Although the profile of the 70 kV and 90 kV cases are very close, the 90 kV produces a slightly flatter profile. Figure 6.4 also indicates that the electric charge dramatically improves the TE when electric potential on the electrodes changes from 50 kV to 70 kV. However, applying higher electric potential, e.g., 90 kV, does not seem to improve the efficiency further.

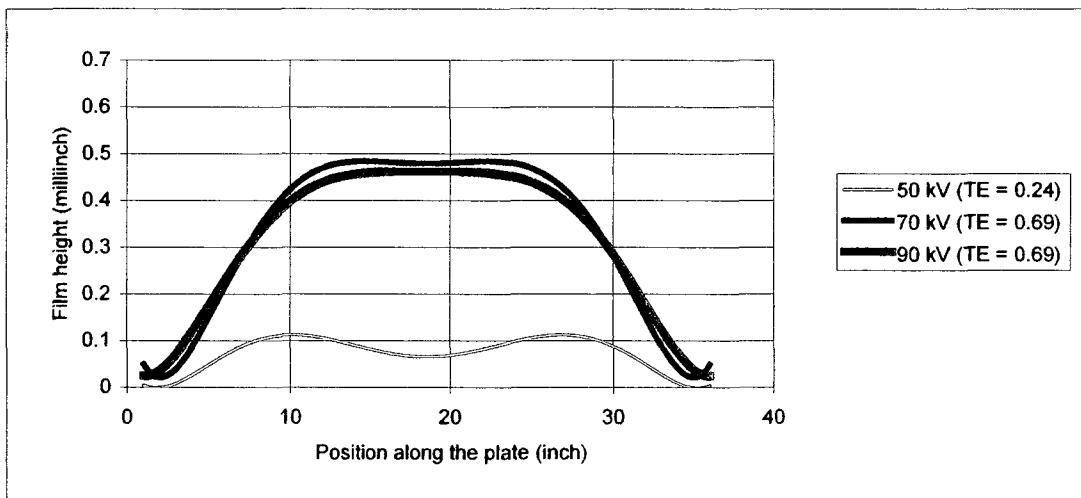


Figure 6.4 Predicted Paint Film Thickness Profiles and Transfer Efficiencies for Varying Electric Charge

6.3.3 Effect of Droplet Diameter

Figure 6.5 shows the effect of initial droplet size on the paint film thickness profile. Compared with the other two cases, the initial droplet size of 1.62 micron results in a globally flatter profile, although the profile at the centre of the plate is worse. Figure 6.5 also indicates that the transfer efficiency decreases slightly with the decrease of droplet size.

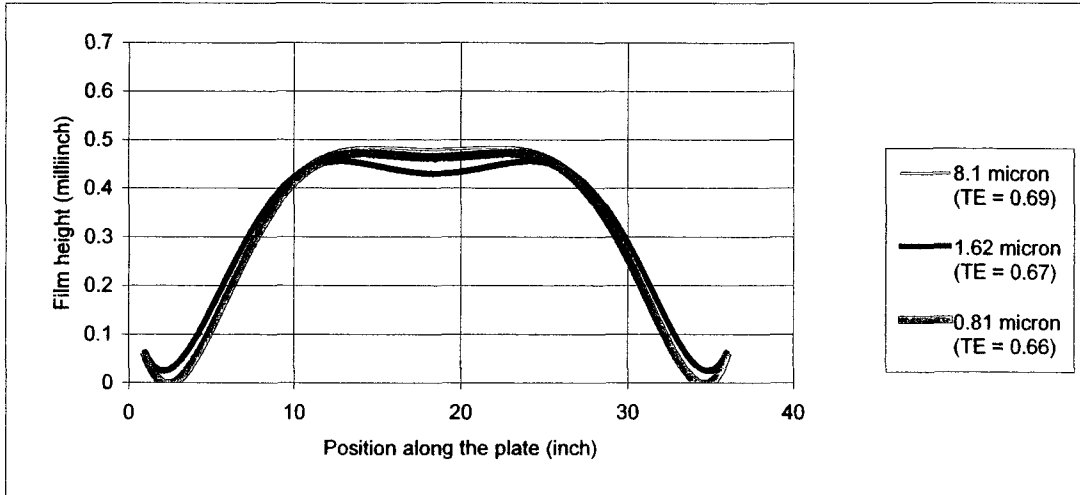


Figure 6.5 Predicted Paint Film Thickness Profiles and Transfer Efficiencies for Varying Initial droplet Diameter

6.3.4 Effect of Bell Rotational Speed

The bell rotational speed effect on the profile is shown in Figure 6.6. The 42000 rpm case demonstrates a globally better profile. Figure 6.6 also shows that, for this range of bell speed, there is no significant effect of bell rotational speed on the TE.

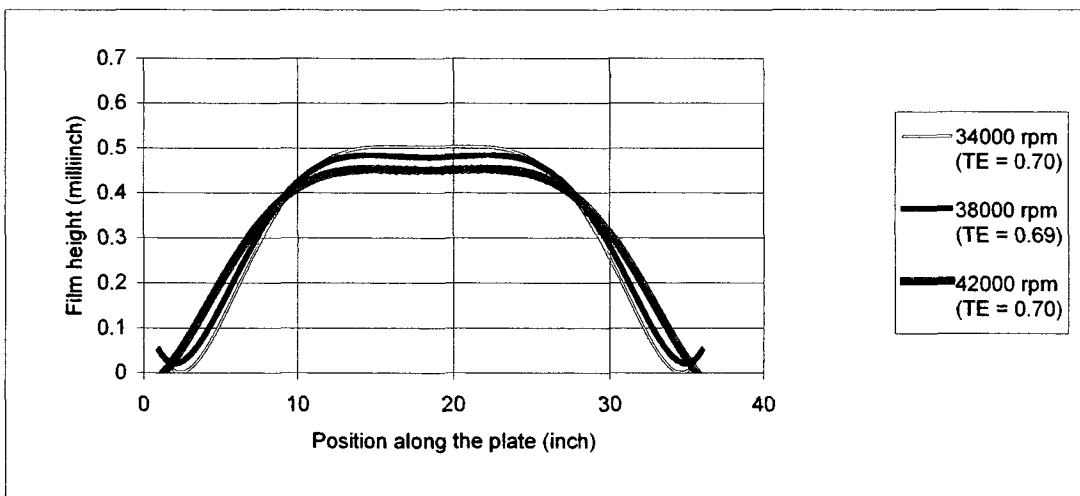


Figure 6.6 Predicted Paint Film Thickness Profiles and Transfer Efficiencies for Varying Rotational Speed

6.3.5 Effect of Paint Flow Rate

Figure 6.3, Figure 6.7 and Figure 6.8 show the effect that varying the paint flow rate has on the paint film thickness and transfer efficiency, at a fixed shaping air flow rate of 250 cc/min. As seen in these figures, the predicted paint film thickness profiles agree well with experimental data. There is no flatness trend of paint film thickness profile with paint flow rate, as seen in Figure 6.9. Although there is no trend of the TE value for the measurement, the CFD results predict that the TE decreasing as the paint flow rate increases.

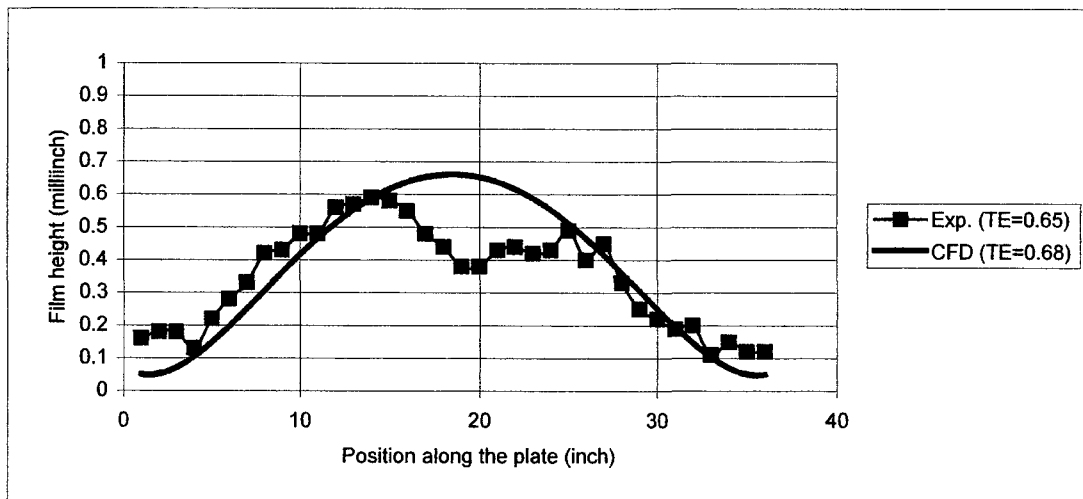


Figure 6.7 Paint Film Thickness Profile and Transfer Efficiency (paint flow rate = 175 cc/min, shaping air flow rate = 250 cc/min)



Figure 6.8 Paint Film Thickness Profile and Transfer Efficiency (paint flow rate = 200 cc/min, shaping air flow rate = 250 cc/min)

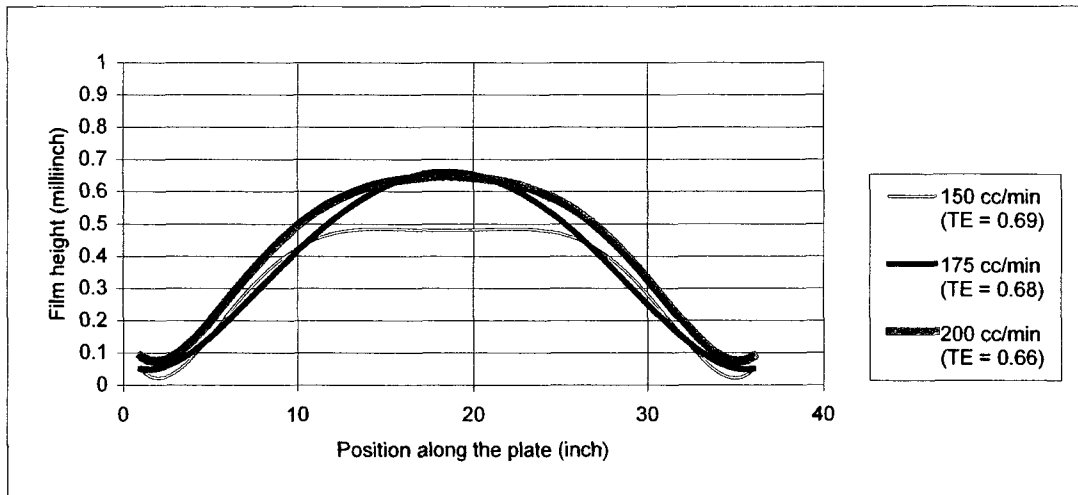


Figure 6.9 Predicted Paint Film Thickness Profiles and Transfer Efficiencies for Varying Paint Flow Rate (shaping air flow rate = 250 cc/min)

6.3.6 Effect of Shaping Air Flow Rate

Figure 6.7, Figure 6.10 and Figure 6.11 show the paint film thickness and transfer efficiency at a fixed paint flow rate of 175 cc/min, with varying shaping air flow rate. These figures further demonstrate that the CFD results agree well with measurements. The simulations indicate that the paint film thickness profile narrows when the shaping

air flow rate becomes large, as seen in Figure 6.12. For shaping air flow rates between 150 cc/min and 200 cc/min, the profiles are fairly flat over the middle half of the plate. Figure 6.12 also indicates that an increase of shaping air flow rate can enhance the spray transfer efficiency (TE) value.

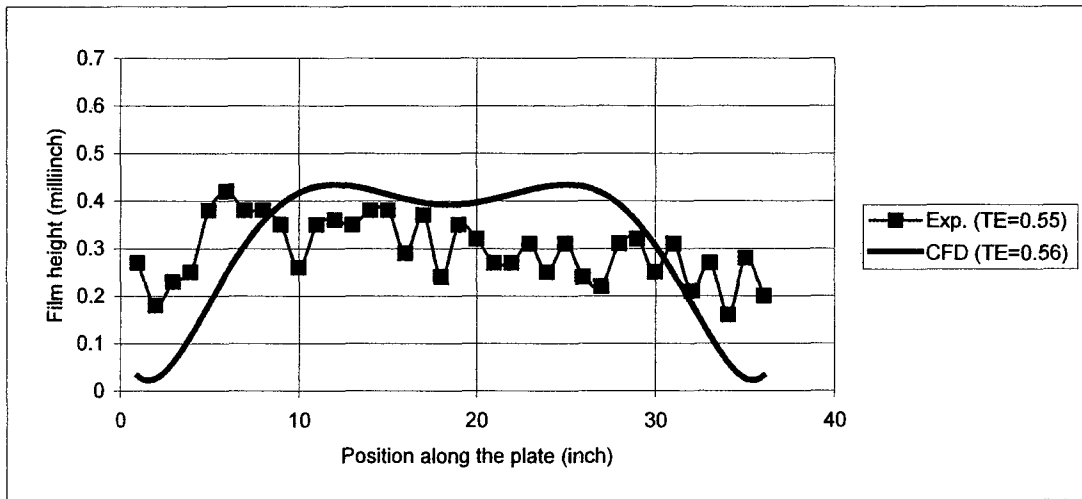


Figure 6.10 Paint Film Thickness Profile and Transfer Efficiency (paint flow rate = 175 cc/min, shaping air flow rate = 150 cc/min)

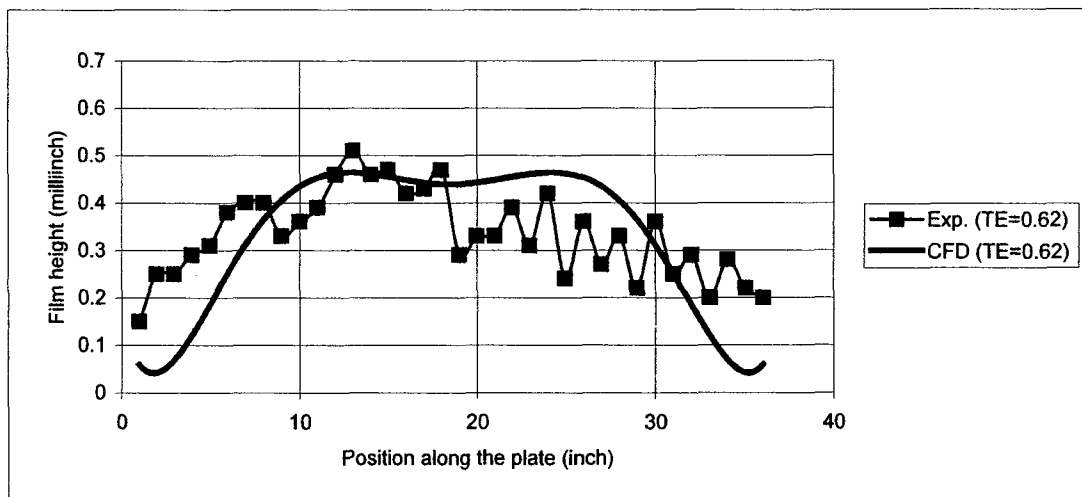


Figure 6.11 Paint Film Thickness Profile and Transfer Efficiency (paint flow rate = 175 cc/min, shaping air flow rate = 200 cc/min)

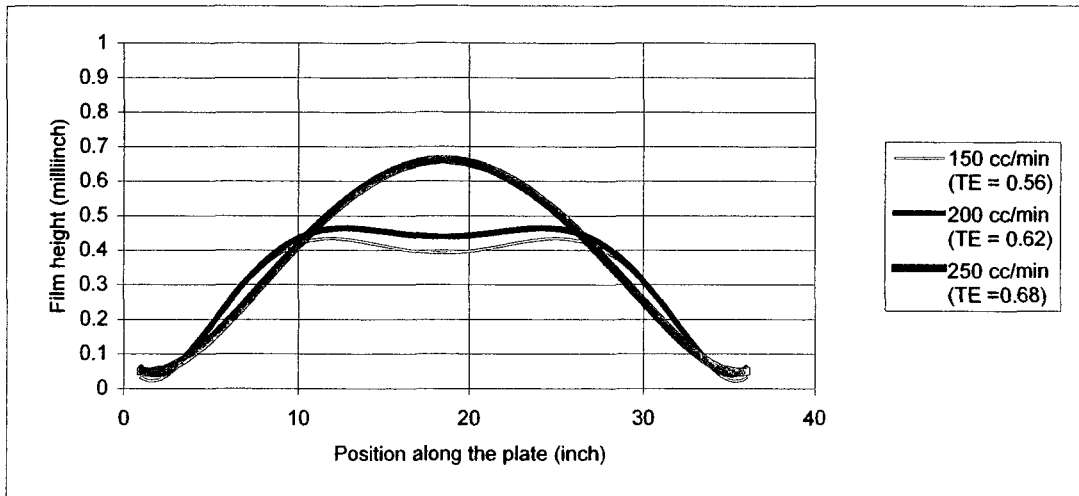


Figure 6.12 Predicted Paint Film Thickness Profiles and Transfer Efficiencies for Varying Shaping Air Flow Rate (paint flow rate = 175 cc/min)

6.3.7 Effect of Spray Angle

Figure 6.13 shows the effect of initial spray angle on the profile. It can be seen that the spray angle at 32.5 degrees results in a flatter profile. Figure 6.13 also shows that there is no significant TE difference with varying spray angle.

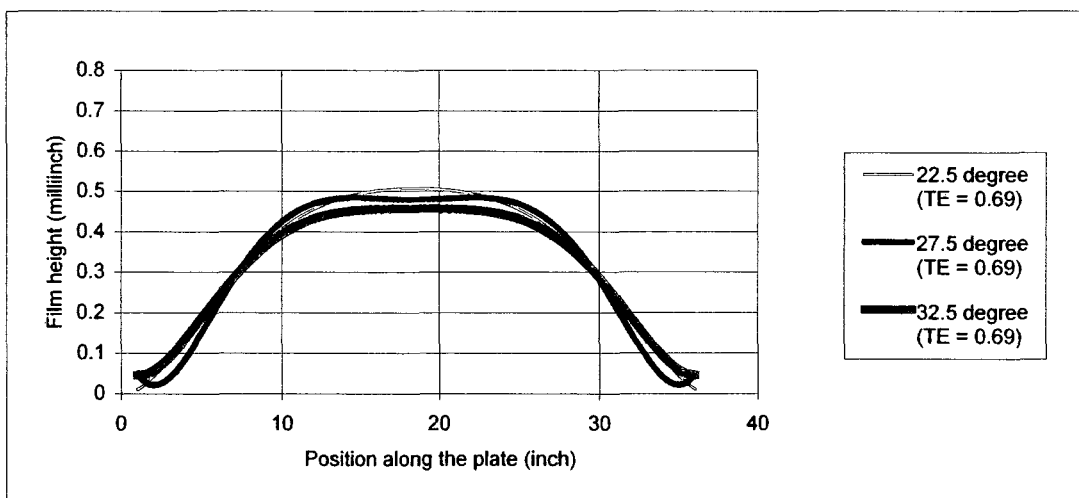


Figure 6.13 Predicted Paint Film Thickness Profiles and Transfer Efficiencies for Varying Spray Angle

6.4 Conclusions

Based on the above results and discussion, the following conclusions can be drawn, for the range of parameters used in this study.

The predicted paint film thickness profiles and transfer efficiency values match the experimental data very well.

The rate at which the paint is pumped into the nozzle affects both the transfer efficiency and the film profile by thickening the film and decreasing the efficiency.

The shaping air noticeably confines the spray. An increase in shaping air flow rate improves the transfer efficiency and narrows the film thickness profile.

An increase in electric charge can improve the transfer efficiency over that attained at low potential.

The transfer of the paint from the bell cup to the target plate is more efficient for larger paint particles. These particles also create a thicker film build on the plate.

The rotational speed of the bell cup has very little effect on the film thickness, and no effect on the transfer efficiency.

An increase in the spray angle causes the film thickness profile to flatten slightly without influencing the transfer efficiency.

These effects have been summarized in Table 6.1.

Parameter increased (↑)		Thickness	TE
Voltage	50 - 70 kV	↑	↑
	70 - 90 kV	↓	↔
Droplet diameter		↔	↑
Rotational speed		↓	↔
Paint flow rate		↑	↓
Shaping air flow rate		↑	↑
Spray angle		↓	↔

Table 6.1 Summary of the Parametric Study on the Paint Film Thickness and Transfer Efficiency

CHAPTER 7 CONCLUSIONS AND RECOMMENDATIONS

7.1 Conclusions

In this study, a three-step numerical simulation procedure has been devised and shown to be a feasible methodology to study the spray process of the electrostatic high-speed rotary bell applicator. These three steps involve separate modeling for the disintegration, fully developed spray and droplet/wall interaction regions. This procedure is general enough that it could be applied to other atomizers operating under similar conditions. Conclusions can be drawn on (i) simulation of the flow in the atomizer, (ii) the droplet transfer simulation and (iii) the film thickness and transfer efficiency calculation.

7.1.1 Simulation of the Flow in the Atomizer

A numerical procedure to calculate the paint droplet sizes and velocities at the edge of the high-speed rotary atomizer has been successfully developed. Most significantly, it has been demonstrated that this information can be obtained by performing a single-phase paint flow simulation inside the bell cup, rather than a more complicated and computationally expensive two-phase simulation.

The simulations predict that the droplet size and velocities vary linearly with rotational speed of the bell and flow rate of the paint, in agreement with previously published data. The spray angle varies slightly with bell speed and flow rate.

The droplet properties obtained through this procedure can be used as inputs for the droplet transfer simulation. This method is a good alternative to using data from more expensive droplet measurement experiments, as done by previous researchers.

7.1.2 Droplet Transfer Simulation

Separate meshes are created for the electric field calculation and the droplet transfer calculation. This is shown to be advantageous because of the flow and corresponding mesh complexities associated with each of these calculations. The circumferential uniformity of the electric potential in the droplet transfer region supports

the plausibility and feasibility of calculating the electric field in a mesh that is clustered (but not circumferentially uniform) around the electrodes. Then, the results can be imported into a circumferentially uniform mesh, provided the electric field is circumferentially uniform in the region where the second mesh is constructed. This approach significantly reduces the size of the computational mesh, and consequently the run times.

The droplet transfer simulations can be carried out in reasonable computational time. The predicted electric potential contours, electric field strength and spray pattern are realistic. The predicted air circulation zone is similar to that observed by previous researchers. It can be concluded that the mesh structure, spray models and numerical algorithm applied in the present study are appropriate.

7.1.3 Film Thickness and Transfer Efficiency Calculation

A simple procedure has been developed to compute the paint film thickness on the target plate and the transfer efficiency of the spray, using the data from the CFD simulation of the fully developed spray. Over the range of parameters used in this study, the predicted paint film thickness profiles and transfer efficiency values match the experimental data very well. No procedure of this type, and no paint film thickness profiles have been previously reported in the literature.

The rate at which the paint is pumped into the nozzle affects both the transfer efficiency and the film profile by thickening the film and decreasing the efficiency. The shaping air noticeably confines the spray. An increase in shaping air flow rate improves the transfer efficiency and narrows the film thickness profile. An increase in electric charge can improve the transfer efficiency over that attained at low potential. The transfer of the paint from the bell cup to the target plate is more efficient for larger paint particles. These particles also create a thicker film build on the plate. The rotational speed of the bell cup has very little effect on the film thickness, and no effect on the transfer efficiency. An increase in the spray angle causes the film thickness profile to flatten slightly without influencing the transfer efficiency.

7.2 Recommendations for Future Work

There are several possible reasons for any discrepancies between the experimental film profile and the predicted film profile. Some of the following factors should be considered:

- The experimental film build profile data are not based on duplicated experiments. The data would be more reliable if the experiments had been repeated at any single condition, and any errors in instrument setting and measurement were further removed.
- The experimental film build profile data were measured from the dry paint film. The numerical film thickness data are derived from the wet film thickness multiplied by the ratio of dry component.
- Droplet evaporation and paint film deformation and evaporation have been neglected in the simulation.
- Surface tension value of water was assumed for the surface tension value of the paint.
- Single-phase instead of two-phase simulations were conducted in the bell atomizer.
- The film thickness at the edge of the bell was taken as the initial droplet diameter. Film thickness has a very close relation with droplet size, but they may not be exactly equal to each other.
- The force exerted on the electrostatic field by the moving charged droplets has been neglected. Only the electrostatic force on the droplets exerted by the electrostatic field was considered.
- The electrostatic interaction between droplets has been neglected.
- The polynomial for charge-to-mass ratio vs. droplet diameter was derived from a published figure of experimental data, which was very rough. Since this is an important parameter affecting the droplet transfer, a better representation of this relationship may lead to more accurate predictions.

As an extension of the work reported in this dissertation, further improvements on this study could be accomplished through the following efforts:

- Scrutinize the setting of the experiments and repeat the experiments several times for a single condition so as to minimize the experimental errors.
- Develop a method to measure the wet film profile on the target plate.
- Run the two-phase simulation within the atomizer.
- Determine the correlation of film thickness at the bell edge and initial droplet diameter.
- Incorporate evaporation modeling into the numerical simulations.
- Incorporate the electrostatic interaction between charged droplets, and the effect that the moving charged droplets have on the electrostatic field.
- Incorporate more precise paint property values.
- Determine and incorporate more accurate charge-to-mass ratio vs. droplet size functions.

REFERENCES

Alajbegovic, A. and Meister, G., Simulation of Multiphase Flow with Vaporization in DGI Engine Injector, ASME 2001-ICE-393, Argonne, USA, 2001.

ANSYS ICEM CFD 4.3, Berkeley, CA, USA.

Arcoumanis, C. and Gavaises, M., Pressure-Swirl Atomizers for DISI Engines: Further Modeling and Experiments, SAE 2000-01-1044, Detroit, USA, 2000.

Bai, C. and Gosman, A.D., Development of Methodology for Spray Impingement Simulation, SAE 950283, 1995.

Bailey, A.G., *Electrostatic Spraying of Liquids*, Wiley, New York, USA, 1988.

Bauckage, K., Scholz, T. and Schulte, G., Atomization of Water-Based Metallic Paints by Means of Electrostatic Rotary Atomizers, Proceedings of ICLASS-94, pp. 1010-1019, Rouen, France, 1994.

Bauckage, K., Scholz, T. and Schulte, G., The Influence of Applied High-Voltage on the Atomization Characteristic of a Commercial High-Speed Rotary Atomizer, Proceedings of the 4th International Congress on Optical Particle Sizing, pp. 337-346, Nurnberg, Germany, 1995.

Bell, G.C. and Hochberg, J., Mechanics of Electrostatic Atomization, Transport, and Deposition of Coatings, Organic Coatings Science and Technology, Vol. 5, pp. 325-357, 1981.

Bhatia, J.C. and Durst, P., A Comparative Study of Some Probability Distributions Applied to Liquid Sprays, Proceedings of International Conference On Mechanics of Two-phase Flows, pp. 279-284, Taipei, Taiwan, 1989.

Bussmann, M., Mostaghimi, J. and Chandra, S., Modeling the Splash of a Droplet Impacting a Solid Surface, Physics of Fluids, Vol. 12, pp. 3121-3132, 2000.

Chandra, S. and Avedisian, C.T., On the Collision of a Droplet With a Solid Surface, Proceedings of the Royal Society of London, Vol. 432, pp. 13-41, 1991.

Chryssakis, C.A., Assanis, D.N., Lee, J. and Nishida, K., Fuel Spray Simulation of High-Pressure Swirl-Injector for DISI Engines and Comparison with Laser Diagnostic Measurements, SAE 2003-01-0007, 2003.

Corbeels, P.L., Senser, D.W. and Lefebvre, A.H., Atomization Characteristics of a High-Speed Rotary Bell Paint Applicator, Atomization Sprays, Vol. 2, pp. 87-99, 1992.

Cossali, G.E., Coghe, A. and Marengo, M., The Impact of a Single Drop on a Wetted Solid Surface, Experiments in Fluids, Vol. 22, pp. 463-472, 1997.

Cousin, J. and Nuglisch, H.J., Modeling of Internal Flow in High Pressure Swirl Injectors, SAE 2001-01-0963, 2001.

Domnick, J. and Thieme, M., Atomization Characteristics of High-Speed Rotary Bell Atomizers, Proceedings of ILASS-Europe-2004, pp. 527-534, Nottingham, UK, 2004.

Dooley, B.S., Warncke, A.E., Gharib, M. and Tryggvason, G., Vortex Ring Generation Due to the Coalescence of a Water Drop at a Free Surface, Experiments in Fluids, Vol. 22, pp. 369-374, 1997.

Ellwood, K.R.J. and Braslaw, J., A Finite-Element Model for an Electrostatic Bell Sprayer, *Journal of Electrostatics*, Vol. 45, pp. 1-23, 1998.

FLUENT 6.1, *User's Guide*, FLUENT Inc, Lebanon, NH, USA.

FLUENT 6.1, *UDF Manual*, FLUENT Inc, Lebanon, NH, USA.

Fogliati, M., Fontana, D., Garbero, M., Vanni, M. and Baldi, G., CFD Simulation of Paint Deposition in an Air Spray Process, *JCT Research*, Vol. 3, pp. 117-125, 2006.

Fukai, J., Zhao, Z., Poulikakos, D., Megaridis, C.M. and Miyatake, O., Modeling of the Deformation of a Liquid Droplet Impinging upon a Flat Surface, *Physics of Fluids*, Vol. 5, pp. 2588-2599. 1993.

Fukai, J., Shiiba, Y., Yamamoto, T., Miyatake, O., Poulikakos, D., Megaridis, C.M. and Zhao, Z., Wetting Effects on the Spreading of a Liquid Droplet Colliding with a Flat Surface, *Physics of Fluids*, Vol. 7, pp. 236-246, 1995.

Garbero, M., Vanni, M. and Baldi, G., CFD Modeling of a Spray Deposition Process of Paint, *Macromolecular Symposia*, Vol. 187, pp. 719-729, 2002.

Gemci, T., Hitron, R. and Chigier, N., Measuring Charge-to-Mass Ratio of Individual Droplets Using Phase Doppler Interferometry, *Proceedings of the 15th Annual Conference of ILASS-Americas*, pp. 241-245, Madison, WI, USA, 2002.

Ghafouri-Azar, R., Mostaghimi, J. and Chandra, S., Numerical Study of Impact and Solidification of a Droplet Over a Deposited Frozen Splat, *Proceedings of the 10th Annual Conference of CFD Society of Canada, CFD02*, pp. 61-65, Windsor, Canada, 2002.

Han, Z., Parrish, S., Farrell, P.V. and Reitz, R.D., Modeling Atomization Processes of Pressure-Swirl Hollow-Cone Sprays, *Atomization and Sprays*, Vol. 7, pp. 663-684, 1997.

Hicks, P.G., Drop Transport in Air Sprays, Ph.D. Dissertation, School of Mechanical Engineering, Purdue University, USA, 1995.

Hicks, P.G. and Senser, D.W., Simulation of Paint Transfer in an Air Spray Process, *Journal of Fluids Engineering*, Vol. 117, pp. 713-719, 1995.

Hinze, J.O. and Milborn, H., Atomization of Liquids by Means of a Rotating Cup, *Journal of Applied Mechanics*, Vol. 17, pp. 145-153, 1950.

Huang, H., Lai, M. and Meredith, W., Simulation of Spray Transport from Rotary Cup Atomizer using KIVA-3V, The 10th International KIVA User's Group Meeting, Detroit, USA, 2000.

Im, K., An Experimental and Numerical Study of the Spray Transfer Processes in An Electrostatic Rotating Bell Sprayer. Ph.D. Dissertation, Department of Mechanical Engineering, Wayne State University, USA, 1999.

Im, K., Lai, M., Liu, Y., Sankagiri, N., Loch, T. and Nivi, H., Visualization and Measurement of Automotive Electrostatic Rotary-Bell Paint Spray Transfer Processes, *Journal of Fluids Engineering*, Vol. 123, pp. 237-245, 2001.

Im, K., Lai, M., Yu, S. and Matheson, R.R., Simulation of Spray Transfer Processes in Electrostatic Rotary Bell Sprayer, *Journal of Fluids Engineering*, Vol. 126, pp. 449-456, 2004.

Lefebvre, A.H., *Atomization and Sprays*, Hemisphere Publishing Corporation, New York, USA, 1989.

Lefebvre, A.H., The Prediction of Sauter Mean Diameter for Simplex Pressure-Swirl Atomizers, *International Journal of Atomization and Spray Technology*, Vol. 3, pp. 37-51, 1987.

Li, X. and Tankin, R.S., Derivation of Droplet Size Distribution in Sprays by Using Information Theory, *Combustion Science and Technology*, Vol. 60, pp. 345-357, 1988.

Mao, T., Kuhn, D.C. and Tran, H., Spread and Rebound of Liquid Droplets upon Impact on Flat Surfaces, *AIChE Journal*, Vol. 43, pp. 2169-2179, 1997.

McCarthy, J.E. Jr., Basic Studies on Spray Coating: Drop Rebound From a Small Workpiece with a Conventional Air Applicator, M.S.M.E. Thesis, School of Mechanical Engineering, Purdue University, 1991.

McCarthy, J.E. Jr., Paint Transfer in Electrostatic Air Sprays, Ph.D. Dissertation, School of Mechanical Engineering, Purdue University, 1995.

Moriyoshi, Y., Hu, X. and Takagi, M., Experimentally Evaluated Spray Model for a Swirl-Type Injector, SAE 2002-01-2696, 2002.

Morsi, S.A. and Alexander, A.J., An Investigation of Particle Trajectories in Two-Phase Flow Systems, *Journal of Fluid Mechanics*, Vol. 55, pp. 193-208, 1972.

Mundo, C., Sommerfeld, M. and Tropea, C., Experimental Studies of the Deposition and Splashing of Small Liquid Droplets Impinging on a Flat Surface, *Proceedings of ICLASS-94*, pp. 134-141, Rouen, France, 1994.

Mundo, C., Sommerfeld, M. and Tropea, C., Droplet-Wall Collisions: Experimental Studies of the Deformation and Breakup Process, *International Journal of Multiphase Flow*, Vol. 21, pp. 151-173, 1995a.

Mundo, C., Lacknermeier, U., Sommerfeld, M. and Tropea, C., Numerical and Experimental Studies of the Splashing and Deposition of Spray Droplets on Surfaces, Proceedings of ICLASS-95, Nurnberg, Germany, 1995b.

Mundo, C., Sommerfeld, M. and Tropea, C., Numerical and Experimental Investigation of Spray Characteristics in the Vicinity of a Rigid Wall, Proceedings of the 1st International Symposium on Two-Phase Flow Modelling and Experimentation, pp. 831-839, Rome, Italy, 1995c.

Mundo, C., Sommerfeld, M. and Tropea C., On the Modeling of Liquid Sprays Impinging on Surfaces, Atomization and Sprays, Vol. 8, pp. 625-652,1998.

Oguz, H.N. and Prosperetti, A., Bubble Entrainment by the Impact of Drops on Liquid Surfaces, Journal of Fluid Mechanics, Vol. 219, pp.143-166, 1990.

O'Rourke, P.J., Collective Drop Effects on Vaporizing Liquid Sprays, Ph.D. Dissertation, Department of Mechanical and Aerospace Engineering, Princeton University, USA, 1981.

Pumphrey, H.C. and Elmore, P.A., The Entrainment of Bubbles by Drop Impacts, Journal of Fluid Mechanics, Vol. 220, pp. 539-557. 1990.

Rein, M., Phenomena of Liquid Drop Impact on Solid and Liquid Surfaces, Fluid Dynamics Research, Vol. 12, pp. 61-93, 1993.

Ruger, M., Hohmann, S., Sommerfeld, M. and Kohnen, G., Euler/Lagrange Calculations of Turbulent Sprays: the Effect of Droplet Collisions and Coalescence, Atomization and Sprays, Vol. 10, pp. 47-81, 2000.

Snyder, H.E., Senser, D.W. and Lefebvre, A.H., Drop Size Measurements in Electrostatic Paint Sprays, IEEE Transactions: Industrial Applications, Vol. 25, No. 4, pp. 720-727, 1989a.

Snyder, H.E., Senser, D.W. and Lefebvre, A.H., Mean Drop Sizes from Fan Spray Atomizers, Transactions of the ASME, Vol. 111, pp. 342-347, 1989b.

Sommerfeld, M., Kohnen, G. and Ruger, M., Some Open Questions and Inconsistencies of Lagrangian Particle Dispersion Models, Proceedings of 9th Symposium on Turbulent Shear Flows, Paper No. 15-1, Kyoto, Japan, 1993.

St-Georges, M. and Buchlin, J.M., Detailed Single Spray Experimental Measurements and One-Dimensional Modeling, International Journal of Multiphase Flow, Vol. 20, No. 6, pp. 979-992, 1994.

Taylor, G.I., The Shape and Acceleration of a Drop in a High Speed Air Stream. Technical Report, In the Scientific Papers of G. I. Taylor, ed., G. K. Batchelor, Cambridge University Press, London, UK, 1963.

Trapaga, G. and Szekely, J., Mathematical Modeling of the Isothermal Impingement of Liquid Droplets in Spraying Processes, Metallurgical Transactions, Vol. 22B, pp. 901-914, 1991.

Tropea, C. and Marengo, M., The Impact of Drops on Walls and Films, Multiphase Science and Technology, Issue 1, pp. 19-36, 1999.

Wang, X.F. and Lefebvre, A.H., Mean Drop Sizes from Pressure Swirl Nozzles, AIAA Journal of Propulsion and Power, Vol. 3, No. 1, pp. 11-18, 1987.

Xing, L., Glass, J.E. and Fernando, R.H., Parameters Influencing the Spray Behaviour of Waterborne Coatings, Journal of Coatings Technology, Vol. 71, pp. 37-50, 1999.

Van Der Geld, C.W.M. and Vermeer, H., Prediction of Drop Size Distributions in Sprays Using the Maximum Entropy Formalism: The Effect of Satellite Formation, International Journal of Multiphase Flow, Vol. 20, pp. 363-381, 1994.

Weiss, D.A. and Yarin, A.L., Single Drop Impact onto Liquid Films: Neck Distortion, Jetting, Tiny Bubbles Entrainment, and Crown Formation, *Journal of Fluid Mechanics*, Vol. 385, pp. 229-254, 1999.

Yarin, A.L. and Weiss, D.A., Impact of Drops on Solid Surfaces: Self-Similar Capillary Waves, and Splashing as a New Type of Kinematic Discontinuity, *Journal of Fluid Mechanics*, Vol. 283, 141-173, 1995.

Yule, A.J. and Chinn, J.J., Swirl Atomizer Flow: Classical Inviscid Theory Revised, *Proceedings of ICLASS-94*, pp. 334-341, Rouen, France, 1994.

APPENDIX USER DEFINED FUNCTIONS

UDF1 - Electrostatic Field Strength Calculation

```
/* UDF for calculating the electrostatic field strength*/

#include "udf.h"

DEFINE_ON_DEMAND(store_gradient)
{
    Domain *domain;
    cell_t c;
    Thread *t;

    domain=Get_Domain(1);

    /* Fill the UDM with the three dimensional electrostatic field strength */
    thread_loop_c (t,domain)
    {
        begin_c_loop (c,t)
        {
            C_UDMI(c,t,0) = 0-C_UDSI_G(c,t,0)(0);
            C_UDMI(c,t,1) = 0-C_UDSI_G(c,t,0)(1);
            C_UDMI(c,t,2) = 0-C_UDSI_G(c,t,0)(2);
            C_UDMI(c,t,3) = NV_MAG(C_UDSI_G(c,t,0));
        }
        end_c_loop (c,t)
    }
}
```

UDF2 - Electrostatic Force Incorporation

```
/* UDF for incorporating the electrostatic force on a charged droplet */
/* C_UDMI(c,t,0) is x component of electrostatic field strength in the cell.
   C_UDMI(c,t,1) is y component of electrostatic field strength in the cell.
   C_UDMI(c,t,2) is z component of electrostatic field strength in the cell.
*/
/* Define bforce_acceleration as the electrostatic acceleration */

#include "udf.h"
#include "dpm.h"
#include "surf.h"

#define TSTART 0 /* electric field applied at t = 0 */

/* Calculate electrostatic acceleration on charged droplet*/
/* The force = droplet mass * charge-to-mass ratio * electric field strength*/
/* The acceleration = charge-to-mass ratio * electrostatic field strength*/

DEFINE_DPM_BODY_FORCE(electrostatic_body_force, p, i)
{
    float dia,Q_TO_MASS_RATIO; /* Droplet diameter (micron) and charge-to-
mass ratio */

    cell_t c;
    Thread *t;
    real bforce_acceleration;
    c=P_CELL(p);
    t=P_CELL_THREAD(p);
    dia=1000000*P_DIAM(p);
```

```
Q_TO_MASS_RATIO=pow(10,3.3829-0.1837*dia+0.0052*dia*dia-  
0.00005*dia*dia*dia)/1000;
```

```
if(P_TIME(p)>=TSTART)  
{  
  if(i==0) bforce_acceleration=Q_TO_MASS_RATIO*C_UDMI(c,t,0);  
  
  else if(i==1) bforce_acceleration=Q_TO_MASS_RATIO*C_UDMI(c,t,1);  
  
    else if(i==2)  
  
bforce_acceleration=Q_TO_MASS_RATIO*C_UDMI(c,t,2);  
  }  
  else  
    bforce_acceleration=0.0;  
  
  return (bforce_acceleration);  
}
```

UDF3 - Calculation of Mass Accumulation on the Target Plate

```
/* UDF for calculating the paint mass accumulation on the target plate
*/
#include"udf.h"
#include"dpm.h"
#define f_id 4
DEFINE_ON_DEMAND(film_thickness)
{
    FILE *fpr,*fpw1,*fpw2; /* declare file pointer */
    real x(ND_ND);
    real area(ND_ND);
    char string(50);
    int No_cells=0, i=0, j=0, No_bands=18,id;
    float location_f=0, location_b=0, coordinate=0;
    float mass_of_cell=0, radius=0.4572, interval,mass=0;

    Domain *d=Get_Domain(1);
        face_t f;
        Thread *t;

        fpw1=fopen("plate.xy", "w");

        t=Lookup_Thread(d,f_id);

        begin_f_loop(f,t)
        {
            F_CENTROID(x,f,t);
            coordinate=x(0);
```

```

        F_AREA(area,f,t);

mass_of_cell=NV_MAG(area)*F_STORAGE_R(f,t,SV_DPMS_ACCRETION);
        No_cells++;
        fprintf(fpw1, "%d %e %e\n",No_cells,coordinate,mass_of_cell);
        /*print number of cells on the target plate, the x coordinate of
        each cell and the mass accretion in that cell*/
    }
    end_f_loop(f,t)
    fclose(fpw1);

    interval=radius/No_bands;
    location_b=location_b+interval;

    fpw1=fopen("film_thickness.xy", "w");
    fprintf(fpw1, "(title %cDPM Accretion%c)\n", 34,34);
    fprintf(fpw1, "(labels %cPosition%c %cDPM Accretion%c)\n\n", 34,34,34,34);
    fprintf(fpw1, "((xy/key/label %cplate%c)\n", 34,34);

    fpw2=fopen("film_thickness_br.xy", "w");
    fprintf(fpw2, "(title %cDPM Accretion%c)\n", 34,34);
    fprintf(fpw2, "(labels %cPosition%c %cDPM Accretion%c)\n\n", 34,34,34,34);
    fprintf(fpw2, "((xy/key/label %cplate%c)\n", 34,34);

    for(j=0; j<=No_bands; j++)
    {
        fpr=fopen("plate.xy", "r");
        for(i=0; i<No_cells; i++)
        {

```



```

        fscanf(fpr, "%d", &id);/*just move the file pointer to the
        next datum*/
        fscanf(fpr, "%e", &coordinate);
        fscanf(fpr, "%e", &mass_of_cell);
        if((coordinate>location_f)&&(coordinate<=location_b))
        {
            mass=mass+mass_of_cell;
        }

    }
    printf("%e %e\n", location_f,location_b);
    fprintf(fpw1, "%f %e\n", location_f,mass);
    fprintf(fpw2, "%f %e\n", ((location_f)/0.0254+18),mass);
    mass=0;
    location_f=location_b;
    location_b=location_b+interval;
    fclose(fpr);
}

fprintf(fpw1, "");
fprintf(fpw2, "");

fclose(fpw1);
fclose(fpw2);
}

```

VITA AUCTORIS

Name: Ligong Yang
Place of Birth: Mianchi, Henan, China
Year of Birth: 1972
Education: University of Windsor, Windsor, Ontario
2002 – 2006, Ph.D.
University of Windsor, Windsor, Ontario
2000 – 2002, M.A.Sc.
Nanjing University of Science and Technology, Nanjing, China
1989 – 1993, B.A.Sc.